Title

Materials design of flexible bioelectronics for reliable electrochemical signal transduction and electrical signal transmission

Permalink

https://escholarship.org/uc/item/88c3w4bv

Author

Zhao, Yichao

Publication Date

2021

Peer reviewed|Thesis/dissertation

UNIVERSITY OF CALIFORNIA

Los Angeles

Materials design of flexible bioelectronics for reliable electrochemical signal transduction and

electrical signal transmission

A thesis submitted in partial satisfaction

of the requirements for the degree Doctor of Philosophy

in Materials Science and Engineering

by

Yichao Zhao

2021

ABSTRACT OF THE DISSERTATION

Materials design of flexible bioelectronics for reliable electrochemical signal transduction and

electrical signal transmission

by

Yichao Zhao

Doctor of Philosophy in Materials Science and Engineering

University of California, Los Angeles, 2021

Professor Sam Emaminejad, Co-Chair

Professor Qibing Pei, Co-Chair

Both sophisticated electronic systems and human biological systems rely on signal transduction and transmission to achieve all operations and complex tasks. However, there are many fundamental differences between these two systems. For example, the human biological system contains deformable and soft organs/tissues under solution environments, mainly based on chemical reactions to transduce/transmit bio-signals. In comparison, electronics contain non-deformable rigid components under ambient environment mainly, based on electrons to transduce/transmit electrical signals. Even though it is difficult to merge gaps between these two

systems, translation of existing electronics to be compliant with our biological tissues will render a wide panel of applications such as wearable health and wellness monitoring platforms, implantable/ingestible devices, artificial prosthesis, surgery robots, *etc*. As a researcher in materials science and engineering, I am applying reductionism to approach this complicated question by firstly decomposing electronic materials' properties into chemical, electrical, and mechanical domains, then engineering material properties in each domain to be compatible with biological systems as needed. However, the most difficult part is that materials' chemical, electrical and mechanical properties are always coupled and interacted with one another, thus rarely allowing us to independently tune each of them. For example, highly conductive materials (*e.g.* Au) are normally mechanically fragile (low crack onset strain), which will lead to distorted electrical signal transmission under strain imposed by organ/tissue movement. To improve mechanical compliance of these materials, it normally needs to compensate for their electrical properties (*e.g.* lower conductivity). As another example of materials for electrochemical bio-signal transduction, it requires to apply voltage to transduce target bio-signals into electrical signals, while also inevitably oxidizing non-target electroactive species to generate noise. In this case, applying lower voltage will simultaneously lower both the target bio-signal and unwanted noise.

In this thesis, as the building block towards envisioned applications, Chapter 1 firstly introduces the background and design rationales for two fundamental units: bio-signal transduction module (*e.g.* electrochemical biosensing interface) and signal-transmission module (stretchable interconnects). Chapter 2 is focused on describing a material design methodology (based on Pt nanoparticles and p-Phenylenediamine-based permselective membrane), serving as an example of a reliable bio-signal transduction interface to simultaneously improve the sensitivity and selectivity

of enzymatic-based electrochemical sensing. In Chapter 3, we devise a wearable freestanding electrochemical system that enables high-fidelity biomarker data acquisition under body movement in daily activities. As the core, it utilizes the anisotropic conductive film as the substrate for the developed sensing interface (in Chapter 2), coupled with microfluidic housing to achieve strain-isolated biomarker information delivery pathway. Subsequently, in Chapter 4, we integrate this technique with miniaturized iontophoresis interfaces and wearable hybrid control/readout electronics to achieve autonomous sweat extracting and glucose tracking in a day. In the end, in Chapter 5, I presented my preliminary research results for two future directions to use anisotropic conductive film to 1): decouple strain-effect on thin-film conductive materials' conductivity (in bending mode) to achieve compliant electronics and 2) composite with silver-nanowire-based elastomer to achieve strain-resilient stretchable electrochemical sensing materials.

The dissertation of Yichao Zhao is approved.

Ali Mosleh

Dwight C. Streit

Qibing Pei, Committee Co-Chair

Sam Emaminejad, Committee Co-Chair

University of California, Los Angeles

2021

Table of Contents

List of Figures

Acknowledgements

After I graduated from my master program in 2015, I was hesitating between going to industry in China and applying for the Ph.D program in the U.S. At the end, I was convinced myself to pursue my Ph.D degree by a naïve reason - the curiosity about nature - without even thinking whether do I plan to go to academia in the future or not. Today, I am still very proud about making such a big decision based on such a simple and personal motivation. During my Ph.D journey at UCLA, I am very lucky to live and work with many outstanding people, which offers me opportunities to learn a lot of things from their personalities, achievements and experiences in daily lives.

First of all, I would like to thank my parents for letting me grow in a family environment full of happiness and freedom without finical burden since I was born. They set themselves as an example by their behaviors in the daily life to shape me becoming a man of integrity. Their sense of values is deeply rooted in my mind, which always reminds me to be honest to others as well as myself, to embrace success as well as failures and to be socially responsible. I also appreciate their encouragement, understanding and patience when I was facing difficulties, making my own decisions, and made mistakes.

Nest, I would like to thank my advisor, Professor Sam Emaminejad for his mentoring students in accordance with their aptitude. In particular, he always encourages me to approach the research questions from my own perspectives after understanding the current status and fundamental bottlenecks of the target field. Professor Emaminejad not only teaches me basic techniques, communications skills and research altitudes but also his life philosophies which really changes my way to look at the world. I also want to deeply thank Professor Emaminejad's trust on me when

he recruited me as his student and both emotional and intellectual supports on me when I overcome scientific problems.

I also would like to thank my friends and colleagues: Dr. Bo Wang, Haisong Lin, Shuyu Lin, Hanna Hojaiji, Xuanbing Cheng, Wenzhuo Yu, Jiawei Tan, Zhaoqing Wang, Jialun Zhu and so on. I really learned a lot from them and enjoyed talking and working with them during my Ph.D journey. May our friendship grow stronger.

Last but not the least, I want to express my deep appreciation to my girlfriend, Ruikun Li for her companion since 2015. Although we are in different countries in most of the time, we find our way to overcome many difficulties due to physical distance. I also appreciate it that she can quit her job in Beijing and decide to come to the U.S. She makes me a better man.

Vita

2010 – 2014	B.S., Materials Science and Engineering
	Harbin University of Science and Technology
	Harbin, China
2014 – 2015	M.S., Materials Science and Engineering
	Advisor: Professor Mark Hersam
	Northwestern University
	Evanston, IL

Selected publications:

1. **Y. Zhao**, B. Wang, H. Hojaiji, Z. Wang, S. Lin, C. Yeung, H. Lin, P. Nguyen, K. Chiu, K. Salahi, X. Cheng, J. Tan, B. A. Cerrillos, and S. Emaminejad, "A Wearable Freestanding Electrochemical Sensing System", *Science Advances*, 6(12), eaaz0007, DOI: 10.1126/sciadv.aaz0007, 2019.

2. X. Cheng, B. Wang, **Y. Zhao**, H. Hojaiji, S. Lin, R. Shih, H. Lin, S. Tamayosa, B. Ham, P. Stout, K. Salahi, Z. Wang, C. Zhao, J. Tan, and S. Emaminejad, "A Mediator-free Electroenzymatic Sensing Methodology to Mitigate Ionic and Electroactive Interferents' Effects for Reliable Wearable Metabolite and Nutrient Monitoring", *Advanced Functional Materials*, 30(10), 1908507, DOI: 10.1002/adfm.201908507, 2019. (Cover)

3. H. Hojaiji, **Y. Zhao**, M. C. Gong, M. Mallajosyula, J. Tan, H. Lin, A. M. Hojaiji, S. Lin, C. Milla, A. M. Madni, and S. Emaminejad, "An Autonomous Wearable System for Diurnal Sweat Biomarker Data Acquisition", *Lab on a Chip*, DOI: 10.1039/D0LC00820F, 2020. (Cover)

4. **Y. Zhao**, B. Wang, H, Hojaiji, S. Lin, H. Lin, J. Zhu, C. Yeung, and S. Emaminejad, "An Adhesive and Corrosion-Resistant Biomarker Sensing Film for Biosmart Wearable Consumer

Electronics", *IEEE Journal of Microelectromechanical Systems*, 29(5), 1112-1114, DOI: 10.1109/JMEMS.2020.3012101, 2020.

5. H. Hojaiji, **Y. Zhao**, S. Lin, M. C. Gong, M. Mallajosyula, H. Lin, A. M. Hojaiji, A. M. Madni, and S. Emaminejad, "An Autonomous Diurnal Sweat Sampling Patch for Biomarker Data Analytics", *IEEE Journal of Microelectromechanical Systems*, 29(5), 1106-1108, DOI:10.1109/JMEMS.2020.3010537, 2020.

Chapter 1 Introduction

1.1 Analytes accessing in sweat

To explain different kinds of biomarkers partitioning pathways in sweat and their significance, we first need to understand sweat secretion process. Secreted-anions (*e.g*., Cl⁻) will induce electrical potential difference across the cellular lining of sweat secretory coils, leading to attraction of cations (*e.g*., Na⁺) to the cell membranes [1]. The localized cations concentration difference will cause net flux of fluid into sweat secretory lumen due to electro-osmosis effect. In this way, sweat will be secreted and its secretion rate is ranging from 0.1 nL min⁻¹ per gland (under natural perspiration) to > 10 nL min⁻¹ per gland. During the sweat secretion process, biomarkers will partition through different pathways into sweat, which requires different interpretation methods of biomarker information (*e.g*. correlation with blood biomarkers, related with sweat gland activities, *etc*.). For Na⁺ and Cl⁻, since they are the main biomarkers involved into sweat secretion process, they have clinical significance related to sweat gland activities, but have no correlation with blood Na⁺ and Cl⁻ levels. Blood lactate is a very important hydrophilic biomarker to indicate tissue hypoxia, which relates to various disease diagnosis such as sepsis, tissue infections as well as wellness monitoring. Although, lactate molecules from blood/interstitial fluid (ISF) can be diffused into sweat gland, lactate will also be locally produced inside the sweat gland during sweat generation. Therefore, the correlation between sweat lactate and blood lactate is difficult to be established without mitigation of confounding factors caused by sweat generation process. Glucose is another important hydrophilic biomarker related with body's metabolism. In clinics, it is a gold indicator for diabetes diagnosis and very informative for nutrition management.

Many studies have shown the preliminary results to demonstrate the correlation between sweat and blood glucose levels. However, to make this correlation more precise, efforts need to be focused on the large-scale clinical investigation and confounding factors mitigation (*e.g.* sweat rate, sweat pH, *etc.*). Unlike ions and hydrophilic biomarkers, lipophilic molecules (*e.g.* cortisol), by nature, have a good correlation between their blood levels and sweat levels, which seems to be a more promising direction for sensor development to achieve non-invasive biomarker monitoring.

1.2 Electrochemical sensors

In general, electrochemical sensors are developed to transduce biomarker information to current signaling relying on biomolecules interact with sensing electrode under applied voltage. Particularly, here we focused on oxidase-based enzymatic electrochemical sensors to target small molecules such as glucose, lactate, and alcohol. Its underlying sensing mechanism is based on leveraging enzymatic reactions for the simultaneous production/electroanalytical quantification of hydrogen peroxide (H_2O_2), which is generated in proportional amounts to the target molecule's concentration [6]. However, the oxidation voltage of H_2O_2 on conventional noble metal electrodes (*e.g.* Pt) is relatively high, which leads to a poor sensor's selectivity due to interference species redox reactions.

To solve this challenge, there are two methods have been proposed: 1) incorporation of mediator agent (*e.g.* PB) on the electrode to reduce H_2O_2 oxidation potential [2, 6]; 2) incorporation of permselective membrane to reject electroactive species away from electrode surface to significantly increase their redox potential [3, 4, 6]. For the PB-based biosensors, it presents fundamental shortcomings centering on confounding effects due to variation in biofluid conditions, rendering it unsuitable (at current stage) for the envisioned wearable applications that

2

target biofluids with dynamically varying ionic strength and pH. In particular, PB-based wearable sensor responses can be distorted by naturally occurring variation in ionic species' concentration in biofluids, because they rely on ionic species (such as potassium, K^+) for charge compensation and facilitating the intended PB-based redox reactions (*i.e*., reduction to Prussian White, PW, from PB) [3]. characterized in terms of sensor selectivity against non-electroactive ionic species and operational stability. Therefore, it is important to develop mediator-free based electrochemical sensing interface by incorporation of suitable permselective membrane to target biomarkers in real biofluids.

1.3 Stretchable conductors as interconnections [5]

Two main approaches have been widely used for stretchable interconnects development: structure-based and materials-based design. For structure-based stretchable interconnects, thin film metal-substrate composite is fabricated into 2D/3D patterns, which can form in-plane and out-of-plane configuration during tension. Among all these interconnects, serpentine-based stretchable conductors are the most widely adopted interconnect in the stretchable electronics field (as shown in Fig. 1). Depending on the complexity of the serpentine structure, the conductor macroscopic stretchability is in the range from 30% up to 1600%. By leveraging lithography fabrication techniques, the structure-based conductors are particularly compatible with thin-film device integration (sensors, transistors, *etc*.). However, in practical settings, the structure-based conductors are normally encapsulated by elastomer, which its stretchability is significantly degraded due to the constrain of out-of-plane deformation. Additionally, the conductor's stretchability is degraded with increasing elastic modulus of their bonded substrate. The second design approach for stretchable interconnects is to synthesize materials or composites that are

intrinsic stretchable without complex structure engineering. One of the most commonly-used materials is AgNW. It has been demonstrated that a percolation network will be formed once AgNW is coated onto the substrate. Under tension, AgNW network will deform by re-orienting of nanowires at junctions while maintain its structure integrity and high conductivity. Another example, demonstrated by Suji Choi *et al*., is to synthesize Ag-Au nanowire composites with two phases [7]. "Soft" SBS-rich phase is mechanically stretchable under tension while Ag-Au rich phase maintains stable electrical conduction. However, most stretchable conductors are implemented to interconnect physical sensing interface with electronic components. To position it for electrochemical signal transmission, various challenges are yet to be addressed, which includes construction of sensing interface on conductors, elimination of galvanic corrosion under biofluids environment and so on.

1.4 Reference

1   Z. Sonner, E. Wilder, J. Heikenfeld, G. Kasting, F. Beyette, D. Swaile, F. Sherman, J. Joyce, J. Hagen, N. Kelley-Loughnane, R. Naik, *Biomicrofluidics*, 2015, 9, 031301.

2   W. Gao, S. Emaminejad, H. Y. Y. Nyein, S. Challa, K. V. Chen, A. Peck, H. M. Fahad, H. Ota, H. Shiraki, D. Kiriya, D. H. Lien, G. A. Brooks, R. W. Davis, A. Javey, *Nature,* 2016, *529*, 509.

3   X. Cheng, B. Wang, Y. Zhao, H. Hojaiji, S. Lin, R. Shih, H. Lin, S. Tamayosa, B. Ham, P. Stout, K. Salahi, Z. Wang, C. Zhao, J. Tan and S. Emaminejad, *Adv. Funct. Mater.*, 2020, 30, 1908507.

4   Y. Zhao, B. Wang, H. Hojaiji, Z. Wang, S. Lin, C. Yeung, H. Lin, P. Nguyen, K. Chiu, K. Salahi, X. Cheng, J. Tan, B. A. Cerrillos and S. Emaminejad, *Sci. Adv.*, 2020, 6, eaaz0007.

5   N. Matsuhisa, X. D. Chen, Z. A. Bao, and T. Someya, *Chem Soc Rev,* 2019*,* 48, 2946-2966.

6   J. Wang, *Chem Rev,* 2008, 108, 814-825.

7   S. Choi, S. I. Han, D. Jung, H. J. Hwang, C. Lim, S. Bae, O. K. Park, C. M. Tschabrunn,

M. Lee, S. Y. Bae, J. W. Yu, J. H. Ryu, S.‑W. Lee, K. Park, P. M. Kang, W. B. Lee, R. Nezafat,

T. Hyeon, D.‑H. Kim, *Nat. Nanotechnol*. 2018, 13, 1048.

Chapter 2. Enzymatic electrochemical sensing surface design to mitigate ionic and electroactive interferents' Effects

2.1 Introduction

Wearable biomarker sensors present great potential for transforming personalized healthcare and precision medicine, because they allow frequent and convenient harvesting of relevant physiological data from non-invasively accessible biofluid samples such as sweat.[1-9] This information can be used to provide actionable feedback to the user with respect to adopting/modifying lifestyle routines and daily activities such as nutrition and physical exercise. To this end, tracking circulating metabolites (*e.g.*, glucose and lactate) and nutrients (*e.g.*, choline) plays a significant role in rendering a complete view of the body's dynamic chemistry.

To measure these molecules in epidermally-retrievable biofluids, electrochemical sensing interfaces are suitable, because of their simplicity, low cost, and ease of integration with readout electronics to realize sample-to-answer sensing systems.[10-11] To this end, wearable electroenzymatic sensors (a sub-class of electrochemical sensors) have been developed to measure biomarkers such as glucose and lactate in sweat.[1-4] The underlying sensing mechanism for the majority of the demonstrated sensing interfaces is based on leveraging enzymatic reactions for the simultaneous production/electroanalytical quantification of hydrogen peroxide (H_2O_2), which is generated in proportional amounts to the target molecule's concentration.[12] Direct amperometric detection of H_2O_2, using conventional electrodes (e.g., gold, Au, and platinum, Pt) is practically achievable at ~ 0.6 V (versus silver/silver chloride, Ag/AgCl).[13] At this potential, various other electroactive species (*e.g.*, ascorbic acid, AA, and uric acid, UA) can also be oxidized at the electrode surface together with H_2O_2 and interfere in the measurement.[14-15] To address this

issue, previously reported wearable enzymatic sensors commonly incorporate a redox mediator-based layer (*e.g.*, Prussian Blue, PB, also referred to as "artificial peroxidase") to lower the applied potential (close to ~ 0 V) for hydrogen peroxide detection.[16]

However, as widely reported in the context of conventional electrochemical sensors, PB-based sensing presents fundamental shortcomings centering on confounding effects due to variation in biofluid conditions, rendering it unsuitable (at current stage) for the envisioned wearable applications that target biofluids with dynamically varying ionic strength and pH.[1, 17-24] In particular, PB-based wearable sensor responses can be distorted by naturally-occurring variation in ionic species' concentration in biofluids, because they rely on ionic species (such as potassium, K^+) for charge compensation and facilitating the intended PB-based redox reactions (*i.e.*, reduction to Prussian White, PW, from PB, as conceptualized in Figure 2.1a).[17-20] Furthermore, variation in biofluid pH (especially around neutral pH) can lead to the degradation of the PB framework resulting in the loss of its electrocatalytic activity.[21-24] Thus, while electroenzymatic sensing has been realized using PB, its inherent limitations warrant focused efforts aimed at resolving them, or alternatively, necessitate exploration of other sensing methodologies that by design are suitable for sensing operation across diverse biofluid environments with varying compositions.

Here, first, the inherent limitations of PB were studied and characterized in terms of sensor selectivity against non-electroactive ionic species and operational stability. Then, as an alternative methodology for the development of enzymatic sensors well-suited for wearable biofluid sensing, we devise a mediator-free sensing interface (Figure 2.1b). To achieve high sensor selectivity, sensitivity, and stability, our approach leverages: 1) a permselective membrane (poly-*m*-phenylenediamine, PPD) to reject interfering electroactive species;[25-26] 2) a Pt-based electrode,

which is naturally inert against ionic species (unlike PB); and 3) a H_2O_2 electroanalysis layer with Pt nanoparticles (PtNP) electrodeposited onto a multi-wall carbon nanotube (MWCNT) to achieve superior electrocatalytic capability toward the detection of H_2O_2.[27-28]

To demonstrate the versatility of the methodology to target a panel of analytes, as example critical metabolites and nutrients accessible in biofluids such as sweat, we adapted the sensing interfaces to measure glucose, lactate, and choline through immobilizing their respective oxidases. These compounds were selected in particular because tracking their circulating concentration levels can enable actionable feedback to the user and trigger active interventions within a short period, assuming timely notification. For example, sweat glucose has been shown, at least qualitatively, to track blood glucose levels.[29-31] Feedback from non-invasive wearable sensors indicating abnormally high or low levels could enable the awareness and lifestyle adjustment of general users. Similarly, sweat lactate is speculated to be informative of physiological status (*e.g.*, physical stress and aerobic/anaerobic transitions) of individuals.[32-33] Tracking its presence in sweat during a physical activity may inform personalized and real-time performance optimization strategies. Finally, choline is important for general organ function and serves as a precursor to the neurotransmitter acetylcholine.[34-35] Short-term deficiency of choline, which can cause fat accumulation in the liver and other effects, could be reversed within a few days by reintroducing choline to the individual's diet.[34-35]

The devised mediator-free-based sensors were comprehensively characterized from the standpoints of sensitivity, selectivity, and stability, to demonstrate their suitability for the envisioned wearable applications (conceptualized in Figure 2.1c). As shown in Figure 2.1d,e, by integration within a custom-developed smartwatch, containing an optional sweat stimulating iontophoresis module, a wireless sensing system is realized for on-body sweat biomarker data

acquisition and transmission to the cloud server. The versatility of the demonstrated methodology allows for its use to target a wide panel of biomarkers in various biofluids, introducing a new sensor development direction for personal health monitoring applications.

2.2. Experimental Section

2.2.1. Materials and Reagents

Multi-walled carbon nanotubes (MWCNT, carboxylic acid functionalized), Nafion® perfluorinated resin solution (5 wt%), chloroplatinic acid hexahydrate ($H_2PtCl_6 \cdot 6H_2O$), formic acid, *m*-phenylenediamine, bovine serum albumin (BSA), glutaraldehyde solution (25 wt%), polyvinyl chloride, tetrahydrofuran (THF), *D*-(+)-glucose, sodium *L*-lactate, choline chloride, acetylsalicylic acid (aspirin), creatinine, *L*-ascorbic acid, potassium hexacyanoferrate (II) trihydrate, potassium hexacyanoferrate (III), iron (III) chloride, potassium chloride, sodium chloride, uric acid, pilocarpine hydrochloride, metformin hydrochloride, albumin from human serum, sodium hydroxide, glucose oxidase, and choline oxidase were purchased from Sigma-Aldrich (MO, USA). Water (Optima™ LC/MS Grade), *2*-propanol, hydrochloric acid, Honeywell™ hydrogen peroxide solution (30 wt%), and phosphate buffered saline (1 ×, Gibco® PBS, pH 7.2) were purchased from Fisher Scientific (MA, USA). Lactate oxidase was purchased from Toyobo USA, Inc. (NY, USA). Ag/AgCl ink was purchased from Ercon Incorporated (MA, USA). PILOGEL® discs were purchased from ELITechGroup Inc. (UT, USA). PET (100 μm-thick) was purchased from MG Chemicals (BC, Canada). Double-sided tape (170 μm-thick, 9474LE 300 LSE) and Tegaderm™ Film were purchased from 3M Science (MN, USA).

2.2.2. Biosensor Fabrication

The biosensors were fabricated on a pair of Au electrodes (diameter: 4 mm, 30 nm Cr/100 nm Au) deposited and patterned on a PET substrate. The reference electrode was fabricated by depositing 3.2 μL of Ag/AgCl ink on the Au electrode, then dried on a hot plate at 70 °C for 20 min.

To fabricate PB-based sensors, PB was electrochemically deposited onto the Au electrode by CV from 0 V to 0.5 V (versus Ag/AgCl) for 1 cycle at 20 mV s^{-1} in a fresh PB solution containing 2.5 mM $FeCl_3$, 2.5 mM $K_3[Fe(CN)_6]$, 100 mM KCl, and 100 mM HCl. After the deposition, the sensors were dried on a hot plate at 100 °C for 1 hour.

To fabricate PtNP-based sensors, PtNP were electrochemically deposited onto the Au electrode by chronoamperometry at –0.1 V (versus Ag/AgCl) for 10 min in a fresh Pt-solution (containing 2.5 mM H_2PtCl_6 and 1.5 mM formic acid).[58-59] A PPD layer was subsequently electrochemically deposited onto the Au/PtNP electrode by applying 0.85 V (versus Ag/AgCl) for 120 s in a fresh PBS solution (1 ×) containing 5 mM *m*-phenylenediamine.

To fabricate the MWCNT/PtNP-based sensors, a multi-walled carbon nanotube solution was first prepared by mixing MWCNT (2 mg mL^{-1}) with 5 wt% Nafion solution followed by ultrasonic agitation for over 30 min to form a viscous solution of carbon nanotubes. 3.2 μL of the MWCNT solution was drop-cast onto the Au electrode and dried in the ambient environment. PtNP were later electrochemically deposited onto the MWCNT deposited Au electrode via CV from –1.0 V to 0 V (versus Ag/AgCl) for 20 cycles at 50 mV s^{-1} in the fresh Pt-solution. A PPD layer was electrochemically deposited onto Au/MWCNT/PtNP following the same method. In order to prepare the biosensors, the electrode was further functionalized with an enzymatic layer. The BSA stabilizer solution was prepared by adding 0.8% (v/v) of 25 wt% glutaraldehyde solution into a

fresh PBS solution containing 10 mg mL^{-1} BSA. To develop the glucose sensor, the aforementioned BSA stabilizer solution was mixed thoroughly with a glucose oxidase solution (50 mg mL^{-1} in PBS, pH 7.2) at a ratio of 1:1 (v/v). By drop casting 3.2 μL of the glucose enzyme mixture onto the Au/MWCNT/PtNP/PPD electrode, the glucose sensing interface was realized. To realize the choline sensor, the BSA stabilizer solution was mixed thoroughly with a choline oxidase solution (10 mg mL^{-1} in PBS, pH 7.2) at a ratio of 1:1 (v/v). The choline sensing interface was constructed by drop-casting 3.2 μL of the choline enzyme mixture onto the Au/MWCNT/PtNP/PPD electrode. To create the lactate sensor, the BSA stabilizer solution was mixed thoroughly with a lactate oxidase solution (50 mg mL^{-1} in PBS, pH 7.2) at a ratio of 1:1 (v/v). 3.2 μL of the mixture was deposited onto the Au/MWCNT/PtNP/PPD electrode and dried at room temperature, followed by dip-coating of PVC solution (3 wt% in THF) to form a lactate diffusion limiting layer. Sensors were allowed to dry overnight at 4 °C, while being protected from light. The sensors were stored at 4 °C when not in use.

2.2.3. Microfluidic Interface Construction

The microfluidic interface was created by laser-cutting (Epilog Mini 24, Epilog Laser) two-dimensional patterns within the double-sided tape and Tegaderm™ Film. The inlet was created by laser-cutting holes on the PET layer. The outlet was created by laser-cutting holes on the double-sided tape backing layer. The microfluidic interface was then assembled by attaching one layer of pre-patterned double-sided tape with a pre-patterned transparent PET film sheet, and one layer of pre-patterned Tegaderm™ Film with proper alignment.

2.2.4. Biosensor Characterization and Analytes Measurement

To characterize the developed PB-based sensing interface, CV measurements were conducted in 0.1 M KCl solution from –0.2 V to +0.4 V at a scan rate of 50 mV s^{-1}. Constant potential amperometric measurements were conducted in constantly-stirred PBS buffer ($1 \times$ or $0.2 \times$ diluted with 1 mM KCl) at 0 V (versus Ag/AgCl). By stepwise addition of different concentrations of H_2O_2 in the PBS buffer, a series of calibration plots were obtained. To characterize the K^+ responses of the PB-based sensing interface, CV measurements were conducted in $0.2 \times$ diluted PBS from –0.1 V to +0.6 V (versus Ag/AgCl) at a scan rate of 50 mV s^{-1}. Before each measurement, different concentrations of KCl were introduced into the PBS buffer.

To characterize the developed PtNP-based sensing interface, chronoamperometric measurements were conducted in constantly-stirred PBS buffer ($1 \times$ PBS or $0.2 \times$ diluted PBS with 1 mM KCl) at +0.5 V (versus Ag/AgCl). By stepwise addition of different concentrations of the targets (*e.g.*, H_2O_2, glucose, lactate or choline) in PBS buffer with corresponding sensors, a series of calibration plots were obtained. The limit of detection (LOD) for each amperometric sensing interface was calculated as LOD = 3*SD/ (slope of calibration curve), where SD is the standard deviation of the baseline noise in the blank solution and slope is defined as amperometric current change versus target concentration change. Sensitivity is calculated as the slope divided by sensor's surface area. The sensor selectivity tests were conducted by stepwise addition of different interferents into the PBS, including glucose/lactate/choline, creatine, KCl, NaCl, UA, AA, pilocarpine, aspirin, metformin, and albumin. The target analytes were also introduced into the solutions after the interferents.

2.2.5. Glucose and Lactate Quantification with Lab Instrument

The glucose and lactate concentration levels from untreated human sweat samples were directly quantified with a YSI 2900 analyzer (YSI Incorporated, OH, USA).

2.2.6. Characterization of Sensors Morphologies and Chemical Composition Distributions

The sensor morphologies were characterized by field emission scanning electron microscopy (FE-SEM) (ZEISS Supra 40VP, Germany). Chemical compositions distributions were characterized by energy dispersive spectroscopy (EDS) (Thermo^{TM} NORAN System 6, USA).

2.2.7. On-body Tests Using the Mediator-free Sensor-integrated Smartwatch:

The mediator-free sensor was transferred onto the disk contact located at the back of the custom-developed sensing smartwatch. Then, the microfluidic interface was transferred on top of the sensor before being attached to a healthy human subject's wrist. The smartwatch case was customized and three-dimensionally printed to consolidate the smartwatch components, which include LCD display, battery, printed circuit board (PCB) module, sensor, and microfluidic interface. To induce sweat by iontophoresis, a subject's stimulated skin area was first cleaned with deionized water and ethanol, followed by sweat gland stimulation by iontophoresis for 5 minutes.

2.2.8. Wireless PCB Module

The wearable PCB module is designed to activate and control the sweat stimulation and sensing circuits, and to process and communicate the obtained data wirelessly upon user commands. This circuit consists of several layers to enclose the iontophoresis and sensing

modules. The main PCB section is connected to the iontophoresis module through metallic connections. This layer also encapsulates a flat flexible cable connection to interface with the sensor. Utilizing an anisotropic conductive film, the flexible cable was connected to the fabricated flexible electrodes.

The required sweat stimulation circuitry driving the iontophoresis electrodes consists of a current source, where the current applied is independent of the user's skin type (impedance). The current levels are controlled through user command and via the digital-to-analog (DAC) port of the microcontroller. This current is limited through the current limiting circuits implemented on board and constantly monitored by the microcontroller (STM8L – UFQFN20, STMicroelectronics) to apply the minimal current set by the user in the comfortable range of 0.1 – 1.5 mA.

After the iontophoresis process is done, the sensing mode is activated. At this stage, the microcontroller will activate the LMP91000 potentiostat chip (Texas Instruments) through I2C-controlled signals. This chip is programmed to apply +0.5 V across the working and reference electrodes connected to the sensor. Then, to filter out high-frequency interference and the user's motion artifacts, the output voltage of the potentiostat's internal transimpedance amplifier is passed through a fifth-order low-pass filter (LPF). The LPF was applied using a MAX7422 chip (Maxim Integrated) with a cut-off frequency of 1 Hz. Through the microcontroller's built-in 12-bit Analog-to-Digital (ADC) unit then converts the processed analog output of the LPF into the digital domain for real time biomarker monitoring which is then plotted on the LCD (st7735 – TFT-LCD, Sitronix Technology Corporation) and transfers this data to the user's smartphone.

To power the PCB, a single miniaturized rechargeable lithium-ion polymer battery with a nominal voltage of 3.7 V was used. Additionally, in this design, we obtained low/ultra-low power

components to make the device wearable and feasible for on-body testing. For our specific application and duration of tests, we characterized that peak supply current levels on the order of 100 mA must be drawn from the battery. This requirement can vary based on different modes and durations of applications.

2.2.9. Smartphone Application and Smartwatch Design

User commands and data are bilaterally communicated between the PCB module and the custom-developed Android application through Bluetooth communication. In this application, we designed graphical interfaces for each mode to plot the output current (applied in the iontophoresis mode) and the sensing results. Additionally, the data received is time stamped, analyzed, and stored locally for future reference. This stored data can then be sent to a custom-developed Google Cloud platform for further analysis.

2.2.10. Institutional Review Board (IRB) Approval for Human Subject Testing:

The conducted human subject experiments were performed in compliance with the protocols that are approved by the IRB at the University of California, Los Angeles (IRB#17-000170). All subjects gave written informed consent before participation in the study.

2.3. Characterization of PB-based Sensors' Limitations for Sweat-based Analysis

The core functionality of the electroenzymatic sensor is the sensitive and selective detection of H_2O_2, which is the byproduct of the oxidase-based reactions. However, sensitive detection of H_2O_2 with conventional electrodes (*e.g.,* Pt and Au) usually requires a high applied potential (*e.g.,* > 0.6 V versus Ag/AgCl).[13] At this potential, electroactive interferents (*e.g.,* UA, and AA)

in the biofluid matrix can also be oxidized and could mask the desired H_2O_2 signals.[14-15] To lower the applied potential, the majority of wearable electroenzymatic sensors rely on Prussian Blue ($KFe^{III}[Fe^{II}(CN)_6]$), considered as an "artificial peroxidase") as a mediating layer to reduce the applied potential to near 0 V, and thus, to minimize the influence of electroactive interferents.[1-4]

However, inherent limitations of the PB-based interface may make it unsuitable (at current stage) for epidermally-retrieved biofluid analysis. To illustrate this point, here, following the previously reported protocols, PB-based H_2O_2 sensors were fabricated on Au-electrode patterned polyethylene terephthalate (PET) substrates (Figure 2.2 (S1) confirms the successful deposition of PB on Au).[1-3, 36] Then, the shortcomings of the PB-based interface were characterized from the perspective of sensor selectivity against ionic species and operational stability.

2.3.1. Sensor Selectivity against Ionic Species

Even though PB-based H_2O_2 sensing has been demonstrated with low applied potential to achieve selectivity against non-target electroactive species, the interfering effect of non-electroactive ionic species has often been overlooked. The latter group of species participate in the charge compensation mechanisms for the conversion of PB to PW ($K_2Fe^{II}[Fe^{II}(CN)_6]$). The catalytic capabilities of PB are generally attributed to its unique zeolite crystal structure (a coordination complex with Fe^{II} and Fe^{III} ions alternating in face centers of a cubic lattice, where cyanide ions CN^- act as ligands between the two iron states).[22] Given the PB lattice's characteristic channel radius of 0.16 μm, the relatively smaller non-electroactive ionic species can diffuse to the interior of the structure, where they can intercalate among Fe^{II} and Fe^{III} ions and participate in redox conversion of PB to PW.[22] These ionic species include hydrated cations

16

with smaller radii, such as K^+ (0.125 μm), Rb^+ (0.128 μm), Cs^+ (0.119 μm), and NH_4^+ (0.125 μm).[36-38] Among these cations, K^+ is of particular importance in wearable biomarker sensing applications due to its high abundance and inter/intra-subject variation in sweat.[39-41]

The involvement of K^+ in the PB-based mediation of the H_2O_2 reduction can be illustrated by the equations outlined below (Figure 2.3 (2a):[16, 22]

$$PB + e^- + K^+ \rightarrow PW \tag{1}$$

$$H_2O_2 + PW \rightarrow OH^- + PB + K^+ \tag{2}$$

The processes in Equation (1) and subsequently Equation (2) are directly influenced by K^+ concentration variation (with a response time larger than 20 s, as illustrated in Figure 2.4 (S2)). To investigate this effect, as shown in Figure 2.3b, 2.5(S3), cyclic voltammetry (CV) measurements were performed with the fabricated PB-based sensors in a buffer with a physiologically relevant ionic strength (here, similar to that of sweat). Figure 2.3c (2c) indicates that with the higher K^+ concentration level in the buffer, the larger subsidiary cathodic peak current level (a measure of the PB-to-PW conversion) was observed, which can lead to the conclusion that the K^+ concentration level has a direct effect on the PB/PW redox reaction rate.[17-20] This phenomenon is critical to the envisioned sweat sensing application, because the PB/PW redox reaction rate influences the reaction rate of H_2O_2 reduction, and subsequently the measured current. Accordingly, because the K^+ of the target sample is unknown (unless measured by an auxiliary sensor) and differs from that of the calibrator sample, pre/post-calibration-based techniques can not be simply used to relate the measured current to the target analyte's concentration level.

2.3.2. Operational Stability

Another fundamental limitation of PB-based sensors is its operational stability. A number of studies have reported and characterized the degradation of the PB layer in aqueous solutions, especially in alkaline environments.[21, 42] Efforts have been made to improve the stability of PB structure, but the fabrication methods are typically complicated and time-consuming.[42-44] The reason for the instability of the PB structure is likely due to the strong interaction between Fe^{III} ions and hydroxyl ions (OH^-), which can be attributed to inherent buffer conditions (especially, when operating at a pH higher than 6.4) and the H_2O_2 reduction.[45] To better understand this point, it is worth referring to Equation (3):[22, 24]

$$KFe^{III}[Fe^{II}(CN)_6] + 3OH^- \rightarrow Fe(OH)_3 + [Fe^{II}(CN)_6]^{4-} + K^+ \qquad (3)$$
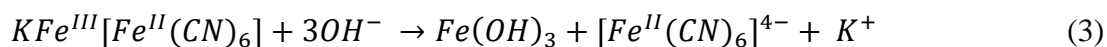
As described by Equation (3), the interaction of PB and OH^- leads to the destruction of the Fe-CN-Fe bond by forming Fe-OH and the leakage of hexacyanoferrate (II) ions from the PB structure, resulting in the dissolution of the deposited PB on the electrode (Figure 2.3d (2d)).[46]

To characterize the operational stability of PB, continuous CV scanning (Figure 2.3e (2e)) was first conducted at pH = 5, 7, and 8.5 (spanning across the physiological relevant range of sweat pH).[47-49] As shown in Figure 2.3e (2e), at pH = 5, the cathodic peak currents of the PB redox reaction decreased linearly over the course of the CV recordings. When changing to neutral and alkaline pH environments (pH = 7 and pH = 8.5), the peak currents decreased sharply and vanished after 150 cycles (80 min) and 50 cycles (27 min), respectively, indicating the degrading effect of the OH^- interaction with PB (visualized in the inset of Figure 2.3d (2d)). Similar trends were also observed when immersing the fabricated PB-based sensors in the aforementioned buffers for a similar time period (where five CV measurements were performed, one every half an hour, Figure

18

2.6 (S4)). These results demonstrate the loss of the PB electroactivity over time, rendering PB unsuitable for H_2O_2-based sensing in biofluid environments.

Reduction of H_2O_2 also contributes to the deleterious effects of OH^- on sensor stability.[16] To characterize this phenomenon, the sensitivity of H_2O_2 detection was evaluated over six rounds of H_2O_2 calibration at neutral pH. As shown in Figure 2.3f(2f) and 2.7(S5), the PB-based H_2O_2 sensor exhibited reduced current responses in consecutive rounds of testing. Figure 2.3g (2g) further illustrates that the sensor's sensitivity decreased dramatically (> 76%) after six rounds of calibrations across three sensors. A distinct hysteresis behavior was also observed when measuring the PB-based sensing interface's current responses with increasing and then decreasing H_2O_2 concentration levels in the testing buffer (Figure 2.8(S6)). These phenomena could be attributed to the destruction of the PB structure by OH^-, which, in this case, can be generated by the reduction of H_2O_2.

Furthermore, the dynamic range of the PB-based sensor for H_2O_2 detection was also evaluated. Figure 2.3h (2h) shows that the reduction current increased linearly with the H_2O_2 concentration from 50 μM to 600 μM. However, a significant current drop was shown beyond 600 μM H_2O_2, which can be related to the limited availability of PB on the sensor surface as well as the degrading OH^- interactions.[50] It is worth mentioning that increasing the thickness of PB layer on the sensor surface has been shown to increase the dynamic range of H_2O_2 detection because of the increased availability of electroactive PB on the sensor surface.[1, 50] However, this increase in dynamic range comes at the expense of longer H_2O_2 response time and lower H_2O_2 detection sensitivity.[50]

2.4. Optimization and Characterization of PtNP-based Sensors

Given the characterized shortcomings of PB-based sensing interfaces, as an alternative wearable enzymatic sensing approach, we devised a mediator-free electroenzymatic sensing interface, which centers on the measurement of H_2O_2 with high sensitivity, selectivity and stability to facilitate the reliable quantification of target biomarkers in complex biofluids.

Platinum is reported to be capable of catalyzing the oxidation of H_2O_2 directly with high sensitivity.[13, 26] By electrochemically depositing PtNP onto the Au electrode, a H_2O_2 electroanalysis layer was realized to effectively oxidize H_2O_2 (by applying +0.5 V versus Ag/AgCl). Figure 2.9a(3a) shows the response of such layer to various H_2O_2 concentrations in a range from 50 μM to 1.1 mM. The detectable range is twice that of the PB-based sensing interface and can be attributed to the mediator-free nature of the PtNP-based sensing interface. The PtNP-based interface exhibited minimal H_2O_2 detection sensitivity variations and minimal current response change through multiple rounds of calibrations, as illustrated in Figure 2.9b(3b) and 2.10(S7) (six rounds), indicating the inherent stability of the interface.

In addition, without any mediating reactions involved in the H_2O_2 detection, the PtNP-based sensing interface is inherently not prone to interference from variation in ionic species concentration levels in the biofluid matrix (unlike PB-based sensing). To illustrate the influence of ionic species, PB- and PtNP-based sensors were utilized to estimate the H_2O_2 concentration level from samples with an elevated K^+ level compared to that of the calibrators (7 mM versus 1 mM). As shown in Figure 2.9c(3c), the PB-based sensing interface over-estimated the H_2O_2 concentration by 94%, whereas the PtNP-based interface enabled an accurate estimation of the H_2O_2 concentration. Similar superior estimation ability was obtained in glucose measurements utilizing the glucose oxidase modified sensing interface (Figure 2.11(S8)). Given the variation of

20

K$^+$ in biofluids (*e.g.,* sweat), these results indicate that the PtNP-based sensing interface is expected to give more reliable readings for the envisioned wearable applications as compared to conventional PB-based sensing interfaces.

For reliable electroenzymatic analysis, the sensing interface needs to be further modified to achieve selectivity against the electroactive interfering species. To understand the context, it is worth noting that when applying +0.5 V (versus Ag/AgCl) at the working electrode, electroactive interferents in the biofluid such as UA and AA can also undergo reactions, confounding the H$_2$O$_2$ current response.[14-15] To this end, a permselective membrane (here, PPD) was incorporated, which only allows the passage of small and neutral molecules (e.g., H$_2$O$_2$) to reach the electroanalysis layer. However, the incorporated permselective membrane will inevitably act as a diffusion limiting layer as well, impairing the H$_2$O$_2$ detection sensitivity (Figure 2.9d(3d)). To regain the H$_2$O$_2$ detection sensitivity, a Nafion-dispersed MWCNT layer was incorporated prior to the PtNP electrodeposition, which provides a larger electrocatalytic surface area for the H$_2$O$_2$ electroanalysis. This new MWCNT/PtNP/PPD-based interface exhibited more than eight times the sensitivity of the PtNP/PPD-based interface (Figure 2.9d(3d)). A representative real-time current response of the MWCNT/PtNP/PPD-based interface to H$_2$O$_2$ is shown in Figure 2.9e(3e). It is worth mentioning that the demonstrated sensitivity to H$_2$O$_2$ is superior to those reported previously.[27, 51]

To evaluate the selectivity of the MWCNT/PtNP/PPD-based interface, interfering electroactive species (UA and AA) and ions (K$^+$ and Na$^+$) were introduced (at physiologically relevant levels) to the sensor. Figure 2.9f(3f) shows that the recorded response to these interfering species was minimal as compared to the H$_2$O$_2$ response, validating the intended utility of the deposited permselective membrane and the mediator-free sensing mechanism.

To characterize the morphology of the (Nafion-)MWCNT/PtNP/PPD sensing interface and to confirm the homogenous distribution of the elements in each layer of the interface, scanning-electron microscopy coupled with energy dispersive spectroscopy (SEM-EDS) was performed (Figure 2.9g(3g)). As shown in Figure 2.9g(3g) (I), the characterized particle sizes ranged from 200 to 500 nm, which falls within the expected range of the feature sizes. As further shown in Figure 2.9g(3g) (II-IV), a homogeneous element distribution was observed in each functional layer.

2.5. Development and Characterization of Electroenzymatic Sensors Based on the MWCNT/PtNP/PPD Interface

By the oxidase-based functionalization of the MWCNT/PtNP/PPD-based interface, its excellent H_2O_2 sensing performance can be leveraged to develop electroenzymatic sensors targeting various metabolites and nutrients. Here, specifically, this interface is adapted to target glucose, lactate, and choline by the modification of the interface with the respective oxidases. Figure 2.12(a-c)(4a-c) show the corresponding real-time chronoamperometric current responses of representative glucose, lactate, and choline sensors (working electrode diameter: 4 mm) within the physiological relevant concentration ranges of the respective analytes (glucose: 0 – 300 μM, lactate: 0 – 20 mM, and choline: 0 – 300 μM).[1, 52-53] Linear relationships between the sensor current responses and target analyte concentration levels were observed for all the demonstrated sensors, with measured sensitivities of 59 ± 12 μA mM^{-1} cm^{-2} for glucose sensors, 0.79 ± 0.18 μA mM^{-1} cm^{-2} for lactate sensors, and 68 ± 5 μA mM^{-1} cm^{-2} for choline sensors (all with high degrees of reproducibility and reversibility, as shown in Figure 2.13(S9) and 2.14(S10), respectively).

It is worth noting that, even though the sensing mechanisms of the demonstrated sensors are all based on the H_2O_2 sensing, the functionalization methods are different in terms of the use of different oxidases and diffusion limiting layers (in the case of the lactate sensor), all of which may affect the generation rate of H_2O_2 and the amount of H_2O_2 that can approach the electroanalysis layer (all sensors' schematics in Figure 2.15(S11)). In the context of sweat lactate sensing, due to the fact that Michaelis constant for lactate oxidase is only ~1 mM, while sweat lactate concentration level is exceptionally high (~5 – 20 mM), without any provision, the sensor signal saturates.[1, 52, 54] Therefore, here, we incorporated a diffusion-limiting layer (*i.e.,* polyvinyl chloride, PVC) which allows for the extension of the lactate sensor dynamic range to span across the physiological concentration range of sweat lactate.[4, 54]

In order to ensure the sensors' reliable performance in complex biofluids, comprehensive selectivity tests were conducted by measuring chronoamperometric current responses of the developed sensors towards a diverse panel of interfering species within their physiological concentration ranges in sweat. As listed in Figure 2.12(4d), this panel of interfering species includes small molecules, ionic species, electroactive species, a sweat agonist, xenobiotic drugs, and a protein. As shown in Figure 2.12(4e-g), the developed glucose, lactate, and choline sensors showed negligible current responses towards all the interfering species, and significant stepwise current increases were recorded upon the introduction of the sensor-specific target molecules.

Long-term stability of the electroenzymatic sensor was also examined, and accordingly, the response of an exemplary glucose sensor was recorded over a 20-hour period, while different glucose concentration levels were introduced. As shown in Figure 2.12(4h), throughout the entire test period, the sensor maintained a relatively constant response for each glucose concentration

23

level with minimal current drift ($< 6.5\%$), indicating the excellent long-term stability and robustness of the developed sensor.

2.6. Ex-situ and In-situ Sweat Analysis Using Mediator-free Electroenzymatic Sensing

The utility of the mediator-free electroenzymatic sensing for glucose, lactate, and choline quantification was validated by performing electrochemical analysis in artificial sweat samples (five per sensor) and untreated human sweat samples (iontophoretically- or exercise-induced, three per sensor), and comparing the results with expected values. As shown in Figure 2.16a-c (5a-c), the sensor-estimated glucose, lactate, and choline concentration levels closely matched the expected values ($R^2_{Glucose} = 0.99$, $R^2_{Lactate} = 0.80$, and $R^2_{Choline} = 0.98$). The results collectively indicate the suitability of the devised mediator-free sensing approach to quantify metabolites and nutrients in complex biofluids.

To demonstrate the suitability of the developed sensors for wearable applications, an electrochemical enzymatic sensing system was developed in the form of a smartwatch (Figure 2.16d(5d), 2.17(S12)), which consists of: 1) an optional iontophoresis module which can apply current on-demand to deliver sweat agonist (pilocarpine) underneath the skin for sweat stimulation (Figure 2.17(S12)); 2) a microfluidic interface for sweat sampling and routing to the sensor surface (Figure 2.18(S13)); 3) a mediator-free electroenzymatic sensor for biomarker analysis (glucose and lactate as example target biomarkers); 4) a custom-developed wireless readout circuitry for signal acquisition, processing, and wireless data communication to a mobile application (Figure 2.17(S12)); and 5) an liquid-crystal display (LCD) for real-time data display.

The smartwatch was first coupled with the glucose sensor and utilized to monitor the sweat glucose change in three subjects before and after consumption of mixed meals (where standard

iontophoresis protocol was performed 2 hours before and 0.5 hour after meal consumption in order to induce and subsequently analyze sweat). Figure 2.16e-g (5e-g) demonstrate the elevation of sweat glucose concentration level after meal consumption (in all three subjects), which is in agreement with a trend observed previously.[3, 55-56]

Additionally, the smartwatch was coupled with the lactate sensor and used for continuous sweat lactate profile monitoring of a subject engaged in constant-load stationary cycling. As illustrated in Figure 2.16h(5h) (solid green), a decreasing profile of sweat lactate current responses were recorded, similar to that observed previously.[4, 57] The control experiment conducted on the same subjects with a non-functionalized system (without lactate-oxidase modification) yielded the recording of minimal current response (Figure 2.16h(5h), dashed black). Altogether, the on-body studies illustrate the suitability of the mediator-free electroenzymatic sensing for wearable applications.

2.7 Conclusion

In this study, we characterized the performance of PB-based sensing to demonstrate its limitations in terms of: 1) sensor response susceptibility to ionic species (e.g., K^+), the concentration levels of which dynamically vary in biofluids (e.g., such as sweat), practically leading to severe inaccurate estimation of the end-product of the enzymatic reaction (i.e., H_2O_2), and subsequently, the target biomarkers concentration levels, and 2) degradation of the PB framework (i.e., zeolite crystal structure) caused by OH^-, resulting in poor operational stability. These results indicate that either significant efforts are required to further study and optimize PB-based sensors for reliable wearable biofluid analysis or alternative sensor development methodologies may need to be adopted. Aligned with the latter point, a mediator-free

electroenzymatic sensing methodology is devised, which centers on utilizing a sensing interface comprised of a coupled MWCNT/PtNP layer and a permselective membrane (PPD). Through functionalization with appropriate oxidases, this interface was used to develop glucose, lactate, and choline sensors. The developed sensors were comprehensively characterized from the standpoints of sensitivity, selectivity, stability, and reliability of sensing operation in untreated sweat samples. To further demonstrate their suitability for the envisioned wearable applications, the glucose and lactate sensors were integrated with a custom-developed smartwatch, rendering on-body sweat biomarker data acquisition.

By tuning the materials of the devised functional layers (*e.g.,* permselective membrane or the enzyme layer) as well as by utilizing auxiliary (*e.g*., temperature and pH) sensors, the demonstrated mediator-free sensing methodology can be adapted to accurately measure a broad range of biomarkers in various biofluids. In this way, the presented methodology can serve as a basis for the future wearable electroenzymatic sensor development efforts toward personal health monitoring applications.

2.8. Reference

1   W. Gao, S. Emaminejad, H. Y. Y. Nyein, S. Challa, K. V. Chen, A. Peck, H. M. Fahad, H. Ota, H. Shiraki, D. Kiriya, D. H. Lien, G. A. Brooks, R. W. Davis, A. Javey, *Nature,* 2016, 529, 509.

2   H. S. Lin, Y. C. Zhao, S. Y. Lin, B. Wang, C. Yeung, X. B. Cheng, Z. Q. Wang, T. Y. Cai, W. Z. Yu, K. King, J. W. Tan, K. Salahi, H. Hojaiji, S. Emaminejad, *Lab Chip,* 2019, 19, 2844.

3   S. Emaminejad, W. Gao, E. Wu, Z. A. Davies, H. Y. Y. Nyein, S. Challa, S. P. Ryan, H. M. Fahad, K. Chen, Z. Shahpar, S. Talebi, C. Milla, A. Javey, R. W. Davis, *Proc. Natl. Acad. Sci., U. S. A.* 2017, 114, 4625.

4   S. Imani, A. J. Bandodkar, A. M. V. Mohan, R. Kumar, S. F. Yu, J. Wang, P. P. Mercier, *Nat. Commun.,* 2016, 7, 11650.

5   A. Koh, D. Kang, Y. Xue, S. Lee, R. M. Pielak, J. Kim, T. Hwang, S. Min, A. Banks, P. Bastien, M. C. Manco, L. Wang, K. R. Ammann, K. I. Jang, P. Won, S. Han, R. Ghaffari, U. Paik, M. J. Slepian, G. Balooch, Y. G. Huang, J. A. Rogers, *Sci. Transl. Med.,* 2016, 8, 366ra165.

6   J. Kim, A. S. Campbell, J. Wang, *Talanta,* 2018, *177*, 163.

7   H. Y. Y. Nyein, M. Bariya, L. Kivimaki, S. Uusitalo, T. S. Liaw, E. Jansson, C. H. Ahn, J. A. Hangasky, J. Q. Zhao, Y. J. Lin, T. Happonen, M. H. Chao, C. Liedert, Y. B. Zhao, L. C. Tai, J. Hiltunen, A. Javey, *Sci. Adv.,* 2019, 5, eaaw9906.

8   A. Hauke, P. Simmers, Y. R. Ojha, B. D. Cameron, R. Ballweg, T. Zhang, N. Twine, M. Brothers, E. Gomez, J. Heikenfeld, *Lab Chip,* 2018, 18, 3750.

9   J. Kim, I. Jeerapan, S. Imani, T. N. Cho, A. Bandodkar, S. Cinti, P. P. Mercier, J. Wang, *ACS Sens.,* 2016, 1, 1011.

10   W. Gao, H. Y. Y. Nyein, Z. Shahpar, H. M. Fahad, K. Chen, S. Emaminejad, Y. J. Gao, L. C. Tai, H. Ota, E. Wu, J. Bullock, Y. P. Zeng, D. H. Lien, A. Javey, *ACS Sens.,* 2016, 1, 866.

11   L. C. Tai, W. Gao, M. H. Chao, M. Bariya, Q. P. Ngo, Z. Shahpar, H. Y. Y. Nyein, H. Park, J. Sun, Y. Jung, E. Wu, H. M. Fahad, D. H. Lien, H. Ota, G. Cho, A. Javey, *Adv. Mater.,* 2018, 30, 1707442.

12   S. B. Bankar, M. V. Bule, R. S. Singhal, L. Ananthanarayan, *Biotechnol. Adv.,* 2009, 27, 489.

13   G. G. Guilbault, G. J. Lubrano, *Anal. Chim. Acta,* 1973, 64, 439.

14   A. A. Karyakin, E. E. Karyakina, L. Gorton, *Talanta,* 1996, 43, 1597.

15   H. Zhang, Y. J. Yin, P. Wu, C. X. Cai, *Biosens. Bioelectron.,* 2012, 31, 244.

16   A. A. Karyakin, E. E. Karyakina, L. Gorton, *Electrochem. Commun.,* 1999, 1, 78.

17   J. Q. Ang, T. T. N. Binh, C. S. Toh, *Sens. Actuators, B* 2011, 157, 417.

18   V. Krishnan, A. L. Xidis, V. D. Neff, *Anal. Chim. Acta,* 1990, 239, 7.

19   J. Q. Ang, B. T. T. Nguyen, Y. Huang, C. S. Toh, *Electrochim. Acta,* 2010, 55, 7903.

20   B. T. T. Nguyen, J. Q. Ang, C. S. Toh, *Electrochem. Commun.,* 2009, 11, 1861.

21   F. Ricci, A. Amine, G. Palleschi, D. Moscone, *Biosens. Bioelectron.,* 2003, 18, 165.

22   R. Koncki, *Crit. Rev. Anal. Chem.,* 2002, 32, 79.

23   D. E. Stilwell, K. H. Park, M. H. Miles, *J. Appl. Electrochem.,* 1992, 22, 325.

24   J. M. Noel, J. Medard, C. Combellas, F. Kanoufi, *Chemelectrochem,* 2016, 3, 1178.

25   X. M. Wen, B. Wang, S. Huang, T. Y. Liu, M. S. Lee, P. S. Chung, Y. T. Chow, I. W. Huang, H. G. Monbouquette, N. T. Maidment, P. Y. Chiou, *Biosens. Bioelectron.,* 2019, 131, 37.

26   B. Wang, B. Koo, L. W. Huang, H. G. Monbouquette, *Analyst,* 2018, 143, 5008.

27   S. Hrapovic, Y. L. Liu, K. B. Male, J. H. T. Luong, *Anal. Chem.,* 2004, 76, 1083.

28   S. K. Vashist, D. Zheng, K. Al-Rubeaan, J. H. T. Luong, F. S. Sheu, *Biotechnol. Adv.,* 2011, 29, 169.

29   J. Moyer, D. Wilson, I. Finkelshtein, B. Wong, R. Potts, *Diabetes Technol. Ther.,* 2012, 14, 398.

30   Y. J. Hong, H. Lee, J. Kim, M. Lee, H. J. Choi, T. Hyeon, D. H. Kim, *Adv. Funct. Mater.,* 2018, 28.

31   H. Lee, C. Song, Y. S. Hong, M. S. Kim, H. R. Cho, T. Kang, K. Shin, S. H. Choi, T. Hyeon, D. H. Kim, *Sci. Adv.,* 2017, 3, e1601314.

32   Z. Sonner, E. Wilder, J. Heikenfeld, G. Kasting, F. Beyette, D. Swaile, F. Sherman, J. Joyce, J. Hagen, N. Kelley-Loughnane, R. Naik, *Biomicrofluidics,* 2015, 9, 031301.

33   P. J. Derbyshire, H. Barr, F. Davis, S. P. J. Higson, *J. Physiol. Sci.,* 2012, 62, 429.

34   S. H. Zeisel, K. A. da Costa, *Nutr. Rev.,* 2009, 67, 615.

35   S. H. Zeisel, *J. Am. Coll. Nutr.,* 1992, 11, 473.

36   K. Itaya, I. Uchida, V. D. Neff, *Acc. Chem. Res.,* 1986, 19, 162.

37   K. Itaya, T. Ataka, S. Toshima, *J. Am. Chem. Soc.,* 1982, 104, 4767.

38   F. Ricci, G. Palleschi, *Biosens. Bioelectron.,* 2005, 21, 389.

39   A. J. Bandodkar, J. Choi, S. P. Lee, W. J. Jeang, P. Agyare, P. Gutruf, S. Q. Wang, R. A. Sponenburg, J. T. Reeder, S. Schon, T. R. Ray, S. L. Chen, S. Mehta, S. Ruiz, J. A. Rogers, *Adv. Mater.,* 2019, 31, 1902109.

40   M. J. Patterson, S. D. R. Galloway, M. A. Nimmo, *Exp. Physiol.,* 2000, 85, 869.

41   S. J. Montain, S. N. Cheuvront, H. C. Lukaski, *Int. J. Sport Nutr. Exercise Metab.,* 2007, 17, 574.

42   Y. J. Lin, M. Bariya, H. Y. Y. Nyein, L. Kivimaki, S. Uusitalo, E. Jonsson, W. B. Ji, Z. Yuan, T. Happonen, C. Liedert, J. Hiltunen, Z. Y. Fan, A. Javey, *Adv. Funct. Mater.,* 2019, 29, 1902521.

43   N. A. Sitnikova, A. V. Borisova, M. A. Komkova, A. A. Karyakin, *Anal. Chem.,* 2011, 83, 2359.

44   N. A. Sitnikova, M. A. Komkova, I. V. Khomyakova, E. E. Karyakina, A. A. Karyakin, *Anal. Chem.,* 2014, 86, 4131.

45   B. J. Feldman, R. W. Murray, *Inorg. Chem.,* 1987, 26, 1702.

46   A. Malinauskas, R. Araminaite, G. Mickeviciute, R. Garjonyte, *Mater. Sci. Eng., C,* 2004, 24, 513.

47   H. M. Emrich, E. Stoll, B. Friolet, J. P. Colombo, R. Richterich, E. Rossi, *Pediatr. Res.,* 1968, 2, 464.

48   F. Herrmann, L. Mandol, *J. Invest. Dermatol.,* 1955, 24, 225.

49   H. Y. Y. Nyein, W. Gao, Z. Shahpar, S. Emaminejad, S. Challa, K. Chen, H. M. Fahad, L. C. Tai, H. Ota, R. W. Davis, A. Javey, *ACS Nano,* 2016, 10, 7216.

50   J. H. Zhu, Z. Q. Zhu, Z. S. Lai, R. Wang, X. M. Guo, X. Q. Wu, G. X. Zhang, Z. R. Zhang, Z. R. Zhang, Y. T. Wang, Z. Y. Chen, *Sensors,* 2002, 2, 127.

51   T. Unmussig, A. Weltin, S. Urban, P. Daubinger, G. A. Urban, J. Kieninger, *J. Electroanal. Chem.,* 2018, 816, 215.

52   M. Bariya, H. Y. Y. Nyein, A. Javey, *Nat. Electron.,* 2018, 1, 160.

53   S. S. Craig, S. A. S. Craig, M. S. Ganio, C. M. Maresh, H. Greg, K. A. da Costa, S. H. Zeisel, *J. Int. Soc. Sports Nutr.,* 2010, 7, 3.

54   A. J. Bandodkar, P. Gutruf, J. Choi, K. Lee, Y. Sekine, J. T. Reeder, W. J. Jeang, A. J. Aranyosi, S. P. Lee, J. B. Model, R. Ghaffari, C. J. Su, J. P. Leshock, T. Ray, A. Verrillo, K. Thomas, V. Krishnamurthi, S. Han, J. Kim, S. Krishnan, T. Hang, J. A. Rogers, *Sci. Adv.,* 2019, 5, eaav3294.

55   A. J. Bandodkar, W. Z. Jia, C. Yardimci, X. Wang, J. Ramirez, J. Wang, *Anal. Chem.,* 2015, 87, 394.

56   J. Xiao, Y. Liu, L. Su, D. Zhao, L. Zhao, X. Zhang, *Anal. Chem.,* 2019, DOI: 10.1021/acs.analchem.9b03110.

57   M. J. Buono, N. V. L. Lee, P. W. Miller, *J. Physiol. Sci.,* 2010, 60, 103.

58   B. Wang, X. M. Wen, P. Y. Chiou, N. T. Maidment, *Electroanalysis,* 2019, 31, 1641.

59   B. Wang, L. L. Feng, B. Koo, H. G. Monbouquette, *Electroanalysis,* 2019, 31, 1249.

Chapter 3. Anisotropic conductive film-based wearable freestanding electrochemical sensing film

3.1. Introduction

Leveraging the Internet-of-Things (IoT) infrastructure to transform personalized and precision medicine necessitates the large-scale deployment of health and wellness monitoring sensors in readily-proliferated wearable consumer electronics to harvest physiologically relevant data with minimal user intervention. [1, 2] To this end, physical sensors have been widely incorporated within commercialized wearable platforms to track the users' physical activities and vital signs. [3-7] However, to gain insight into the body's dynamic chemistry, electrochemical sensing interfaces are required to target the biomarker molecules present in non-invasively retrieved biofluids such as sweat. To this end, enzymatic, ion-selective, and electroactive electrochemical sensing interfaces were previously developed to target informative analytes such as metabolites and electrolytes. [8-13] Such sensing interfaces were embedded within sophisticated epidermal microfluidic configurations [11] and interfaced with wireless circuit boards to achieve system-level functionality. [14, 15] However, such implementations, for the most part, focused on optimizing the individual modules separately. Existing systems rely on in-plane interconnections and rigid connectors, fundamentally forcing them to route the transduced signal from the sensor to the readout electronics through highly strained (motion-induced) regions .[16-18] This limitation makes them severely susceptible to device operation failure (due to delamination, slipping, detachment, metal interconnect cracking, *etc*.) and external interference (*e.g*., mechanical noise), both of which lead to the loss of data fidelity.[19, 20] Body motion

restriction and/or external fixtures were required to stabilize and communicate the readings, making reported techniques impractical for the envisioned wearable applications.

To achieve high fidelity biomarker data acquisition, careful understanding and subsequently engineering the information delivery pathway from the skin to a readout unit is critical. Unlike the wearable physical sensors harvesting information from direct contact with the epidermis, the electrochemical sensors need to directly interact with the epidermally-retrieved biofluid to target biomarker data. This difference in the target information medium fundamentally necessitates a different design rationale and methodology. As shown in Fig. 3.1a (1A), for electrochemical sensing, the information delivery pathway consists of sampling and delivering the biomarker-rich biofluid to the sensor surface within a microfluidic structure, followed by signal transduction at the sensor surface and signal routing to the readout electronics via interconnecting elements (*e.g.*, metal traces and sensor-circuit connector). To preserve the fidelity of the biomarker information, the signal must be preserved along this pathway in the presence of motion-induced strain.

Here, by examining the biomarker information delivery pathway and recognizing near-zero strained regions within a microfluidic-based sensing module [21, 22], we engineer a strain-isolated pathway to preserve the biomarker data fidelity. Accordingly, a generalizable and disposable freestanding electrochemical sensing system (FESS) is devised, which simultaneously facilitates sensing and out-of-plane signal interconnection with the aid of double-sided adhesion. The FESS can be simultaneously adhered to skin and electronics with the aid of double-sided adhesion forces and without the need for rigid connectors. As a standalone unit, the FESS samples and directs epidermally-retrieved biofluids (*e.g.*, sweat) for electrochemical sensing. Then, it routes the transduced signal to the readout electronics through a strain-isolated pathway with the aid of out-of-plane interconnection.

On a broader scope, the FESS can serve as a foundation to realize an unprecedented system-level design strategy to address the challenges of wearable biosensing and integration with consumer electronics for daily use. To illustrate this point, the FESS was integrated within a custom-developed smartwatch to render a self-contained and skin-mountable wearable platform capable of sweat induction, sampling, electrochemical sensing, signal processing, and data display/transmission. The FESS-enabled smartwatch was specifically employed to monitor the sweat metabolite profiles of individuals engaged in various daily activities. The results indicate that the devised FESS-enabled platform renders high fidelity signal transduction as well as robust mechanical contact with human skin without constraining user motion. This freestanding sensing system can be integrated with the future wearable consumer electronics to generate high-fidelity longitudinal health- and wellness-related datasets throughout the users' daily activities.

3.2. Experimental Section

3.2.1. Fabrication Process of the FESS

The FESS, a thin film system, consists of multiple vertically stacked films: (1) a double-sided adhesive anisotropic conductive film (9703, 3M, 50 µm, ACF), (2) a noble metal electrode array patterned on ACF, (3) a bioanalytical film deposited on the electrodes as a sensing interface, (4) a thin-film microfluidic structure which houses biosensors, and (5) a double-sided skin adhesive film which facilitates the adherence of the FESS's microfluidic module to the skin. The fabrication process of the FESS is as follows:

First, an ACF was used as the substrate for electrode array patterning. One of the adhesive surfaces was covered with a pre-patterned mask for metal deposition. A 200 nm thick Au layer was thermally deposited onto the ACF to create an Au electrode array. For the Pt-based electrode

array, platinum nanoparticles (PtNP) were deposited onto the Au electrodes by chemical reduction in an aqueous solution of 2.5 mM H_2PtCl_6 and 1.5 mM formic acid (-0.1 V *vs.* Ag/AgCl, 10 min) to construct the PtNP-coated Au electrodes (Au/PtNP).[42] Cyclic voltammetry was used to examine their cathodic and anodic currents (under a three-electrode system) using a potentiostat (CHI660E, CH instrument, USA). The experiments were performed in fresh 0.1 M H_2SO_4 solution/0.1 M NaAc/0.1 M NaOH solution and the potential was scanned at a rate of 25 mV/s.

A poly-m-phenylenediamine (PPD) layer was electrochemically deposited onto the Au/PtNP electrodes by applying 0.85 V (*vs.* Ag/AgCl) for 300 s in a fresh PBS solution (Gibco® PBS, ThermoFisher, pH 7.2) with 5 mM m-phenylenediamine (Sigma-Aldrich). Then, the Au/PtNP/PPD electrodes were washed with deionized (DI) water and air-dried. Next, the electrode array was transferred to a low adhesion release paper liner (72#, 3M) by using PVA water-soluble tape (5414, 3M) and rinsed in DI water to remove residual particles. A 1% chitosan solution (Sigma-Aldrich) was prepared by dissolving chitosan in a 2% acetic acid (Sigma-Aldrich) solution by heating it up to 60 °C for 30 min until chitosan was fully dissolved. To develop the glucose sensor, the aforementioned 1% chitosan solution was mixed thoroughly with a glucose oxidase solution (Sigma-Aldrich, 50 mg/mL in PBS, pH 7.2) at a ratio of 1:1 (volume/volume). By drop casting 1 μL of the mixture onto the Au/PtNP/PPD electrode (12 mm^2), the glucose sensing interface was realized. To create the choline sensor, a 0.5 μL choline oxidase solution (Sigma-Aldrich, 0.5 unit/μL in DI water, pH 7.2) was placed onto the Au/Pt/PPD electrode (12 mm^2), dried at room temperature, and was followed by drop casting a 0.5 μL 1% chitosan solution. To create the lactate sensor, a 4 μL Lactate oxidase solution (Toyobo, 50 mg/mL in PBS) was deposited onto Au/PtNP/PPD electrode (12 mm^2) and dried at room temperature, followed by drop casting of a 2 μL 1% Chitosan solution and a 2 μL 3% polyvinyl chloride (PVC, Sigma-

Aldrich) solution.[43] The sensors were allowed to dry overnight at 4 °C, while being protected from light. They were stored at 4 °C when not in use. For pH sensor, iridium oxide (IrOx) was electrodeposited following previously reported protocols.[44, 45] For all biosensors, the reference electrode was fabricated by depositing Ag/AgCl ink (Ercon) on the electrodes and heating the modified electrodes at 80 °C for 10 min. The Au/PtNP electrode was used as the counter electrode.

Microfluidic channels were created by laser-cutting (Epilog Mini 24, Epilog Laser) 2D patterns on the double-sided tape (~170 µm). Outlets were created by using laser-patterned holes on PET (MG Chemicals, ~100 µm). The microfluidic structure/module was then assembled by attaching the patterned PET layer to the patterned double-sided tape with proper alignment. The microfluidic structure served as the strain-isolated housing for all biosensors (constructed on ACF).

3.2.2. Finite element analysis (FEA) and mechanical modeling of the FESS

FEA software, COMSOL 5.2, was used to simulate the mechanical behavior of the FESS under the directional shear load expected during usage. A 3D model of the FESS, mounted on the readout electronics, was used for the mechanical analysis with no delamination between layers being considered. In-plane directional shear force was applied on the skin adhesive layer with the base of electronics fixed. Similarly, the strain profile of the conventional in-plane interconnection subjected to a directional shear load and a bi-directional stretch load was analyzed using a 2D demo structure. For directional shearing, 10% displacement along the skin surface was applied on the µ-fluidics structure interfacing the skin and the displacement of the readout electronics was set to zero. For bi-directional stretching, displacements corresponding to 10% skin stretching were applied on both the readout electronics and the µ-fluidics interfacing the skin. The strain

36

distributions and magnitudes were captured for each simulation. The Young's modulus and Poisson's ratio used in the simulations were: 450 MPa and 0.49 for the ACF, skin adhesive and μ-fluidics structure; 2.5 GPa and 0.4 for PET; 24 GPa and 0.12 for the rigid electronics (FR-4); 2.5 GPa and 0.4 for flexible electronics (PI); 500 kPa and 0.49 for stretchable electronics (PDMS).

3.2.3. Contact resistance measurement of the FESS

The electrical resistance between the ENIG (electroless nickel/Immersion gold) contact pads (6 × 6 array, on a FPCB) and their corresponding pins were measured and recorded by a multimeter (Fluke-299), as initial resistances. Then, an ACF layer patterned with corresponding 6 × 6 Au electrode array was transferred onto the ENIG contact pads with proper alignment. The ACF-FPCB was mounted onto the curved surface of 3D-printed holder. The resistance for each pixel of the Au array on ACF was measured again by the same multimeter. Each resistance value was determined by averaging measured resistances from three different positions of the electrode surface.

3.2.4. Peel adhesion test of the FESS

The peel adhesion force (interfacial toughness) between the FESS and the PCB was determined by performing standard 180°-peeling tests, based on ASTM D3330, with a mechanical testing machine (Instron 5943). At first, the ACF, microfluidic-channel-patterned double-sided tape, and PET were laser-cut and assembled into 30 mm wide and 300 mm long strips. The patterned double-sided tape and PET served as the microfluidic structure, which can be considered as the backing material for the ACF. During the test, the ACF side of the laminated FESS strip was thumb-pressed onto the PCB to ensure a uniform and tight bond. The samples were prepared

in less than 1 day prior to the mechanical tests. The peeling tests were performed with the standard 180°-peeling method at a speed of 5 mm/s in ambient air at room temperature. The force *vs.* displacement profile was directly output by the Instron, and the peeling adhesion force/interfacial toughness was calculated by dividing the measured peeling force by the sample width.

3.2.5. Biosensor characterization and analytes measurement

To characterize the developed enzymatic sensing interfaces, constant potential amperometric measurements were conducted in PBS buffer (pH = 7.2) at + 0.5 V *vs.* Ag/AgCl. The amperometric response was continuously recorded by a potentiostat under constant stirring. By stepwise addition of different concentrations of the target analytes (*e.g*., glucose, lactate, and choline) in the PBS buffer for different sensors, a series of calibration plots were obtained. The limit of detection (LOD) for each amperometric sensing interface was calculated as LOD = 3*SD/(slope of calibration curve), where SD is the standard deviation of the baseline noise in blank solution. To characterize the IrOx pH sensor, open circuit potential (OCP) was measured against a separate Ag/AgCl reference. The PBS was titrated with NaOH/HCl to vary the pH from 4.1 to 10.15 and each stabilized OCP was recorded. The sensor selectivity tests were performed by the stepwise addition of different interferents into PBS, including glucose/lactate, creatine, KCl, NaCl, UA, AA, Pilocarpine, Aspirin, Metformin, and Albumin. At the end of the selectivity test, the target analytes were also added into the solutions.

3.2.6. Anti-corrosion capability of the FESS-PCB

Two PCBs with ENIG-based electrodes (18 mm^2) and a Pt disk electrode (1.6 mm in diameter) were cleaned with DI water and IPA solution, then dried in air at room temperature. The

ACF with Au/PtNP was transferred and aligned with the electrodes on one PCB and the other PCB was left unmodified as a control. The unmodified PCB, PCB with Au/PtNP patterned ACF, and Pt disk electrode were immersed into a PBS solution followed by OCP and corrosion current measurements. For OCP measurement, the voltage was recorded using a potentiostat. For corrosion current measurement, + 0.5 V (*vs.* Ag/AgCl) was applied under constant stirring.

3.2.7. Ex-situ signal fidelity characterization of the FESS-PCB

The FESS-PCB system and an accelerometer (mobile phone) were fixed onto a vortex mixer (Fisher Scientific). The blank PBS and PBS containing 100 μM glucose were sequentially injected into the FESS with a controlled flow rate (5 μL/min). The electrochemical signal was then recorded by a potentiostat during stationary and motion-induced (via vortex mixer, frequency = 5 Hz) conditions.

3.2.8. On-body test using the FESS-integrated smartwatch

The FESS was transferred onto the contact pads located on the backside of the custom-developed smartwatch. Then, the FESS-coupled smartwatch was adhered onto a healthy human subject's wrist. A smartwatch case was designed and 3D-printed to consolidate the smartwatch components (including LCD display, PCB module, and battery). In addition to the smartwatch, a mobile phone (equipped with an accelerometer) was mounted onto the subject's forearm to record the acceleration of his forearm during the exercise. To induce sweat iontophoretically, the target stimulation area of the skin was first cleaned with DI water and ethanol, followed by 5 minutes of iontophoretic sweat gland stimulation (with pilocarpine-loaded hydrogels, Pilogel).

3.2.9. Wireless PCB module

The wireless PCB module implements the required sweat stimulation circuitries to drive the iontophoresis electrode, as well as signal conditioning and processing circuitries to reliably measure the transduced sensing signals. The electrical connections from the iontophoresis/sensing layers with the main board were established by the metal vias, embedded within each layer. At its core, the PCB utilized an ultra-low-power microcontroller unit (STM8L – UFQFN20, STMicroelectronics), which was programmed to facilitate system level functionalities. These functionalities include setting the current levels for iontophoresis (accompanied with a current limiting protection circuitry) and providing I2C-controlled signals for the sensing and serial data communication modules. The microcontroller is interfaced with an onboard Bluetooth transceiver to wirelessly and bilaterally communicate the command and sensor output data with a custom-developed smartphone application. Moreover, the microcontroller communicates with an onboard LCD screen (st7735 – TFT-LCD, Sitronix Technology Corporation) to display the biomarker readouts, iontophoresis current level, and the local time.

An analog signal acquisition and conditioning circuitry was developed to interface the amperometric sensors and process the transduced signals. Accordingly, after the sensing mode is activated, an LMP91000 potentiostat chip (Texas Instruments) was enabled. This chip was programmed to maintain +0.5 V across the working and reference electrodes, and to convert the transduced sensor current to voltage values by leveraging its internal transimpedance amplifier stage. The output of the potentiostat was connected to a fifth-order low-pass filter (LPF), which was realized by a MAX7422 chip (Maxim Integrated), with a cut-off frequency of 1 Hz. The LPF stage mitigates the high frequency interference and the user's motion artifacts. The microcontroller's built-in 12-bit Analog-to-Digital (ADC) unit was used to convert the LPF's

analog output to the digital domain. The measured amperometric sensor response by the PCB was validated against a potentiostat.

In our PCB development efforts, we selected integrated circuit chips that were designed for low-power/ultra-low-power applications to implement a power efficient system. To power the PCB, a single miniaturized rechargeable lithium-ion polymer battery with a nominal voltage of 3.7 V was used. The choice for the battery's capacity depends on the intended modes and duration of operations. Based on our characterization results, with no further power optimization, the envisioned simultaneous operations (*e.g.*, iontophoresis, sensing, and bilateral wireless communication) demanded peak supply current levels on the order of 100 mA. For an application such as periodic sweat sampling and analysis at 6 points during the day (*e.g.*, monitoring glucose levels before/after main meals), and assuming 15 minutes of active operation, a battery capacity on the order of 500 mAh would be sufficient.

3.2.10. Smartphone application and smartwatch design

To wirelessly communicate with the PCB module from the user standpoint, an Android-based smartphone application was developed. The application provides a graphical user interface to execute a range of functionalities, including setting the desired operational modes as well as data display and storage. In our implementation, the user input is read and relayed to the PCB through Bluetooth communication of predefined integer values (each value mapped to a desired operation). Then, the corresponding command is received and executed at the microcontroller level.

3.2.11. The custom smartphone application design/cloud server

The Android application is designed to establish communication with the paired/specified custom-developed smartwatch upon startup. Once the communication is established, the user has the option to program the desired iontophoresis current level for sweat stimulation. Additionally, the user can switch between the iontophoresis and sensing modes with the press of a button. In sensing mode, the real-time and filtered sensing results are recorded, timestamped, and plotted by the application. Finally, the sweat metabolite data captured by the application are automatically stored on a custom-developed Google Cloud platform.

3.2.12. Institutional Review Board (IRB) approval for human subject testing

The conducted human subject experiments were performed in compliance with the protocols approved by the IRB at the University of California, Los Angeles (IRB#17-000170). All subjects gave written informed consent before participation in the study.

3.3. Characterization and Integration of the Anisotropic Conductive Sensing Film

In our approach, we leverage a double-sided adhesive ACF (~50 µm-thick). One side of the adhesive film serves as the integration interface, where it can be directly adhered to PCB contact pads, realizing a µm-level vertical sensor-circuit signal interconnection. On the other side of the ACF, the biosensing interface can be constructed, by first patterning a noble metal layer, followed by modifying the recognition layers. The vertical conductivity of the ACF is rendered by metal particles (*e.g.*, silver) that are embedded in the polymer matrix of ACF, as seen from the scanning electron microscopy (SEM) image in Figure 3.2a (JMEMS). By leveraging the adhesive coating

42

of the ACF and without the need for a metal adhesion layer, a gold layer (Au) can be directly evaporated on the film's surface (200 nm-thick) as shown in Figure 3.2b(JMEMS), serving as a base for the subsequent chemical modification layers required to achieve biosensing. The adhesive coating on the other side of the ACF facilitates the adhesion of the ACF to contact pads, thereby forming the mechanically robust and electrically-conductive sensor-circuit interconnection.

Standard metal contact pads on a PCB galvanically corrode in an ionic biofluid solution during electrochemical sensing operation. This corrosion manifests as signal degradation and/or large background current (Figure 3.2c(JMEMS), corrosion current indicated in red). As shown in Figure. 3.2c, the PCB contacts (made from cost effective immersion gold) coupled with an ACF-based metal film (platinum/Au) presented near-zero corrosion current (blue line), indicating that the galvanic corrosion underneath the metal contact pads was effectively prevented. The amperometric characterization of the ACF/PCB-based electrode response to a series of oxidant solutions (here, H_2O_2) indicated the preservation of the catalytic capability of the electrode (Figure 3.2c, inset). The excellent anti-corrosion performance of the ACF sensing film can be attributed to: (1) the hydrophobicity of the adhesive coating on both sides of the film, and (2) the absence of oxidation prone-adhesion metal (*e.g*., chromium). Additionally, as shown in Figure. 3.2d, amperometric characterization using ACF films with different areas on a fixed PCB contact pad yielded a linear relationship between the corresponding electrochemical current responses (toward H_2O_2) and the ACF sensing area. This observation illustrates the high degree of freedom achieved by our approach for tuning the sensor's output current level, simply by customizing the area of the ACF sensing film and (without adjusting the circuitry or contact pads designs).

3.4. Design principles of the freestanding electrochemical sensing system

Careful examination of the strain distribution of a typical microfluidic module, under motion-induced stress, yields near-zero strain at the bottom of the microfluidic channel (channel-biofluid interface). The resultant strain profile can be attributed to the absorption and isolation of the strain by the load-bearing components of the microfluidic structure and biofluid, respectively. As shown in Figure 3.1b (1B), by recognizing and leveraging the fact that the strain-isolated region is the one that contains the sensor, we engineer a strain-isolated biomarker information delivery pathway that protects and routes the signal from the biofluid sensing interface all the way to the readout electronics.

To render an efficient pathway, we were inspired by integrin [23, 24], a cell adhesive molecule, which efficiently enables physiological information exchange between intracellular (*e.g*., cytoskeleton) and extracellular matrices. As a single entity, integrin utilizes double-sided adhesion forces (*e.g*., Van der Waals force) to facilitate sensing and out-of-plane signal interconnection (Figure 3.3a (S1)). Accordingly, a generalizable and disposable freestanding electrochemical sensing system (FESS) is devised, which implements integrin-like functionalities through a strain-isolated region within a microfluidic structure (Figure 3.3b (S1, B)).

The FESS is engineered as a vertically conductive, double-sided adhesive, and flexible microfluidic bioanalytical thin film system (Figure 3.4, 3.5 (S2, 3)). This thin film system consists of multiple vertically stacked films: an adhesive anisotropic conductive film (ACF), a noble metal electrode array film, a biochemical film, a microfluidic film (Figure 3.6a-e (S4, A to E), [25, 26]), and a skin adhesive film. The versatility of the FESS in terms of its core capabilities is demonstrated by depositing various patterns of different noble metals (gold Au and platinum Pt) as well as different sensing layers to target a panel of physiologically-relevant biomarker

molecules in sweat. The inherent vertical conductivity of the FESS based on ACF allows for the realization of out-of-plane interconnection (Figure 3.1c (1C)), which provides a degree of freedom for signal routing to avoid highly strained regions, thus preserving the transduced signal along the sensor-to-electronics signal pathway. The vertical conductivity and adhesive properties of the FESS, together, allow for direct interface with contact pads (Figure 3.6f (S4, F)) on the readout electronics, eliminating the need for rigid connectors. Additionally, by including a microfluidic film, the thin film and inherently flexible system can be adapted for leakage-free epidermal biofluid (*e.g.*, sweat) harvesting and routing (Figure 3.6g-k S4, (G to K) and Figure. 3.7). The FESS can be adhered to skin and electronics, by leveraging its double-sided adhesive property.

As a complete thin film system, it can be simply taped onto the readout electronics without the need for any connectors, and with minimal contact resistance, thus potentially transforming any electrical contact into a chemo-/biosensor. The versatility of the FESS design allows for its implementation in various array formats (*e.g.*, 1×2, 3×3, 6×6, as exemplified in Figure 3.1d(1D)) to satisfy the end-application requirements. A representative self-contained biomarker sensing smartwatch, realized with the aid of FESS, is shown in Figure 3.1e (1E), which can monitor the sweat metabolite profiles of individuals in sedentary (Figure 3.1f (1F)) and high intensity exercise settings (Figure 3.1g (1G)).

3.5. A strain-isolated signal pathway

In this section, we first demonstrate the underlying physical phenomenon governing the superior performance of the out-of-plane (achieved by FESS) *vs.* conventional in-plane signal interconnection. Then, we characterize the out-of-plane electrical interconnection and mechanical adhesion properties of the FESS.

Conventional wearable microfluidic electrochemical sensors rely on in-plane signal interconnection (Figure 3.8a (2A)) to relay the transduced signals to the readout circuitry. Therefore, based on the implemented signal pathways, the signal is inevitably routed through body motion-induced strain-concentrated regions (including the 2D-patterned interconnects and/or the connector, Figure 3.9a-c (S6, A to C)). Accordingly, they are severely susceptible to device operation failure (due to delamination, slipping, detachment, metal interconnect cracking, *etc*.) and interference (*e.g*., strain-induced noise), both of which lead to the loss of data fidelity.

In the implementation of the FESS, the inherent vertical conductivity of the ACF facilitates out-of-plane signal interconnection (Figure 3.8a (2A), similar to that shown in the reported advanced stretchable electronics [27]), which here, can be exploited as a degree of freedom for avoiding undesired body motion-induced strain effects on signal pathways. To illustrate this point, we simulated the strain profile experienced by a representative FESS (Figure 3.8b (2B)), under an applied force (representing the force exerted along the skin-device interface due to the body motion). Figure 3.8c (2C) visualizes the corresponding strain distribution of a sensing pixel within the FESS, demonstrating that the maximal strain occurs in the regions where the microfluidic structure contacts with the substrate, while minimal strain occurs at the biofluid-substrate interface (encompassing the sensor). When constructing the signal pathway, the high strain regions can be avoided by leveraging the out-of-plane interconnection property of the FESS. As shown in Figure 3.8d (2D), this unique property of FESS allows for significantly reducing (by 2 orders of magnitude) the strain experienced by the transduced signals. This strain isolation strategy rendered by FESS can be generally adopted for interfacing electronics with different mechanical properties. Figure 3.9d (S6 (D)) shows the simulated strain profiles for electronics with different substrate materials and Young's modulus (also detailed in table S1): stretchable PDMS (500 kPa), flexible

polyimide board (2.5 GPa), and rigid board (24 GPa). In particular, the results shown in Figure 3.9d (S6 (D)) indicate that the strain isolated regions are present in all scenarios (independent of the electronic substrate's stiffness). Additionally, the interconnection length rendered by FESS is ~50 µm (corresponding to the thickness of the ACF). This represents more than two orders of magnitude reduction in the transduced signal pathway, as compared to the conventional implementations with centimeter-scale interconnection routing, which is critical to the mitigation of external electromagnetic interference and mechanical noise.

We first establish the suitability of the ACF to simultaneously serve as an electrode supporting substrate and as an interconnection film. To pattern electrodes on ACF, the inherent adhesive property of the ACF was leveraged to directly deposit Au via e-beam metal evaporation. This approach eliminates the need for the metal adhesion layer (*e.g*., chromium or titanium), and subsequently allows for realizing a corrosion-resistant and stable interface for operation in biofluid environment.[28]

To demonstrate the robustness of the out-of-plane signal interconnection against mechanical deformation, the FESS-based interconnection resistance distribution (R_{FESS}) of a representative 6 x 6 grid of Au ACF-based electrodes was characterized under spatially varying strain distribution profiles. Accordingly, the grid of electrodes was mated with a corresponding grid of flexible PCB-based contact pads (with resultant resistance distribution $R_{FESS} + R_{FPCB}$) via adhesion. Then, the resultant configuration was mounted on holders with localized tip radius curvature ($\alpha = 60°$, $R = 15$ mm and $\alpha = 30°$, $R = 10$ mm), such that the column 4 of the mated gird configuration experiences the maximal strain, while other columns experience minimal strain (conceptualized in Figure 3.8e (2E)). By comparison of the R_{FESS} measurements of the 4th column with those of other columns, we can evaluate the effect of the stress concentration on the out-of-plane interconnection

47

resistance across the device. Our characterization results, shown in Figure 3.8f (2F), demonstrate that despite the high strain experienced by the 4th column (compared to the others), the corresponding out-of-plane interconnection resistances were minimally impacted across the device (for all three tested conditions, *i.e.*, flat, bent at 30°, and bent at 60°). The observed variations are on the order of 5%, which can be attributed to the error associated with the manual probing of the resistance values. The interconnection resistance (per unit area) levels for all cases are less than 0.025 Ω/mm^2, rendering less than 0.1 Ω of resistance, which is a fraction of the resistance contributed by the FPCB (Figure 3.8g (2G)). This substantially low interconnection resistance can be attributed to the devised implementation of the interconnect, which realizes an effective cross-section resistor surface area A comparable to the size of the sensor (~ 1 mm $\times$ 1 mm as compared to conventional interconnects' cross section ~ 100 nm x 1 mm) and resistor length l of 50 µm (as compared to conventional interconnect lengths ~ 1 cm), representing orders of magnitude of reduction in resistance R, where R $\propto$ (l/A). Additional characterization results demonstrate minimal changes to the FESS-based interconnection (ACF) resistance, for different bending angles (Figure 3.10a (S7, A)), upon performing cyclical bending and twisting (over 1000 cycles, respectively shown in Figure 3.10b and c (S7, B and C)), and throughout different daily activities (Figure 3.10d (S7, D)).

To characterize the mechanical adhesion property of the FESS, 180° peel adhesion tests were performed (as described in detail in the Methods section), because interfacial peeling properties are critical to the maintenance of robust interconnection between the FESS and electronics (*e.g.*, PCB). Specifically, the adhesion force between the FESS and electronics should be higher than that between the FESS and dry/actively sweat secreting skin (Figure 3.11 (S8), ~ 0.3 N/cm, in agreement with previously reported skin-adhesive medical tapes characterization results [29, 30]).

Because the ACF layer in our devised thin film system bridges the FESS structure with electronics, we characterize the force required to peel the ACF layer of the FESS from a PCB. Given the influence of the backing structure (consisting of the microfluidic base and channel) on the peeling profile of the ACF, first, two test device structures were considered and characterized: one with double-sided tape backing (representing the microfluidic base) and one without (representing the microfluidic channel). The peeling forces corresponding to devices with/without backing were characterized as 10.3 N/cm and 2.7 N/cm, respectively (> 0.3 N/cm, Figure 3.8h and i (2, H and I)). Following the same protocol, a representative FESS (as a complete device structure) containing periodic microfluidic features was also characterized. As shown in Figure 3.8j (2J), the measured peeling force profile illustrates a periodic pattern, tracing the interfacial features with and without the microfluidic structure backing, where the maximal and minimal peeling force levels correspond to the peeling forces of the two tested structures in Figure 3.8h and i (2H and Fig. 2I), respectively. For all characterized test device structures, the peeling forces were larger than 0.3 N/cm, indicating strong level of the FESS-based interconnection's adhesion to electronics, and validating its suitability for on-body applications.

3.6. Electrochemical signal transduction

In this section, we characterized the signal transduction capability of the FESS. Specifically, to achieve bio/chemical-to-electrical signal transduction, noble metal electrodes were patterned onto the ACF (forming the sensor substrate), followed by the deposition of designated bio/chemical films to target analytes of interest. We first characterized the electrochemical activity of the metal-patterned ACF for two commonly used electrode surfaces: unmodified Au and Pt

nanoparticles (PtNP)-modified Au (which presents enhanced electrocatalytic performance in comparison to unmodified-Au [31]).

Next, cyclic voltammetry was used to test the electrochemical activity of the unmodified-Au and Au/PtNP patterned ACF in 0.1 M H_2SO_4 (Figure 3.12a, b (3A, B)), in 0.1 M NaAc (pH = 7.2 – 7.8, Figure 3.13a and b (S9, A, B)), and in 0.1 M NaOH (pH = 13.0, Figure 3.13a and b (S9, A, B)) solutions [32]. In Figure 3.12a (3A), hydrogen evolution reaction (HER) can be observed in the cathodic region, where the Au electrode inert potential window extends to ~ -0.1 V (*vs.* Ag/AgCl). In the anodic region, the adsorption of anions (*i.e.* OH^-, SO_4^{2-}) and of the initial gold surface oxidation occurs prior to oxygen evolution reaction (OER). The reduction peaks in this region are observed on reverse sweep, which arise from the gold oxide surface reduction and the desorption of ions. The same procedure was performed to characterize the PtNP-modified surface. As shown in Figure 3.12b (3B), the electrochemical characteristic of the PtNP-modified surface presents distinct signature peaks, which are related to hydrogen absorption/desorption of a Pt-based surface, indicating successful and stable PtNP modification of the electrode surface. Given the enhanced electrocatalytic activity of the PtNP-modified electrode in comparison to the unmodified Au electrode (Figure 3.13 c, d (S9, C and D)), the subsequent electrochemical biosensor development efforts were performed on the PtNP-modified electrode. This property can be exploited to detect electroactive species such as hydrogen peroxide (H_2O_2, sensitivity: 296.2 ± 20.0 μA/mM/cm^2 and limit of detection, LOD: 0.2 ± 0.06 μM, Figure 3.12c (3C)), ascorbic acid, and dopamine with high sensitivity (Figure 3.13e and f (S9, E and F)). In particular, the highly sensitive detection of H_2O_2 (the end-product of numerous enzymatic reactions) can be leveraged for targeting informative biomarkers (*e.g*., glucose and lactate).The PtNP-modified electrode surface can be functionalized via the deposition of bio/chemical films to equip the FESS with

chemo-/biosensing capability. Accordingly, the recognition elements of the film as well as the electrochemical interrogation method can be tailored to specifically target the biomarker molecules of interest. For example, Figure 3.12 d-f (3D-F) show that enzymatic-based sensors can be combined with chronoamperometry to target glucose, lactate, and choline. Additionally, iridium oxide-functionalized electrodes can be combined with open-circuit potential measurements to measure pH (Figure 3.13g (S9, G)). These electroanalytical methods provide sample-to-answer biomarker readouts and are capable of rendering real-time insight into the alterations in the sweat bio-composition.

Here, we specifically adapted the sensing capability of the FESS to target glucose, lactate, and choline (all of which are present in non-invasive biofluids such as sweat [33, 34], as they are informative biomarkers of body metabolism and nutrition [35, 36]). The sensing interface for each target consists of an enzyme layer, coupled onto a poly-m-phenylenediamine (PPD)-layer, where the PPD layer serves as a permselective membrane to reject interfering species.[37, 38] The response of each sensor toward the target analyte was first characterized individually. Figure 3.12d-f (3D-F) show the respective current responses of the glucose (sensitivity: 22.8 ± 0.7 $\mu A/mM/cm^2$ and LOD: 1.7 ± 0.7 μM), lactate (sensitivity: 4.1 ± 0.3 $\mu A/mM/cm^2$ and LOD: 4.6 ± 3.0 μM), and choline sensors (sensitivity: 9.4 ± 3.9 $\mu A/mM/cm^2$ and LOD: 10.5 ± 3.7 μM), measured amperometrically within their corresponding physiological relevant range (glucose: 0–1000 μM, lactate: 0–20 mM, choline: 0-350 μM, performed in phosphate-buffered saline, PBS). For all three sensors, the generated responses are proportional to the corresponding analyte's concentration levels. To ensure reliable operation in complex biofluids (here, sweat), the selectivity performances of the glucose and lactate sensors were characterized by measuring their responses towards a diverse panel of interfering species. As listed in Figure 3.12g (3G), the

51

selected classes of interfering species include: electrolytes, electroactive species, drugs, sweat agonists, proteins, and other small molecules. As shown in Figure 3.12h, i (3H, I), both the glucose and lactate sensors exhibited negligible steady-state responses to the interfering species, while incremental addition of the target analytes' concentration levels caused significant stepwise current responses. The sensing reliability of the FESS was further validated by performing a blind study, where a series of sample solutions were analyzed in random sequence by the FESS (taped onto contact pads) and a gold standard lab biochemistry analyzer (YSI 2900D). As shown in Figure 3.14a and b (S10 A and B), the biomarker levels measured by the corresponding sensors were very close to those measured by the lab instrument ($R^2_{Gluocse}$: 0.99 and $R^2_{Lactate}$: 0.95).

Furthermore, to demonstrate the multiplexed sensing capability of the FESS, the developed sensing interfaces were fabricated onto a single ACF, and the resultant functionalized film was taped onto a grid of PCB contact pads. The constructed sensor array's response was continuously monitored, while introducing different analytes at different timepoints. As shown in Figure 3.12j (3J), the sequential addition of 1 mM lactate, 100 μM choline, and 100 μM glucose correspondingly resulted in clear and stable stepwise response of the respective sensors. No crosstalk and corrosion-induced noise were observed during the multiplexed measurements. Moreover, amperometry (Figure 3.15a to c (S11, A to C)) and open circuit potential (Figure 3.15d and e (S11, D and E)) characterization experiments validated the electrochemical corrosion resistance of the FESS-PCB in saline solution environments, which is critical to ensure stable and extended sensing operation in biofluids and for the envisioned applications. Additional amperometry measurements performed under thermal cycling (25, 35 and 45°C) over an extended time period (> 1 hr) further demonstrated the operational stability of the FESS-PCB system (Figure 3.15f (S11, F)). The FESS anti-corrosion lifetime is estimated to be at least 110 hrs at room

temperature (as predicted by the performed accelerated life testing, Figure 3.15g (S11, G), and based on the Arrhenius model [39]).

3.7. FESS-enabled smartwatch for sweat biomarker monitoring during daily activities

To demonstrate the utility of the FESS for biomarker monitoring during the user's daily activities, the FESS was integrated with a custom-developed smartwatch as a model IoT device (Figure 3.16a (4A)). The smartwatch hardware consists of analog/digital circuitries, a Bluetooth transceiver, and an LCD screen to implement system-level functionalities such as signal and user command processing, display, and wireless data communication (Figure 3.17a to c (S12, A to C)). Depending on the user's needs, disposable FESS units with different sensing capabilities can be selected and taped onto the smartwatch by leveraging the reversibility of the adhesion forces of the FESS (Figure 3.17d to h (S12, D to H)). The FESS-integrated smartwatch shows similar performance compared with those obtained by the potentiostat (Figure 3.17i (S12, I)). An optional iontophoresis hardware module (a programmable current source), coupled with a ring-shaped pilocarpine-loaded hydrogel interface, is also implemented as a plugin unit for on-demand sweat induction in sedentary subjects (see more details in Method and Figure 3.17 j and k (S12 J and K)). The FESS-coupled and lithium polymer-powered hardware is embedded within a form-fitting 3D-printed casing. The complete smartwatch can be adhered onto the skin, without the need for any external wrapping or fixtures, to perform wireless biomarker sensing as a self-contained unit, and the obtained sensing data is linearly correlated with those obtained by a standard potentiostat. While the LCD screen displays the real-time readings and the temporal profile of the biomarker measurements, the Bluetooth transceiver module relays the readings to a custom-developed mobile application, which in turn uploads the data to a cloud-based server for further analysis.

To evaluate the signal stability of the FESS-enabled smartwatch against motion artifacts, a series of *ex-situ* and on-body experiments were performed to characterize the sensor response in the presence of varying motion characteristics in terms of frequency, orientation, acceleration, and externally applied contact force. For the *ex-situ* experiments, a FESS-based glucose-sensor response was continuously recorded upon introduction of a blank and 100 μM glucose solutions (injected at 5 μL/min to mimic sweat secretion, into a microchannel with the height of 170 μm, containing a 2 mm × 3 mm glucose sensor), under stationary and three-dimensional oscillatory acceleration conditions (~10 m/s^2 at 5 Hz, generated by a vortical mixer). As shown in Figure 3.16b and c (4B and 4C), the measured sensor responses exhibit negligible fluctuations ($< 6\%$) despite the induced motion, indicating the high fidelity of data achieved by the FESS-based system (similarly, as shown in Figure 3.18 (S 13), stable responses were recorded for the microfluidic sensing modules with different channel heights and sensor dimensions, as well as the insufficient fluidic filling situation). Furthermore, for on-body characterization, a FESS-based lactate-sensor was integrated with the smartwatch worn by the subject, then the sensor's response to exercise-induced sweat was continuously recorded under various body motions, including punching, arm swinging, and forearm twisting, with varying acceleration, frequency, and orientation. Additionally, to quantify the effect of varying externally applied contact forces, different weights (1-2 N, similar force levels to that applied during finger tapping [40]) were applied to the smartwatch during the on-body lactate sensor response recordings. As shown in Figure 3.16d-g (4D-G), the measured sensor responses across all conditions exhibit negligible fluctuations ($< 8\%$), indicating the suitability of the FESS-based smartwatch to render high fidelity biomarker data recording in presence of unconstrained body motion.

To demonstrate the utility of the wearable system for the envisioned diurnal and longitudinal biomarker monitoring, the FESS-enabled smartwatch was adhered on a subject's forearm, which was wirelessly controlled by the subject to take real-time sweat-based biomarker measurements at set time intervals in relation to the user's daily routine. The smartwatch was used by the subject to monitor his iontophoretically-induced sweat glucose levels before/after the consumption of mixed meals (*e.g.*, at the user's routine lunch and dinner times). As illustrated in Figure. 3.16 h, I (4H, I), the smartwatch glucose sensor readouts indicate the elevation of the subject's sweat glucose level upon food intake, which is in line with previously reported trends.[41] Additionally, the smartwatch was used by the subject to monitor the sweat lactate profile (Figure 3.16j (4J)) during running in a field. The smartwatch readouts indicated stable sweat lactate readings, despite the presence of relatively high frequency and high acceleration body motions involved in the running session.

3.8. Conclusion

Here, by examining the biomarker information delivery pathway and recognizing near-zero strained regions within a microfluidic-based sensing module, we engineered a strain-isolated pathway to preserve the biomarker data fidelity. To render an efficient implementation, inspired by integrin (a cell adhesive molecule), which facilitates physiological information exchange between biological interfaces via sensing, out-of-plane signal interconnection, and double-sided adhesion forces, a generalizable and disposable electrochemical thin film sensing system is devised. The thin film system renders integrin-like functionalities in terms of signal transduction and co-axial signal interconnection/double-sided adhesion forces, all within a freestanding entity (namely, FESS). The FESS can reliably bridge the skin and the readout electronics to harvest

biomarker information. The FESS also serves as a foundation to realize an unprecedented system-level design strategy to simultaneously address the challenges of wearable biosensing and integration with consumer electronics for daily use. To illustrate this objective, the FESS is seamlessly coupled with a custom-developed smartwatch. The robustness of the FESS-enabled smartwatch was validated by monitoring the real-time biomarker readouts throughout the user's daily routine activities. The versatility of the FESS can be exploited to target a wide panel of biomarkers. The design methodology can be equivalently adopted to construct physical sensing interfaces in order to characterize the informative metrics related to the sweat secretion profile (*e.g.*, the onset of sweating, secretion rate, and sweat loss volume).

Ultimately, to commercialize and adapt the presented wearable technology for population-level health and wellness monitoring, future clinical trials are required to map the sweat-based biomarker readings to the physiological status of the users, while accounting for the biological factors such as inter/intra individual and anatomical variations. In that regard, the advantages of our technology in terms of its ease of integration with wearable consumer electronics and its ability to generate of high-fidelity biomarker readings can be particularly harnessed to perform large-scale and longitudinal clinical investigations. The large data sets rendered by such studies enables the physiological-meaningful interpretation of the biomarker readings and the establishment of the objective criteria necessary to provide actionable feedback to the users.

3.9. Reference

1   R. Byrne, D. Diamond. *Nat. Mater.* 2006, 5, 421-424.

2   B. Farahani, F. Firouzi, V. Chang, M. Badaroglu, N. Constant, K. Mankodiya. *Future Gener. Comp. Sy.,* 2018, 78, 659-676.

3   H. U. Chung, B. H. Kim, J. Y. Lee, J. Lee, Z. Q. Xie, E. M. Ibler, K. Lee, A. Banks, J. Y. Jeong, J. Kim, C. Ogle, D. Grande, Y. Yu, H. Jang, P. Assem, D. Ryu, J. W. Kwak, M. Namkoong, J. B. Park, Y. Lee, D. H. Kim, A. Ryu, J. Jeong, K. You, B. W. Ji, Z. J. Liu, Q. Z. Huo, X. Feng, Y. J. Deng, Y. S. Xu, K. I. Jang, Y. H. Zhang, R. Ghaffari, C. M. Rand, M. Schau, A. Hamvas, D. E. Weese-Mayer, Y. G. Huang, S. M. Lee, C. H. Lee, N. R. Shanbhag, A. S. Paller, S. Xu, J. A. Rogers, *Science,* 2019, 363, eaau0780.

4   Y. Khan, M. Garg, Q. Gui, M. Schadt, A. Gaikwad, D. G. Han, N. A. D. Yamamoto, P. Hart, R. Welte, W. Wilson, S. Czarnecki, M. Poliks, Z. P. Jin, K. Ghose, F. Egitto, J. Turner, A. C. Arias, *Adv. Funct. Mater.,* 2016, 26, 8764-8775.

5   C. H. Wang, X. S. Li, H. J. Hu, L. Zhang, Z. L. Huang, M. Y. Lin, Z. R. Zhang, Z. N. Yin, B. Huang, H. Gong, S. Bhaskaran, Y. Gu, M. Makihata, Y. X. Guo, Y. S. Lei, Y. M. Chen, C. F. Wang, Y. Li, T. J. Zhang, Z. Y. Chen, A. P. Pisano, L. F. Zhang, Q. F. Zhou, S. Xu, *Nat. Biomed. Eng.,* 2018, 2, 687-695.

6   C. M. Boutry, Y. Kaizawa, B. C. Schroeder, A. Chortos, A. Legrand, Z. Wang, J. Chang, P. Fox, Z. N. Bao, *Nat. Electron.,* 2018, 1, 314-321.

7   C. Wang, D. Hwang, Z. B. Yu, K. Takei, J. Park, T. Chen, B. W. Ma, A. Javey, *Nat. Mater.,* 2013, 12, 899-904.

8   S. Emaminejad, W. Gao, E. Wu, Z. A. Davies, H. Y. Y. Nyein, S. Challa, S. P. Ryan, H. M. Fahad, K. Chen, Z. Shahpar, S. Talebi, C. Milla, A. Javey, R. W. Davis, *Proc. Natl. Acad. Sci. USA,* 2017, 114, 4625-4630.

9   A. Hauke, P. Simmers, Y. R. Ojha, B. D. Cameron, R. Ballweg, T. Zhang, N. Twine, M. Brothers, E. Gomez, J. Heikenfeld, *Lab Chip,* 2018, 18, 3750-3759.

10   W. Gao, S. Emaminejad, H. Y. Y. Nyein, S. Challa, K. V. Chen, A. Peck, H. M. Fahad, H. Ota, H. Shiraki, D. Kiriya, D. H. Lien, G. A. Brooks, R. W. Davis, A. Javey, *Nature,* 2016, 529, 509-514.

11   A. Koh, D. Kang, Y. Xue, S. Lee, R. M. Pielak, J. Kim, T. Hwang, S. Min, A. Banks, P. Bastien, M. C. Manco, L. Wang, K. R. Ammann, K. I. Jang, P. Won, S. Han, R. Ghaffari, U. Paik, M. J. Slepian, G. Balooch, Y. G. Huang, J. A. Rogers, *Sci. Transl. Med.,* 2016, 8, 366ra165.

12   S. Imani, A. J. Bandodkar, A. M. V. Mohan, R. Kumar, S. F. Yu, J. Wang, P. P. Mercier, *Nat. Commun., 2016,* 7, 11650.

13   H. Lee, C. Song, Y. S. Hong, M. S. Kim, H. R. Cho, T. Kang, K. Shin, S. H. Choi, T. Hyeon, D. H. Kim, *Sci. Adv., 2017,* 3, e1601314.

14   Y. J. Hong, H. Lee, J. Kim, M. Lee, H. J. Choi, T. Hyeon, D. H. Kim, *Adv. Funct. Mater.,* 2018, 28, 1805754.

15   H. Y. Y. Nyein, L. C. Tai, Q. P. Ngo, M. H. Chao, G. B. Zhang, W. Gao, M. Bariya, J. Bullock, H. Kim, H. M. Fahad, A. Javey, *ACS Sens., 2018,* 3, 944-952.

16   Y. H. Zhang, S. D. Wang, X. T. Li, J. A. Fan, S. Xu, Y. M. Song, K. J. Choi, W. H. Yeo, W. Lee, S. N. Nazaar, B. W. Lu, L. Yin, K. C. Hwang, J. A. Rogers, Y. G. Huang, *Adv. Funct. Mater., 2014,* 24, 2028-2037.

17   K. D. Harris, A. L. Elias, H. J. Chung, *J. Mater. Sci., 2016,* 51, 2771-2805.

18   M. Bariya, H. Y. Y. Nyein, A. Javey, *Nat. Electron., 2018,* 1, 160-171.

19   M. Gonzalez, F. Axisa, M. V. BuIcke, D. Brosteaux, B. Vandevelde, J. Vanfleteren, *Microelectron. Reliab., 2008,* 48, 825-832.

20   J. Cai, K. Cizek, B. Long, K. McAferty, C. G. Campbell, D. R. Allee, B. D. Vogt, J. La Belle, J. Wang, *Sensor Actuat. B-chem, 2009,* 137, 379-385.

21   A. Romeo, Q. H. Liu, Z. G. Suo, S. P. Lacour, *Appl. Phys. Lett., 2013,* 102.

22   Y. J. Ma, M. Pharr, L. Wang, J. Kim, Y. H. Liu, Y. G. Xue, R. Ning, X. F. Wang, H. U. Chung, X. Feng, J. A. Rogers, Y. Huang, *Small,* 2017, 13, 1602954.

23   M. J. Dalby, N. Gadegaard, R. O. C. Oreffo., *Nat. Mater.*, 2014*,* 13, 558-569.

24   C. K. Miranti, J. S. Brugge, *Nat. Cell Biol.,* 2002, 4, E83-E90.

25   H. S. Lin, Y. C. Zhao, S. Y. Lin, B. Wang, C. Yeung, X. B. Cheng, Z. Q. Wang, T. Y. Cai, W. Z. Yu, K. King, J. W. Tan, K. Salahi, H. Hojaiji, S. Emaminejad, *Lab Chip,* 2019, 19, 2844-2853.

26   H. S. Lin, H. Hojaiji, S. Y. Lin, C. Yeung, Y. C. Zhao, B. Wang, M. Malige, Y. B. Wang, K. King, W. Z. Yu, J. W. Tan, Z. Q. Wang, X. B. Cheng, S. Emaminejad, *Lab Chip*, 2019, 19, 2966-2972.

27   Z. L. Huang, Y. F. Hao, Y. Li, H. J. Hu, C. H. Wang, A. Nomoto, T. S. Pan, Y. Gu, Y. M. Chen, T. J. Zhang, W. X. Li, Y. S. Lei, N. Kim, C. F. Wang, L. Zhang, J. W. Ward, A. Maralani, X. S. Li, M. F. Durstock, A. Pisano, Y. Lin, S. Xu, *Nat. Electron.,* 2018, 1, 473-480.

28   L. L. Qiang, S. Vaddiraju, J. F. Rusling, F. Papadimitrakopoulos. Highly sensitive and reusable Pt-black microfluidic electrodes for long-term electrochemical sensing. *Biosens. Bioelectron.,* 2010*,* 26, 682-688.

29   J. Kim, Y. Hwang, S. Jeong, S. Y. Lee, Y. Choi, S. Jung, *J. Mater. Chem. C,* 2018, 6, 2210-2215.

30   L. Liu, K. Kuffel, D. K. Scott, G. Constantinescu, H. J. Chung, J. Rieger, *Biomed. Phys. Eng. Express,* 2018, 4, 015004.

31   X. Li, D. Heryadi, A. A. Gewirth, *Langmuir*, 2005, 21, 9251-9259.

32   J. D. Benck, B. A. Pinaud, Y. Gorlin, T. F. Jaramillo, *Plos One*, 2014, 9, e107942.

33   V. P. Kutyshenko, M. Molchanov, P. Beskaravayny, V. N. Uversky, M. A. Timchenko, *Plos One*, 2011, 6, e28824.

34   S. S. Craig, S. A. S. Craig, M. S. Ganio, C. M. Maresh, H. Greg, K. A. da Costa, S. H. Zeisel, *J. Int. Soc. Sports Nutr.*, 2010, 7, 3.

35   J. Moyer, D. Wilson, I. Finkelshtein, B. Wong, R. Potts, *Diabetes Technol. Ther.*, 2012, 14, 398-402.

36   Z. Sonner, E. Wilder, J. Heikenfeld, G. Kasting, F. Beyette, D. Swaile, F. Sherman, J. Joyce, J. Hagen, N. Kelley-Loughnane, R. Naik, *Biomicrofluidics*, 2015, 9, 031301.

37   X. Wen, B. Wang, S. Huang, T. Liu, M. S. Lee, P. S. Chung, Y. T. Chow, L. W. Huang, H. G. Monbouquette, N. T. Maidment, P. Y. Chiou, *Biosens. Bioelectron.*, 2019, 131, 37-45.

38   B. Wang, B. Koo, L. W. Huang, H. G. Monbouquette, *Analyst*, 2018, 143, 5008-5013.

39   L. A. Escobar, W. Q. Meeker, *Stat. Sci.*, 2006, 21, 552-577.

40   D. S. Asakawa, G. H. Crocker, A. Schmaltz, D. L. Jindrich, *J. Electromyogr. Kinesiol.,* 2017, 34, 6-13.

41   A. J. Bandodkar, W. Z. Jia, C. Yardimci, X. Wang, J. Ramirez, J. Wang, *Anal. Chem.,* 2015, 87, 394-398.

42   C. Boehler, T. Stieglitz, M. Asplund, *Biomaterials, 2015,* 67, 346-353.

43   A. J. Bandodkar, P. Gutruf, J. Choi, K. Lee, Y. Sekine, J. T. Reeder, W. J. Jeang, A. J. Aranyosi, S. P. Lee, J. B. Model, R. Ghaffari, C. J. Su, J. P. Leshock, T. Ray, A. Verrillo, K. Thomas, V. Krishnamurthi, S. Han, J. Kim, S. Krishnan, T. Hang, J. A. Rogers, *Sci. Adv., 2019,* 5, eaav3294.

44   K. Yamanaka, *Jpn. J. Appl. Phys., 1989,* 28, 632-637.

45   V. M. Tolosa, K. M. Wassum, N. T. Maidment, H. G. Monbouquette, *Biosens. Bioelectron.,* 2013, 42, 256-260.

Chapter 4. An Autonomous Wearable System for Diurnal Sweat Biomarker Data Acquisition

4.1. Introduction

Wearable biomarker sensing platforms are poised to catalyze the transition from point-of-lab and point-of-care to point-of-person health and wellness monitoring as they provide frequent, real-time, and contextually relevant measures of informative biomarker molecules. Among the potential wearable solutions, sweat-based sensing modality particularly allows for accessing biomarker molecules non-invasively. Accordingly, various sweat bioanalytical platforms were developed (typically implemented as a disposable biochemical sensor unit interfacing a control/readout circuit module) and utilized to target biomarker molecules such as metabolites, electrolytes, and nutrients.[1-5] However, the presented platforms are functionally limited to one time-point/period biomarker data recording. To acquire biomarker information at multiple points during the day, frequent thermal/exercise-based or iontophoresis-based (manually set up) sessions are required to access sweat, and pristine microfluidic/sensor unit replacements are necessary to avoid sample/sensor contamination. Therefore, the underlying limitations of such wearable sweat platforms prohibit their translation into large-scale and longitudinal personal health monitoring applications.[1-12]

Here, to address such limitations, we devise a multi-compartment wearable system, where each compartment can be programmatically activated to induce/modulate sweat secretion (*via* iontophoretic actuation) and analyze sweat at intermittent time-points. This system was realized within a compact footprint, following an introduced hybrid-flex system design and seamless integration methodology—integrating the required functional modules: 1) an array of

iontophoretic actuation interfaces, where each interface can be independently programmed to activate/modulate sweat secretion; 2) a laser-patterned thin tape-based microfluidic module for sweat sampling and routing; 3) electrochemical sensing interfaces, which are functionalized on an anisotropic conductive adhesive (ACA) substrate to facilitate seamless biomarker signal transduction to the electronics within the microfluidic module; and 4) a kirigami-inspired and multi-layered flexible printed circuit board (FPCB) to execute system-level functionalities, including tunable iontophoresis (to modulate secretory agonist delivery and thus sweat secretion), sensor signal acquisition/processing, and biomarker data display/wireless transmission.

As a self-sufficient solution, the integrated hybrid-flex wearable system realizes core functionalities such as sweat stimulation at the desired time and secretion rate, *in-situ* signal processing, real-time data display, and bidirectional data communication with phone/cloud server. By automating these operations, delivered within the devised multi-compartment configuration, we enabled the tracking of the diurnal profile of glucose, as an illustrative biomarker with clinical significance.

4.2. Experimental Section

4.2.1. Characterization of the programmable iontophoresis (delivered by the hybrid-flex system)

The programmable iontophoresis characterization and diurnal human subject studies were performed with our wearable system. The commercial agonist-loaded hydrogel discs (0.5% pilocarpine nitrate, [13], PILOGEL®, Wescor Inc., South Logan, Utah) were reshaped (using custom-designed 3D printed molds) to fit the semi-annular positive iontophoresis electrode array. The programmable iontophoretic stimulation was then performed following the sweat stimulation settings described in the results section.

4.2.2. Sweat secretion rate characterization using standard lab instruments

The capability to program sweat secretion rate was first examined using standard lab instruments. Pilocarpine hydrogels (1% pilocarpine nitrate) were fabricated, following the previously introduced method.[14] These hydrogels were molded into donut-shaped gels (area: 3.2 cm^2), and were used to iontophoretically stimulate sweat on the volar surface of the two forearms (alternating between the two arms at each point) for the two subjects using a commercial Q-sweat system (WR Medical Electronics Co. Maplewood, MN). By varying the applied current and duration of iontophoresis, the iontophoretic dosage was tuned for each stimulation datapoint. The commercial sweat-rate sensor (Q-sweat, WR Medical Electronics Co.) was mounted onto the skin, at the center (area: 0.8 cm^2) of the donut-shaped positive electrode, to measure sweat secretion rate for the corresponding iontophoretic dosage. The sweat secretion rate was continuously measured for 10 minutes from the time of the stimulation started and data points represent the plateau of the sweat rate.

4.2.3. Electrochemical sensor design and characterization

To fabricate thin-film electrochemical sensors, first, gold (Au) was deposited and patterned on an ACA substrate (9703, 3M, 50 μm). Then, platinum nanoparticles (PtNP) were electro-deposited onto the ACA/Au.[15] The biosensing interface was constructed by electrochemically depositing poly-*m*-phenylenediamine (PPD) layer onto the PtNP/Au/ACA by applying + 0.85 V (*vs*. Ag/AgCl) for 300 s in a fresh phosphate-buffered saline solution (Gibco® PBS, ThermoFisher, pH 7.2) with 5 mM *m*-phenylenediamine (Sigma-Aldrich). A 1% chitosan solution was thoroughly mixed with a glucose oxidase solution (Sigma-Aldrich, 50 mg/mL in PBS, pH 7.2) at a ratio of 1:1 (volume/volume). The glucose sensing interface was realized by drop-casting 1 μL of the

64

aforementioned mixture onto the PPD/PtNP/Au/ACA electrode (4 mm^2).[16] To create the lactate sensor, a 4 μL lactate oxidase solution (Toyobo, 50 mg/mL in PBS) was deposited onto PtNP/Au/ACA electrode and dried at room temperature, followed by drop-casting of a 2 μL 1% Chitosan solution and a 2 μL 3% polyvinyl chloride (PVC, Sigma-Aldrich) solution. To characterize the developed electrochemical sensor, constant potential amperometric measurements were conducted at + 0.3 V *vs*. Ag/AgCl. The amperometric response was recorded by a potentiostat (CHI 660E) or the custom-developed PCB. By drop-casting different concentrations of the target analytes onto the sensors' surface, a series of calibration curves were obtained. The sensor selectivity tests were performed in PBS buffer (pH 7.2) by the stepwise addition of different interfering species and glucose into PBS.

4.2.4. Fabrication and assembly of microfluidic-sensing module

The thin film microfluidic-sensing module consists of an ACA-based sensing layer, a microfluidic structure layer (170 µm-thick, 9474LE double-sided tape, 3M), polyethylene terephthalate (PET, MG Chemicals, ~100 µm), a skin adhesive layer (170 µm-thick, 9474LE double-sided tape, 3M), and a filler layer (Scotch single-sided self-seal laminating sheets, 3M, USA). We use a laser-cutter (VLS2.30, Universal Laser Systems) to form 2D patterns of microfluidic channels/chambers in the microfluidic structure and skin adhesive layers, and biofluid inlets ($d = 0.5$ mm) in the PET and filler layers. The microfluidic-sensing module was assembled by vertically stacking these layers. On one side, the module adheres to the FPCB through the ACA layer, and on the other side, adheres onto skin through the skin adhesive layer. Additionally, the skin adhesive layer (the flap-like patterns) also supports the hydrogel (within a 3D printed encapsulated mold) array interfacing with the skin.

4.2.5. The hybrid-flexible FPCB module

At its core, the electronic module houses a microcontroller (MCU) unit (STM8L – UFQFN20, STMicroelectronics). The MCU was programmed to facilitate system-level functionalities (*i.e.* controlling the iontophoresis and sensing circuitries), data analysis, signal transduction through Bluetooth, and plotting the signal readouts on an onboard LCD screen (st7735 – TFT-LCD, Sitronix Technology Corporation) in real-time. A programmable current source based on a unity-gain difference amplifier (AD8276 – 8MSOP, Analog Devices) was designed to realize tunable iontophoretic actuation. This current source was integrated with an overcurrent protection circuitry using a current shunt monitor (INA282 – 8SOIC, Texas Instruments) as well as software and hardware current control mechanisms that utilize the MCU's Analog-to-Digital (ADC) and Digital-to-Analog (DAC) modules (controlled programmatically on the MCU and through the custom-developed smartphone application). With on-demand switching capabilities, the onset of iontophoresis activation at each compartment was actively controlled. A potentiostat chip (LMP91000, Texas Instruments) was programmed to generate and maintain the + 0.3 V potential across the sensing electrodes and continuously measure the amperometric output of the sensor (~ 40 minutes, after sweat stimulation before/after each meal intake). The analog-front-end in this circuit converted the measured current to voltage. To mitigate the interfering high-frequency noise, the output voltage was filtered out through a fifth-order low pass filter (MAX7422 chip – Maxim Integrated, LPF) with a cut off frequency of 1 Hz.

4.2.6. Human subject testing and institutional review board (IRB) approval

The conducted human subject experiments were performed in compliance with the protocols approved by the Institutional Review Board (IRB) at the University of California, Los Angeles

(no. 17-000170) and the IRB at Stanford University (no. 31310). Healthy subjects were recruited based on the approved IRB protocols. All subjects gave written informed consent before participation in the study. Prior to the on body experiments, the forearm was cleaned with isopropyl alcohol (Sigma-Aldrich), rinsed with deionized (DI) water, and wiped with Kimwipes (Kimtech Science), followed by mounting the device on the forearm.

4.3. Design and operational principle of the hybrid-flex system

The skin adherable hybrid-flex system (Figure 4.1a (1a)) is realized following a vertical integration scheme, integrating various functional modules: miniaturized iontophoresis interfaces, adhesive thin film microfluidic-sensing module, and control/readout electronics (Figure 4.1b (1b)). The system is implemented as a kirigami-inspired multi-compartment configuration, where linear incisions—in hexagonal-shaped FPCB and microfluidic-sensing modules—were utilized to render flap-like compartments, thus providing the mechanical degree of freedom necessary for structural compliance with skin. In this configuration, each compartment can be individually addressed to induce/modulate sweat secretion (*via* iontophoretic actuation) and analyze sweat at set time-points (Figure 4.1c (1c)).

The iontophoretic sweat induction is achieved with the aid of a digitally programmable current source and a miniaturized iontophoresis electrode/hydrogel array. This implementation allows for the tunable delivery of secretory agonist molecules (embedded in hydrogel) underneath the skin, simply by adjusting the iontophoresis current level/duration, thus enabling the modulation of the sweat secretion profile. In our design, the iontophoresis electrodes are monolithically integrated within the FPCB module: the positive semi-annular electrodes fabricated on the

67

backside of the FPCB flaps, radially arranged around a shared circular negative electrode (on the backside of the center of FPCB). Furthermore as shown in Figure 4.1c (1c), the semi-annular design of the positive iontophoresis electrodes facilitates a lateral pathway [5] for the stimulation of neighboring sweat glands (that are vertically below sweat sampling microfluidic interface, but laterally away from the iontophoresis interface). The collection and analysis of secreted sweat is achieved with the aid of a thin-film microfluidic-sensing module, featuring an array of microfluidic sensing chambers, (Figure 4.2 (S1)) where each sensing chamber is paired with an iontophoresis interface. The sensing interfaces are engineered on an ACA film. In this way, the adhesive and vertical conductivity of the film can be exploited to interconnect the transduced signal to the readout circuitry of the FPCB, *in-situ*, *via* monolithically integrated sensing contact pads. By programming the FPCB, the compartments within our system can be activated at set time points during the day to render biomarker readings autonomously and non-invasively. Therefore, as conceptualized in Figure 4.1d (1d), the devised solution presents great potential to facilitate longitudinal monitoring of biomarkers across the general population.

4.4. Miniaturized and programmable iontophoresis interface for sweat secretion modulation

First, the robustness of the iontophoresis current delivery under mechanical deformation was tested under three iontophoresis electrode bending conditions (flat; $\alpha = 60°$, $R = 15$ mm; and $\alpha = 30°$, $R = 10$ mm, Figure 4.3a (2a)), where the applied iontophoretic current was continuously monitored. The results demonstrate that the effect of bending on iontophoresis current was negligible (Figure 4.3b (2b)). Then, the consistency of the iontophoretic operations across all six compartments and for different physiologically relevant skin conditions (~300 Ω to ~100 kΩ [17]) was evaluated, *ex situ*, by monitoring the applied current through representative skin impedance loads. As shown in Figure 4.3c (2c), the iontophoresis current differences across all six

68

compartments were less than 0.9% ($R_{skin} = 47$ kΩ). Similarly, the variation in the load impedances had minimal effect on the delivered current level (Figure 4.3c inset (2c inset)). To evaluate the stability of on-body iontophoresis stimulation by our wearable system, we performed iontophoresis in the presence of body motions with different intensities. Figure 4.3d (2d) illustrates a stable iontophoresis current profile (negligible current fluctuation, coefficient of variation (CV) < 2%) was delivered under varying body motion frequencies and accelerations (from ~0 to ~20 Hz, and from ~0 to ~20 m/s^2 respectively).

By capitalizing on the capability of our system in tuning the iontophoresis current level and duration of the stimulation, we can control the amount of agonists delivered to the glands, thus allowing us to effectively program the secretion profile and adjust the secretion rate/volume. In our iontophoretic setup, the amount of agonist (P), can be estimated to the first order by the equation below, which illustrates the proportionality of P to the product of the stimulation current I and duration t:

$$P = \frac{I\,t\,M}{F} \quad (1)$$

Where F is the Faraday constant (96489 C/mol) and M is the molecular weight of the agonist (*i.e.* 271 g/mol), I in mA, and t in seconds.[18]

To examine our ability to program the secretion rate, first, we performed sweat stimulation (utilizing standard lab instruments) on two subjects, where in each of the cases we varied I and t ($I = 0.5$, 1 mA; $t = 3$, 5 min). As shown in Figure 4.3e, f (2e, f), our sweat secretion characterization results (performed with an evaporimeter) illustrated that higher $I \times t$ conditions (iontophoretic stimulation dosage) led to higher secretion rates for both subjects. We can also exploit our programmable sweat induction capability to ensure harvesting sufficient sweat sample volumes for reliable *in-situ* analysis. To illustrate this point, using our solution, we performed sweat

stimulation (two trials) with different iontophoresis current levels and fixed duration (on nearby spots of the volar surface of the subject's arm) and secretion characterization with a spiral-shaped microfluidic sweat collector (Figure 4.4 (S2)). As shown in Figure 4.3g (2g), for both trials, the increased iontophoresis current led to larger secreted sweat sample volumes. Furthermore, we can exploit our programmable sweat induction capability to elicit sweat secretion at desired time-points during the day, which is instrumental in the envisioned diurnal biomarker monitoring application. To illustrate this point, we deployed our multi-compartment system in a human subject study, where we programmed the compartments to be activated at different time points to induce sweat. As illustrated in Figure 4.3h (2h), sufficient sweat sample volume (> 2 μL) was consistently induced across the six compartments during a day.

4.5. ACA-based electrochemical sensor development and characterization

The electrochemical sensors are fabricated on an ACA substrate, following a mediator-free enzymatic sensor development protocol. Our electrochemical sensing interface consists of an enzyme layer (glucose oxidase), a PPD layer, and a PtNP/Au layer (Figure 4.5a (3a)). The PPD layer serves as a permselective membrane to reject interfering species in sweat matrix [19, 20], and the PtNP/Au layer facilitates the oxidation of the end-product (here, H_2O_2) generated from enzyme-catalyzed reaction. Similar sensor development protocols can be adopted to construct sensing interfaces targeting other biomarkers by incorporating suitable biorecognition and functional layers: for example, ACA-based lactate sensing interface can be created (Figure 4.6 (S3)) by utilizing lactate oxidase as a biorecognition layer, coupled with PVC as a functional layer (diffusion limiting).

The developed glucose sensors were first characterized, by capturing their amperometric responses (using a standard bench-top potentiostat) to a series of solutions with different glucose

concentrations (spanning the typical glucose concentration range in sweat, 0-600 μM). As shown in Figure 4.5b (3b), the responses of the sensors to the glucose concentrations were highly linear ($R^2 = 0.98$). The sensors' sensitivity and the limit of detection were 15.13 ± 0.8 μA/mM/cm^2 and 0.9 ± 0.05 μM, respectively. Furthermore, the amperometric sensor responses measured by the wireless FPCB were compared with those measured by the bench-top potentiostat. The results indicated that the corresponding FPCB and bench-top potentiostat readouts were closely matched ($R^2 = 0.99$, Figure 4.7 (S4)), thereby validating the FPCB's reliable signal acquisition, processing, and transmission capabilities.

To ensure reliable operation in complex biomatrices such as sweat, the selectivity performance of the glucose sensor was characterized by measuring its responses to a diverse panel of physiologically relevant interfering species, including electrolytes, electroactive species, drugs, sweat agonist, proteins, and other small molecules (listed in Figure 4.5c (3c)). As shown in Figure 4.5d (3d), the response of the glucose sensor to the interfering species was negligible, while exhibiting step-wise current responses to glucose concentration increments.

To evaluate the sensors' preserved sensitivity for the duration of the envisioned on-body application (several hours), their amperometric responses were measured, in ambient conditions, every 2 hours. As illustrated in Figure 4.5e (3e), the sensors presented minimal sensitivity variations ($\Delta < 4.4$ %) over the period of 10-hours.

Furthermore, the effect of mechanical deformation on the generated signal, along the sensor-circuit interconnection pathway (from the sensing interface to the FPCB contact pads), was characterized by recording the sensor-integrated FPCB's amperometric responses under different bending conditions (flat and $\alpha = 60°$, $R = 15$ mm). As shown in Figure 4.8 (S5), the induced bending had a negligible influence on the signal ($< 5\%$). The constancy of the adhesion between

the microfluidic sensor substrate (ACA) and the circuit board's contact pad was evaluated by performing 180° peel adhesion test [21] as depicted in the inset of Figure 4.5f (3f), and was compared to the adhesion force between skin and the skin adhesive layer of the microfluidic module. As shown in Figure 4.5f (3f), the adhesion force between the skin and the skin adhesive layer was ~0.3 N/cm, meeting the skin adhesion limit (< 0.5 N/cm [22, 23]). The adhesion force between the microfluidic-sensing module's substrate and the circuit board metal contact pad was ~11.5 N/cm, indicating a relatively strong adhesion between the microfluidic and circuit modules (as compared to the adhesion force at the skin interface).

4.6. Integrated system for autonomous diurnal sweat sampling and analysis

The custom-developed wireless FPCB module integrates the required circuitries to implement system-level operations, including addressable and programmable iontophoretic-actuation and electrochemical sensor signal acquisition *via* six dedicated channels, as well as signal processing, and real-time biomarker data display (Figure 4.9a, b (4a, b)). This FPCB can bilaterally communicate with a custom-developed smartphone application, *via* Bluetooth, to receive/transmit the command signals (to set the desired mode of operation for each of the compartments) and the biomarker data (Figure 4.10 (S6)). Upon processing the received command signals, the MCU automatically activates the iontophoretic circuitry and addresses the desired compartments (with the aid of multiplexers) to perform sweat stimulation at the intended time points (following the instructed iontophoresis settings). After the deactivation of the iontophoresis circuitry and following the MCU-generated instructions, the electrochemical sensing circuit continuously samples and processes the amperometric signal, thereby rendering biomarker data acquisition (Figure 4.11 (S7), and supplementary methods).

The complete hybrid-flex system—consisting of the microfluidic-sensing and iontophoresis interfaces, integrated with the two-layered FPCB module—was deployed to acquire biomarker data at intermittent periods during the day and capture the biomarker's diurnal profile. Specifically, it was utilized to monitor the sweat glucose levels of a human subject over six periods—before and after the consumption of three main meals during a day—where the sweat glucose readings during each period were captured by a designated compartment. Before and after each meal intake, sweat was iontophoretically stimulated for 5 minutes at 0.6 mA, and with the aid of the inbuilt pressure of the stimulated sweat glands, the harvested sweat sample was routed to and subsequently analyzed within the microfluidic sensing chamber of the same designated compartment (Figure 4.9c (4c)). As shown in Figure 4.9d (4d), the changes in the baseline of the acquired diurnal sweat glucose profile reflected the elevation in glucose levels upon meal intake. This trend is aligned with previously reported observations, in which manual intervention was required to capture the glucose level for each time period.[24]

4.7. Conclusion

In conclusion, we devised a hybrid-flex multi-compartment autonomous wearable system, where each compartment can be activated, at desired time periods, to induce sweat—at programmable secretion rates—for *in-situ* biomarker analysis. To inform its clinical utility, we deployed this system in a human subject study aimed at tracking the diurnal sweat glucose profile, in which the results illustrated the elevation of sweat glucose upon the intake of each of the three main meals. The autonomous functionality and multi-compartment configuration of our solution eliminates the need for manual intervention for the device substitution (unlike the previously reported solutions requiring pristine microfluidic/sensor unit replacements to avoid sample/sensor

contamination). Equivalently important, the demonstrated autonomous sweat acquisition and analysis capability can be exploited to adaptively sample contextual biomarker readings based on the user's need, behavior, and activity.

Furthermore, the generalizability of the introduced sensing system design and integration methodology allows for the integration of other electrochemical sensing interfaces to track the diurnal profiles of a wide panel of biomarkers. To this end, the previously reported wearable sensor development protocols can be leveraged, but may need to be optimized, to allow for sensor fabrication on an ACA substrate and vertical integration with our sensing system. Additionally, the versatility of our system design allows for the incorporation of auxiliary sensing interfaces (*e.g.*, sweat pH, temperature), which could be helpful in calibrating the sensor responses for more accurate biomarker level estimation and mitigating the confounding effects due to inter/intra-individual variations.

Toward translating this technology into personal health monitoring applications, large-scale and longitudinal studies are required to contextualize the diurnal sweat biomarkers' data in relation to the user's activities and other physiologically-relevant parameters. Augmenting data analytics techniques with the datasets harnessed by our scalable technology enables the establishment of clinical criteria to interpret sweat biomarkers' readings and provide actionable/personalized feedback to users. In this way, we can establish a non-invasive biomarker monitoring modality that can be scaled across the general population for personalized healthcare.

4.8. Reference

1.	A. Koh, D. Kang, Y. Xue, S. Lee, R. M. Pielak, J. Kim, T. Hwang, S. Min, A. Banks, P. Bastien, M. C. Manco, L. Wang, K. R. Ammann, K. I. Jang, P. Won, S. Han, R. Ghaffari, U. Paik, M. J. Slepian, G. Balooch, Y. Huang and J. A. Rogers, *Sci. Transl. Med.*, 2016, 8, 366ra165.

2.   W. Jia, A. J. Bandodkar, G. Valdés-Ramírez, J. R. Windmiller, Z. Yang, J. Ramírez, G. Chan and J. Wang, *Anal. Chem.*, 2013, 85, 6553–6560.

3.   W. Gao, S. Emaminejad, H. Y. Y. Nyein, S. Challa, K. Chen, A. Peck, H. M. Fahad, H. Ota, H. Shiraki, D. Kiriya, D. H. Lien, G. A. Brooks, R. W. Davis and A. Javey, *Nature*, 2016, 529, 509–514.

4.   H. Lee, C. Song, Y. S. Hong, M. S. Kim, H. R. Cho, T. Kang, K. Shin, S. H. Choi, T. Hyeon and D. H. Kim, *Sci. Adv.*, 2017, 3, e1601314.

5.   S. Emaminejad, W. Gao, E. Wu, Z. A. Davies, H. Y. Y. Nyein, S. Challa, S. P. Ryan, H. M. Fahad, K. Chen, Z. Shahpar, S. Talebi, C. Milla, A. Javey and R. W. Davis, *Proc. Natl. Acad. Sci. U. S. A.*, 2017, 114, 4625–4630.

6.   W. Gao, H. Y. Y. Nyein, Z. Shahpar, H. M. Fahad, K. Chen, S. Emaminejad, Y. Gao, L. C. Tai, H. Ota, E. Wu, J. Bullock, Y. Zeng, D. H. Lien and A. Javey, *ACS Sensors*, 2016, 1, 866–874.

7.   B. Schazmann, D. Morris, C. Slater, S. Beirne, C. Fay, R. Reuveny, N. Moyna and D. Diamond, *Anal. Methods*, 2010, 2, 342–348.

8.   J. Kim, I. Jeerapan, S. Imani, T. N. Cho, A. Bandodkar, S. Cinti, P. P. Mercier and J. Wang, *ACS Sensors*, 2016, 1, 1011–1019.

9.   A. J. Bandodkar, D. Molinnus, O. Mirza, T. Guinovart, J. R. Windmiller, G. Valdés-Ramírez, F. J. Andrade, M. J. Schöning and J. Wang, *Biosens. Bioelectron.*, 2014, 54, 603–609.

10.   A. J. Bandodkar, V. W. S. Hung, W. Jia, G. Valdés-Ramírez, J. R. Windmiller, A. G. Martinez, J. Ramírez, G. Chan, K. Kerman and J. Wang, *Analyst*, 2013, 138, 123–128.

11.   W. Gao, H. Y. Y. Nyein, Z. Shahpar, H. M. Fahad, K. Chen, S. Emaminejad, Y. Gao, L. C. Tai, H. Ota, E. Wu, J. Bullock, Y. Zeng, D. H. Lien and A. Javey, *ACS Sensors*, 2016, 1, 866–874.

12.   W. Gao, H. Y. Y. Nyein, Z. Shahpar, H. M. Fahad, K. Chen, S. Emaminejad, Y. Gao, L. C. Tai, H. Ota, E. Wu, J. Bullock, Y. Zeng, D. H. Lien and A. Javey, *ACS Sensors*, 2016, 1, 866–874.

13. *MACRODUCT SWEAT COLLECTION SYSTEM instruction/service manual Model 3700 SYS*, 2004.

14. D. M. Sletten, K. Kimpinski, S. D. Weigand and P. A. Low, *Auton. Neurosci. Basic Clin.*, 2009, 150, 127–130.

15. C. Boehler, T. Stieglitz and M. Asplund, *Biomaterials*, 2015, 67, 346–353.

16. X. Cheng, B. Wang, Y. Zhao, H. Hojaiji, S. Lin, R. Shih, H. Lin, S. Tamayosa, B. Ham, P. Stout, K. Salahi, Z. Wang, C. Zhao, J. Tan and S. Emaminejad, *Adv. Funct. Mater.*, 2020, 30, 1908507.

17. R. M. Fish and L. A. Geddes, *Eplasty*, 2009, 9.

18. Clinical and Laboratory Standards Institute, *CLSI*, 2009, 29, C34-A3.

19. B. Wang, B. Koo, L. W. Huang and H. G. Monbouquette, *Analyst*, 2018, 143, 5008–5013.

20. X. Wen, B. Wang, S. Huang, T. "Leo" Liu, M. S. Lee, P. S. Chung, Y. T. Chow, I. W. Huang, H. G. Monbouquette, N. T. Maidment and P. Y. Chiou, *Biosens. Bioelectron.*, 2019, 131, 37–45.

21. Y. Zhao, B. Wang, H. Hojaiji, Z. Wang, S. Lin, C. Yeung, H. Lin, P. Nguyen, K. Chiu, K. Salahi, X. Cheng, J. Tan, B. A. Cerrillos and S. Emaminejad, *Sci. Adv.*, 2020, 6, eaaz0007.

22. J. Kim, Y. Hwang, S. Jeong, S. Y. Lee, Y. Choi and S. Jung, *J. Mater. Chem. C*, 2018, 6, 2210–2215.

23. L. Liu, K. Kuffel, D. K. Scott, G. Constantinescu, H. J. Chung and J. Rieger, *Biomed. Phys. Eng. Express*, DOI:10.1088/2057-1976/aa91fb.

24. H. Lee, T. K. Choi, Y. B. Lee, H. R. Cho, R. Ghaffari, L. Wang, H. J. Choi, T. D. Chung, N. Lu, T. Hyeon, S. H. Choi and D. H. Kim, *Nat. Nanotechnol.*, 2016, 11, 566–572.

Chapter 5. The future work

5.1. Compliant conductive materials: a class of composites with decoupled mechanical and electrical properties' design space.

Inherently deformable, reconfigurable, and deployable electrical materials with high performance are revolutionary building blocks to different fields such as solar array of spacecraft, implantable/wearable electronics, artificial intelligent robots, and next-generation consumer electronics. However, prevalent high-performance electric materials including conductors (e.g., Au, ITO) and semiconductors (e.g., silicon, perovskite) are all rigid and mechanically fragile. Their electrical performance will be significantly degraded (even under minimal deformation because of stress-induced defects nucleation and growth) until entirely function loss at around 1% strain. To solve this problem, unlike conventional methods, we allow these inevitable defects existing, and growing in brittle materials under large strain. However, we construct 3D current density field within materials to harmonize with designed 3D strain field under deformation (here, bending) to route electrons away from defects. By leveraging this method, we fundamentally decouple materials' electro-mechanical properties conjugation to enable fully/reversibly folding (down to ~ 127 um) a class of traditional brittle thin film electric materials into any 3D compliant configurations far beyond its crack onset strain without compromising their conductivity. I define this class of conductive materials as compliant conductors and the electronic devices based on these materials are complaint electronics. The fundamental difference between compliant electronics and traditional flexible electronics is that the mechanical failure does not equal to electrical failure for compliant electronics.

Specifically, compliant conductors are synthesized by laminating µm-thick metal (here, 200 nm Au as an example) coated ACF. During bending, the upper layer Au will experience tension

(causing crack) while the bottom layer is under compression (difficult to form cracks). Therefore, electrons can automatically transmit through these cracks between two Au layers via anisotropic vertical conduction of the middle ACF (50 µm). Consequently, compliant Au resistance has minimal variation (<5%) without electrical failure during sharp folding (bending radius: 127 µm) while the control samples (conventional Au flexible electrode as Au patterned on the top surface of elastomer) shows a large resistance increase before the electrical failure (Figure 5.1a, b). To improve the generalizability of the devised design principle, I also synthesized compliant indium thin oxide (ITO). As we all known, ITO is a more brittle conductive material compared with Au. However, as shown in Figure 5.1c, d, compliant ITO still shows a minimal resistance variation (<5%) without electrical failure during sharp folding (bending radius: 127 µm).

5.2. A soft strain-resilient AgNW-based composite as electrochemical electrode for biomarker sensing

Flexible electrodes (active area) and metal traces (interconnect) that allow electrical conductance to be maintained during mechanical deformation are critical for the development of wearable sensing devices. However, conventional thin-film metal electrodes and interconnects on elastomeric substrates can suffer from unexpected distortions of electrical (*e.g.*, disconnection) properties after the onset of mechanical fracture across the metal. Moreover, preservation of electrochemical properties of metal electrodes during mechanical deformation is required to create reliable wearable electrochemical sensing devices, which has been rarely explored. Here, we developed a grafted stretchable electrode structure by decoupling the electrodes and their interconnects, which leveraged the superior performances of stretchability of silver nanowire network and metal patterned anisotropic conductive film (as shown in Figure 5.2). This unique

79

structure significantly enhanced both strain-resilient electrical and electrochemical functionalities of thin-film metal electrodes under bending conditions (as shown in Figure 5.3). Figure 5.4 demonstrates that the grafted electrodes can been further utilized to construct multiple high-performance electrochemical sensors (*e.g.*, pH, glucose, pharmaceuticals). As an example, the constructed sensors coupled with a miniaturized circuit board are implemented to achieve *in situ* wound monitoring in mice.

Figures
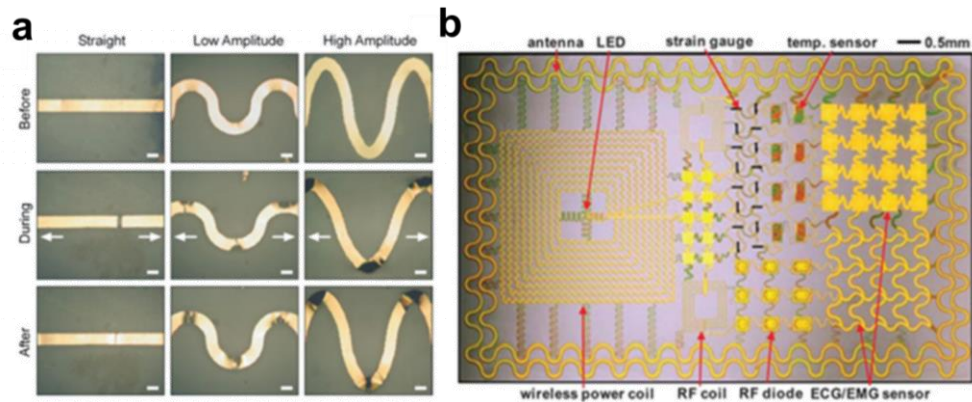
Figure 1.1 Stretchable conductors. (a) Serpentine-based stretchable conductors. (b) Implementation serpentine-based stretchable conductors as interconnects in epidermal electronics.
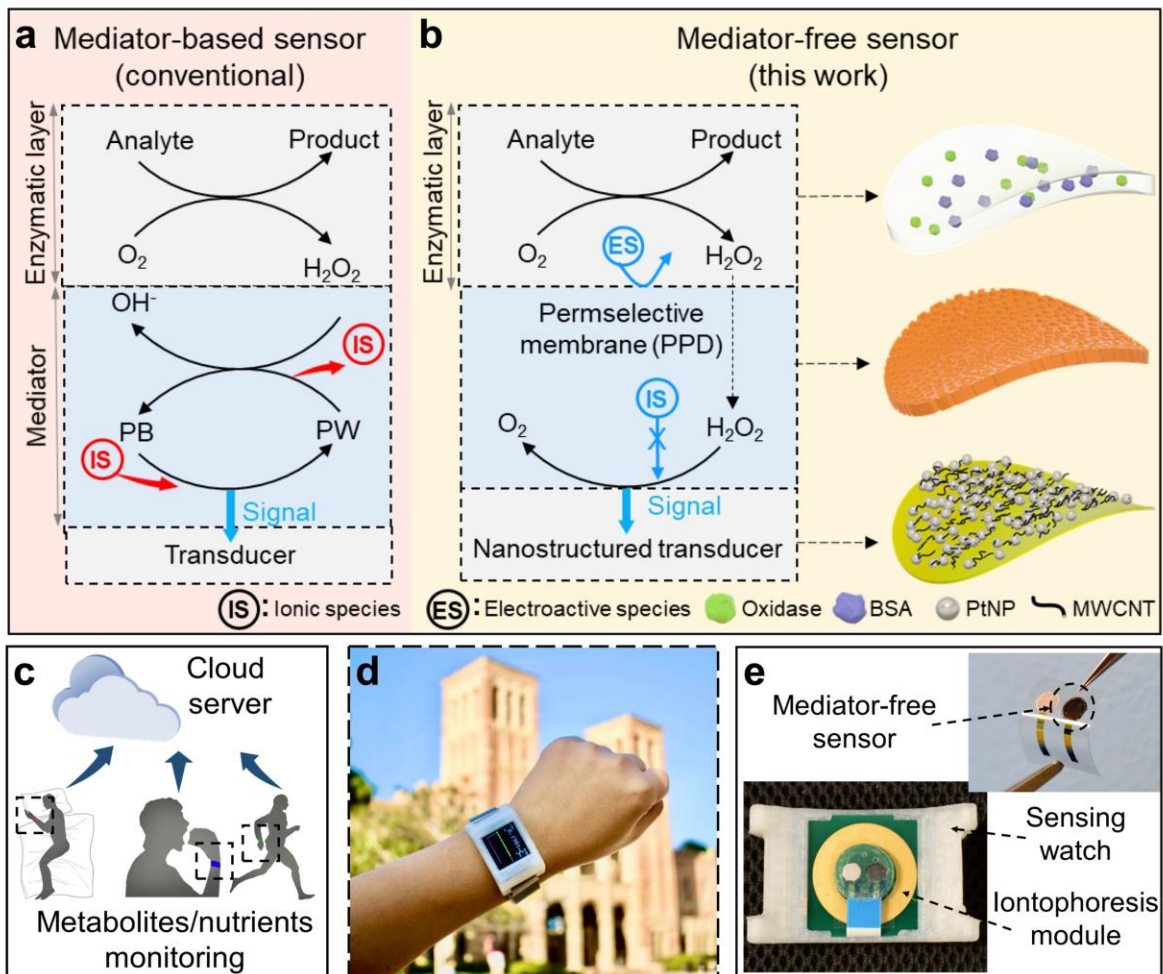
Figure 2.1. A mediator-free electroenzymatic wearable sensing system. (a) Reaction schematic of a conventional mediator (PB)-based electroenzymatic sensor. (b) Reaction schematic of the devised mediator-free electroenzymatic sensor. The sensor interface includes an enzymatic layer, a permselective membrane (PPD), and a MWCNT/PtNP-based H_2O_2 electroanalysis layer. (c) Conceptual illustration of different application scenarios for the devised sensing system, which allows for wireless metabolite and nutrient data acquisition to transmit to a cloud server. (d, e) A complete wearable sensing system in the form of a smartwatch, consisting of a mediator-free sensor interfacing a readout circuit board (with an optional iontophoresis module for on-demand sweat induction).
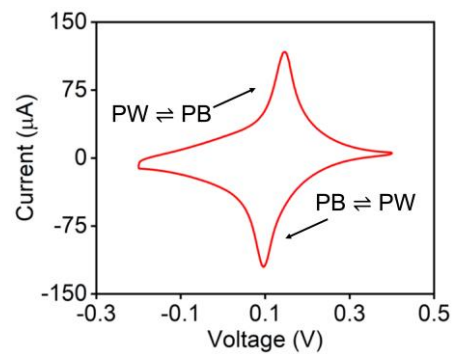
Figure 2.2. CV diagram of a representative PB-based sensing interface. The redox peaks are the characteristic features of Prussian Blue, indicating its successful deposition.
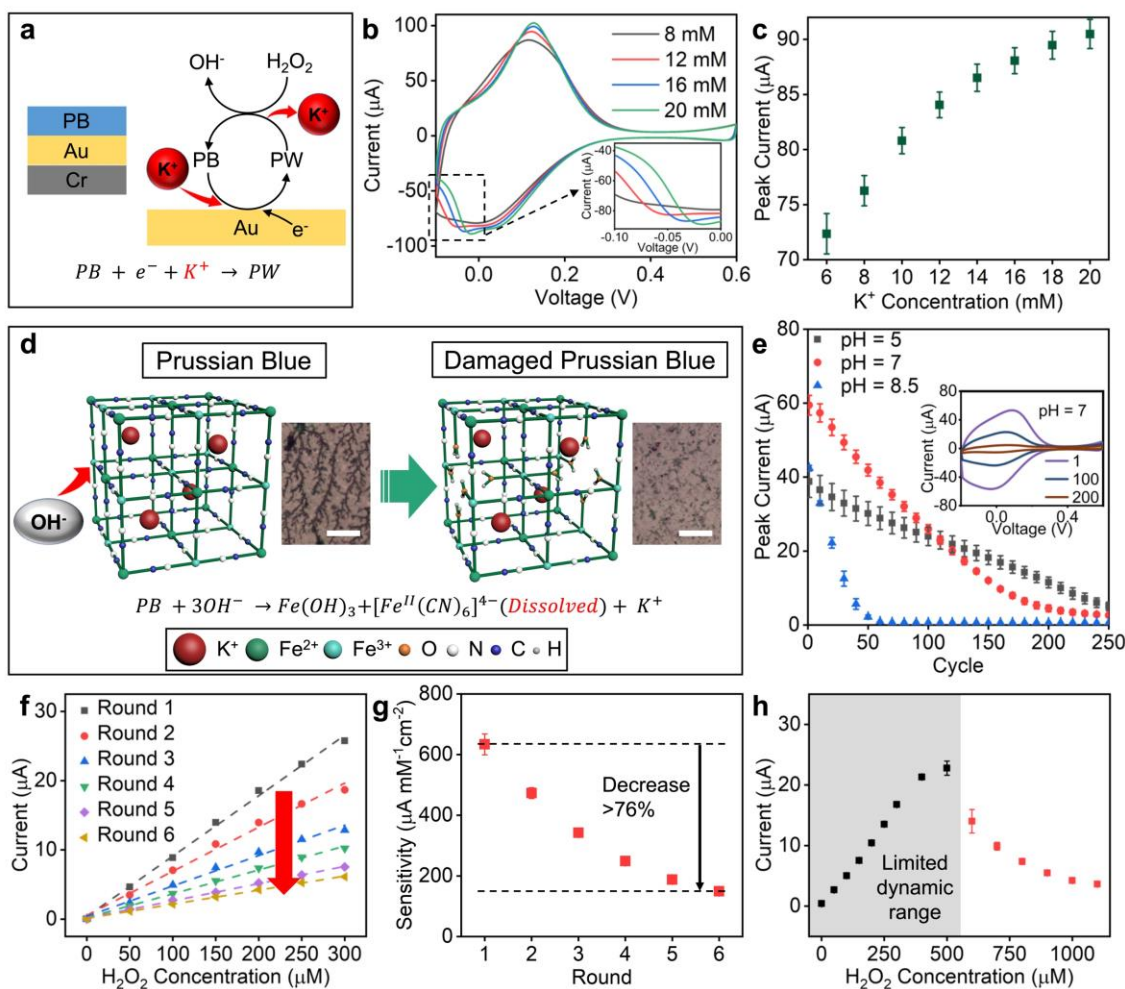
Figure 2.3. Characterization of the PB-based sensing interface's fundamental limitations. (a) Reaction schematic of H_2O_2 sensing (right) using a PB-based sensing interface (left). (b) CV diagrams generated by a representative PB-based sensing interface in response to testing buffer with different concentration levels of K^+ (8 mM, 12 mM, 16 mM, 20 mM, spanning across the concentration range of K^+ in eccrine sweat). Inset shows partial CV diagrams to highlight the increasing trend of the subsidiary cathodic peak current levels with increasing K^+ concentration levels in the buffer. (c) CV subsidiary cathodic peak current levels versus K^+ concentration levels in testing buffer (generated by PB-based sensing interfaces, $n = 3$, error bars indicate standard error). (d) Schematics of the crystal structures of PB and OH^- damaged PB. Insets show representative optical images of PB before and after 250-cycle CV scanning (pH = 7, scale bars indicate 0.5 mm). (e) CV cathodic peak current levels versus scan cycle numbers (tested in three pH conditions, 5, 7, and 8.5, generated by PB-based sensing interfaces, $n = 3$, error bars indicate standard error). Inset shows a representative PB-based sensing interface's CV diagrams at cycles 1, 100, and 200 (pH = 7). (f) Six consecutive H_2O_2 calibration plots of a representative PB-based sensing interface. The arrow indicates the decreasing trend of current response levels. (g) The illustration of decreasing H_2O_2 sensitivity upon calibration (six consecutive rounds of H_2O_2 calibrations performed with PB-based sensing interfaces, $n = 3$, error bars indicate standard error). (h) Extended H_2O_2 calibration plot of PB-based sensing interfaces ($n = 3$, error bars indicate standard error), illustrating their limited H_2O_2 sensing dynamic range (shaded in grey). The testing buffer for all the experiments performed was $0.2 \times$ PBS (if unstated, with 1 mM K^+).

84
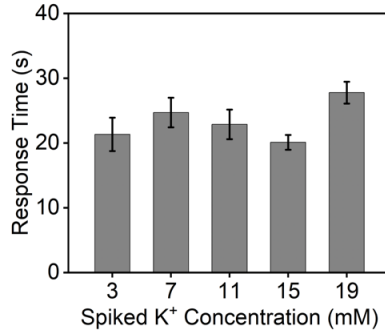
Figure 2.4. The response time of PB-based sensing interface versus spiked K+ concentration levels in testing buffer (n = 3, error bars indicate standard error, tested in 0.2 × PBS containing 20 μm H2O2 and originally 1 mm K+). The response time is defined as the time taken for the sensor's current response to reach 80% of the stabilized current response upon K^+ sample spiking.
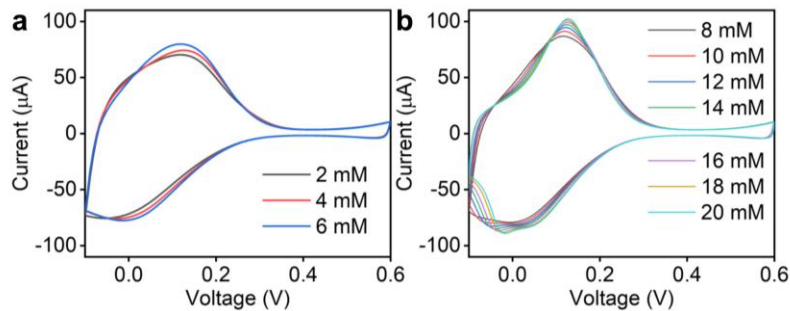
Figure 2.5. CV diagrams of a representative PB-based sensing interface in 0.2 × PBS with different K+ concentration levels. (a) CV diagrams of the PB-based interface for K^+ concentration range of 2 to 6 mM. In this range, the high Na^+ (~ 32 mM) concentration level dominates the interface's response, thus the subsidiary cathodic peaks (< 0 V) are not apparent. (b) CV diagrams of the PB-based interface for K^+ concentration range of 8 to 20 mM. In this range, the subsidiary cathodic peaks become distinct, and the peak current is a measure of PB-to-PW conversion.
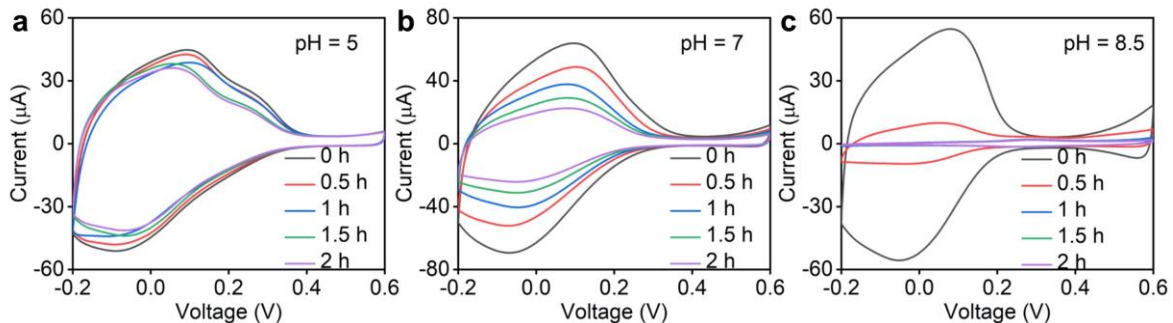
Figure 2.6. CV diagrams of three representative PB-based sensing interfaces in 0.2 × PBS with 1 mm K+ at pH = 5 (a), pH = 7 (b), and pH = 8.5 (c). One-cycle CV scanning was conducted every 30 minutes. The interfaces were immersed in the buffer during the CV measurement period.

85
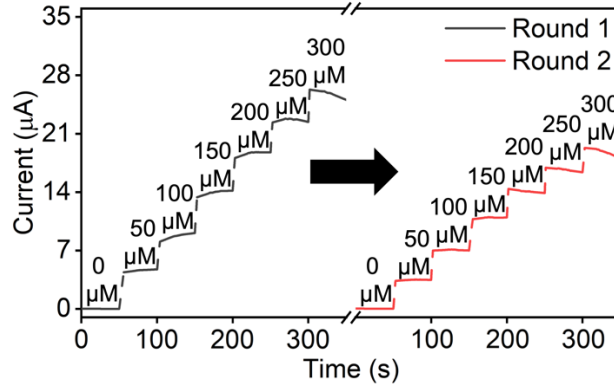
Figure 2.7. Real-time chronoamperometric current responses to H2O2 for a PB-based sensing interface (testing buffer: 0.2 × PBS with 1 mm K+). The arrow indicates the transition from the first to the second round of calibration, where the sensing interface was immersed in the testing buffer containing no H_2O_2 (prior to calibration).
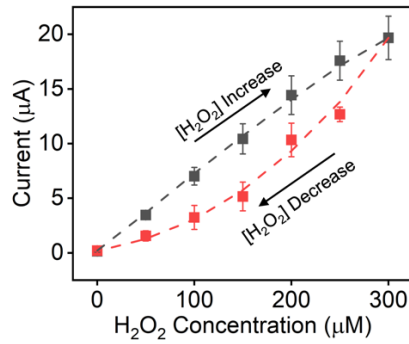
Figure 2.8. Current responses of PB-based sensing interfaces with increasing and then decreasing H2O2 concentration levels in the testing buffer (n = 3, error bars indicate standard error, tested in 0.2 × PBS with 1 mm K+).
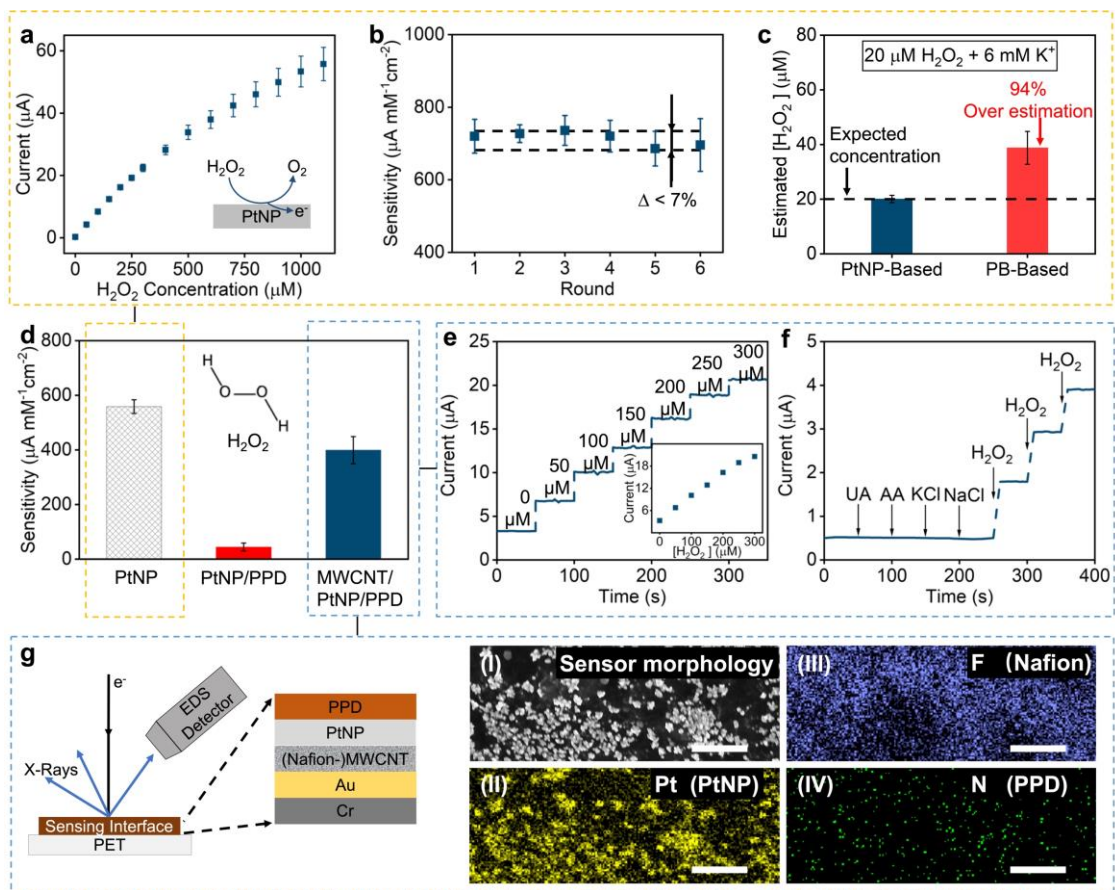
Figure 2.9. Pt-based sensing interface characterization. (a) H_2O_2 calibration plot of PtNP-based sensing interfaces (n = 3, error bars indicate standard error, testing buffer: $0.2 \times$ PBS with 1 mM K^+). Inset shows the reaction schematic of H_2O_2 sensing using a PtNP-based sensing interface. (b) The illustration of stable H_2O_2 sensitivity upon calibration (< 7% change in sensitivity for six consecutive rounds of H_2O_2 calibrations, performed with PtNP-based sensing interfaces, n = 3, error bars indicate standard error, testing buffer: $0.2 \times$ PBS with 1 mM K^+). (c) Estimation of the H_2O_2 concentration level by PB-based and PtNP-based sensing interfaces (n = 3 for both interfaces, error bars indicate standard error) for samples containing 20 μM H_2O_2 with elevated K^+ compared to that of the calibrators (7 mM versus 1 mM in $0.2 \times$ PBS). (d) The H_2O_2 sensitivities of PtNP-based (558 ± 25 μA mM^{-1} cm^{-2}), PtNP/PPD-based (44 ± 15 μA mM^{-1} cm^{-2}), and MWCNT/PtNP/PPD-based (399 ± 50 μA mM^{-1} cm^{-2}) interfaces (n = 3 for all interfaces, error bars indicate standard error, all performed in $1 \times$ PBS). (e) Real-time chronoamperometric current responses of a representative MWCNT/PtNP/PPD-based sensing interface toward H_2O_2 (performed in $1 \times$ PBS). Inset shows the corresponding H_2O_2 calibration plot. (f) Selectivity study with a representative MWCNT/PtNP/PPD-based sensing interface, where its chronoamperometric current response was monitored in real-time in relation to the sequential introduction of the interferents and H_2O_2 (testing buffer: $1 \times$ PBS). The introduction timepoints for the interferents and H_2O_2 are indicated by the arrows. UA: 59 μM, AA: 10 μM, KCl: 2.4 mM, NaCl: 10 mM, H_2O_2: 50 μM. (g) Left: schematic of the EDS setup for the characterization of the (Nafion-)MWCNT/PtNP/PPD-based sensing interface. Right: (I) SEM image of the developed sensing interface; EDS-mappings of Pt to characterize PtNP distribution (II), fluorine (F) to characterize (Nafion-)MWCNT distribution (III), and nitrogen (N) to characterize PPD distribution (IV). Scale bars indicate 4 μm.
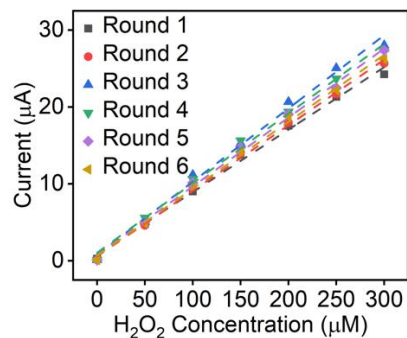
Figure 2.10. Six consecutive H₂O₂ calibration plots of a representative PtNP-based sensing interface.
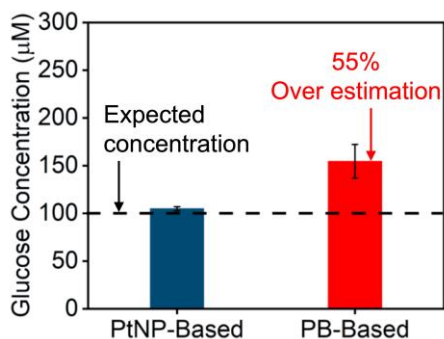
Figure 2.11. Estimation of the glucose concentration level by PB-based and PtNP-based sensors (n = 3 for both sensors, error bars indicate standard error) for samples containing 100 μM glucose with elevated K⁺ compared to that of the calibrators (7 mM versus 1 mM in 0.2 × PBS).
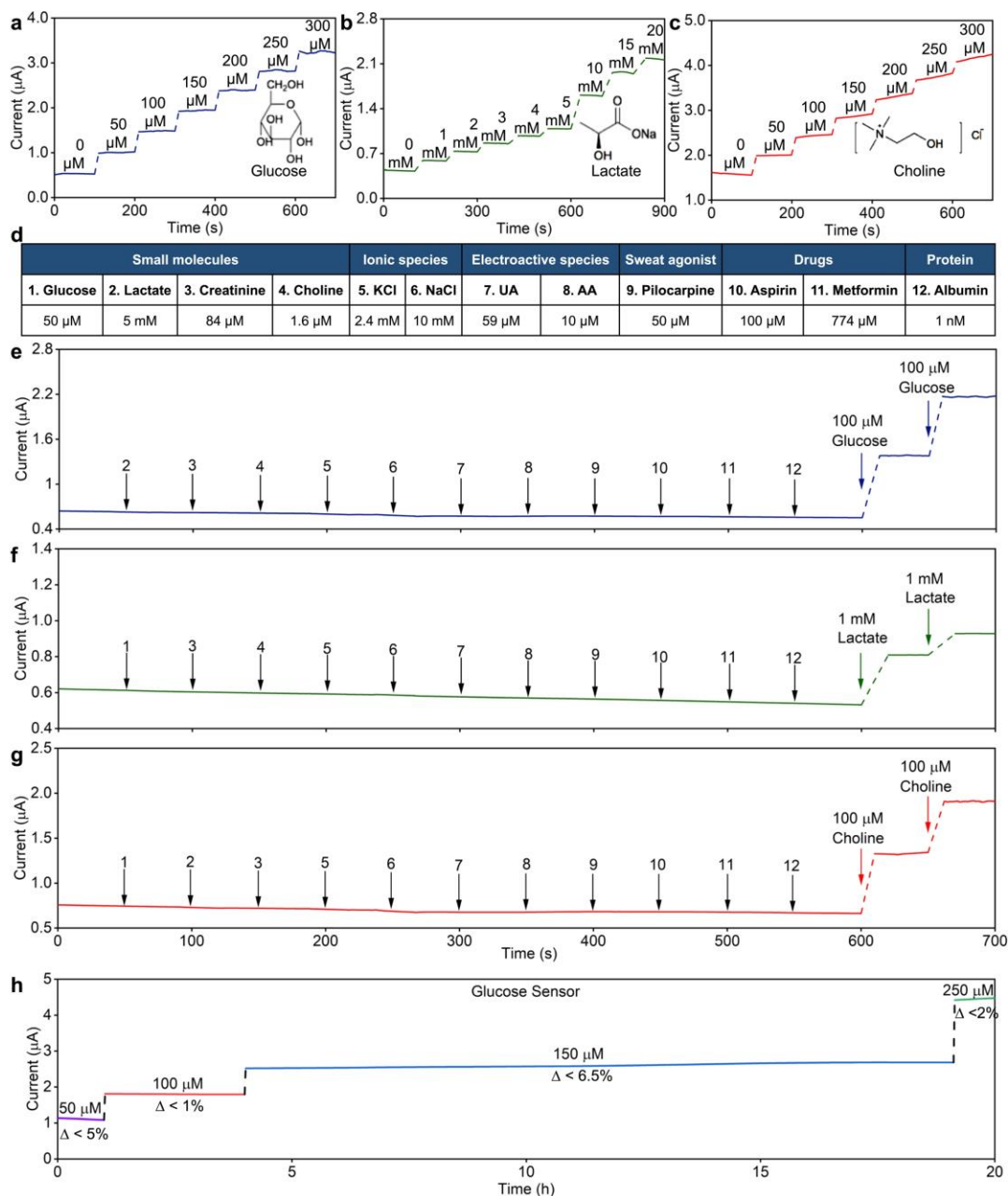
Figure 2.12. Pt-based enzymatic sensors' performance. (a-c) Real-time chronoamperometric current responses to target analytes for a glucose sensor (a), lactate sensor (b), and choline sensor (c). (d) Table of common interferents in biofluids (*e.g.*, sweat). (e-g) Comprehensive selectivity studies for glucose (e), lactate (f), and choline (g) sensors, performed by chronoamperometric measurements to monitor the corresponding sensors' responses to the sequential introduction of the listed interferents and target analytes (the introduction timepoints for the interferents and target analytes are indicated by the arrows). (h) A 20-hour-long chronoamperometric measurement performed with a representative glucose sensor, indicating the sensor's excellent long-term operational stability (the glucose concentration and the sensor current drift are annotated for the corresponding time windows). The testing buffer for all the experiments performed was $1 \times$ PBS.
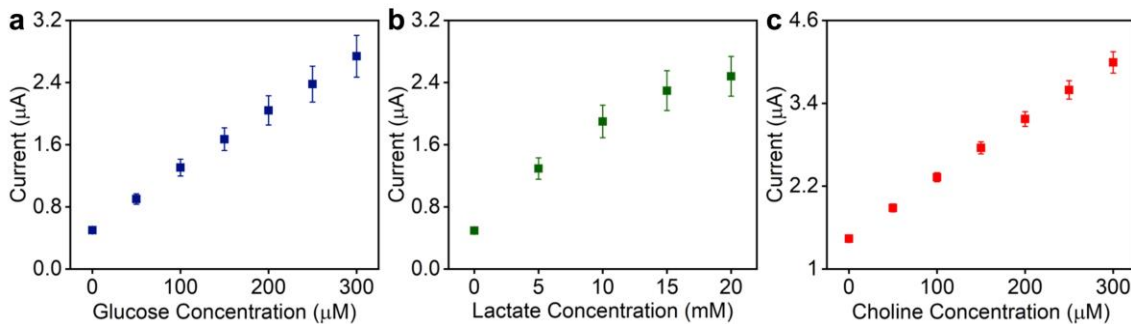
Figure 2.13. Reproducibility of glucose sensors (a), lactate sensors (b), and choline sensors (c) (n = 3 for all the sensors, error bars indicate standard error).
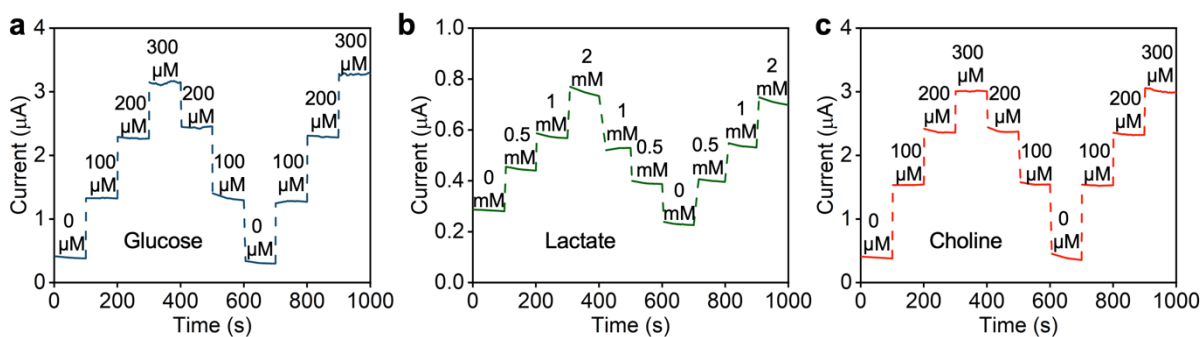
Figure 2.14. Real-time chronoamperometric responses to target analytes with increasing/decreasing/increasing concentration levels measured with a glucose sensor (a), lactate sensor (b), and choline sensor (c).
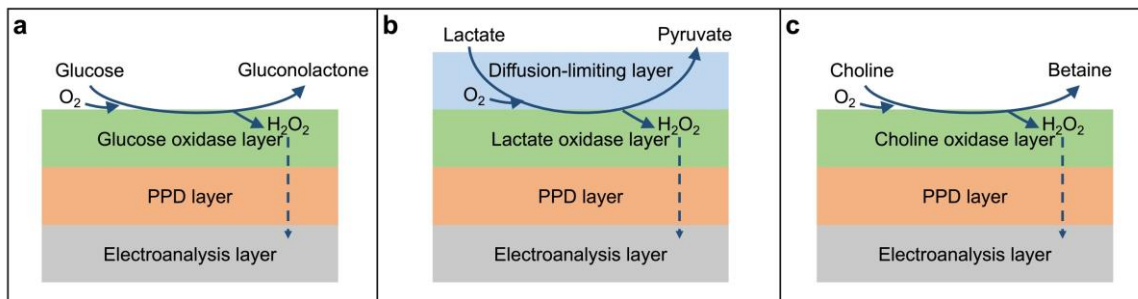
Figure 2.15. Reaction schematics of glucose (a), lactate (b) and choline (c) sensors.

90
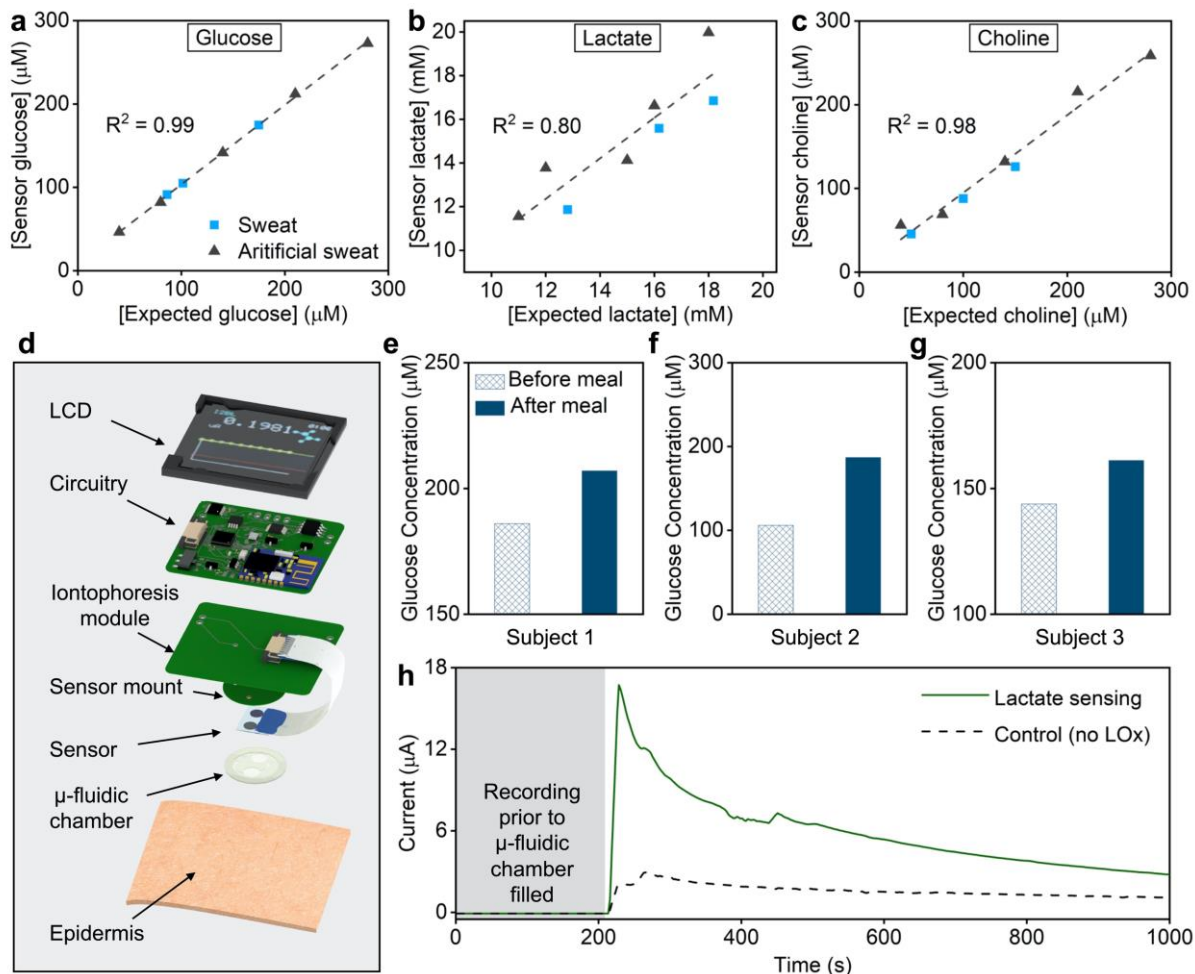
Figure 2.16. Real sample sensing and integrated system on-body biomarker measurement validation. (a-c) The ex-situ sensor-measured glucose (a), lactate (b), and choline (c) concentration levels in artificial sweat and untreated human sweat samples versus the corresponding expected concentration levels of the analytes. The analytes in untreated human sweat samples were quantified by a lab instrument (YSI analyzer for glucose and lactate) or spiked by known amounts (for choline). (d) Exploded view of the mediator-free sensing system, indicating the coupling of the sensor with a custom-developed smartwatch. (e-h) On-body monitoring of subjects' metabolites concentration levels and dynamic changes through various daily events (meal consumption and physical exercise) in different settings (sedentary and active). Measured glucose concentration levels in iontophoretically-induced sweat samples of three subjects before and after consumption of mixed meals (e-g). Continuous sweat lactate measurement of a subject engaged in stationary cycling (h). The solid green line shows the measurement with the lactate oxidase-functionalized sensing system and the control experiment is illustrated with dashed black line, which was performed with a non-functionalized system (without lactate oxidase functionalization).
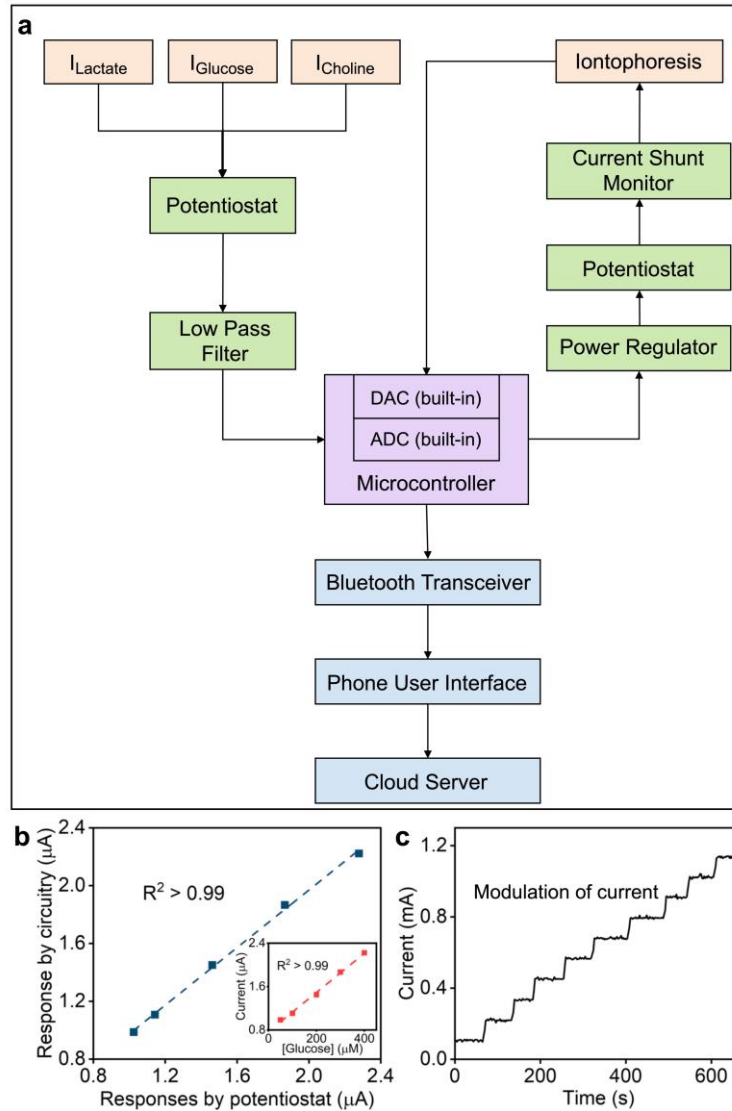
Figure 2.17. Circuitry design and validation. (a) System-level block diagram of the sensor readout and iontophoresis modules. (b) The measured amperometric glucose sensor current response by the custom-developed readout board versus potentiostat (inset shows the corresponding calibration curve obtained by the readout board). (c) Mobile application-based controlled delivery of different iontophoresis current levels.
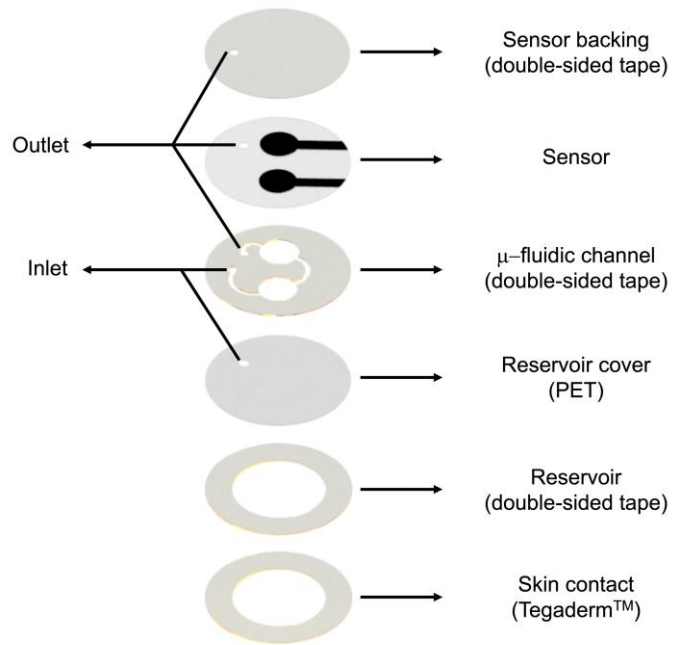
Figure 2.18. Exploded view of the microfluidic interface.
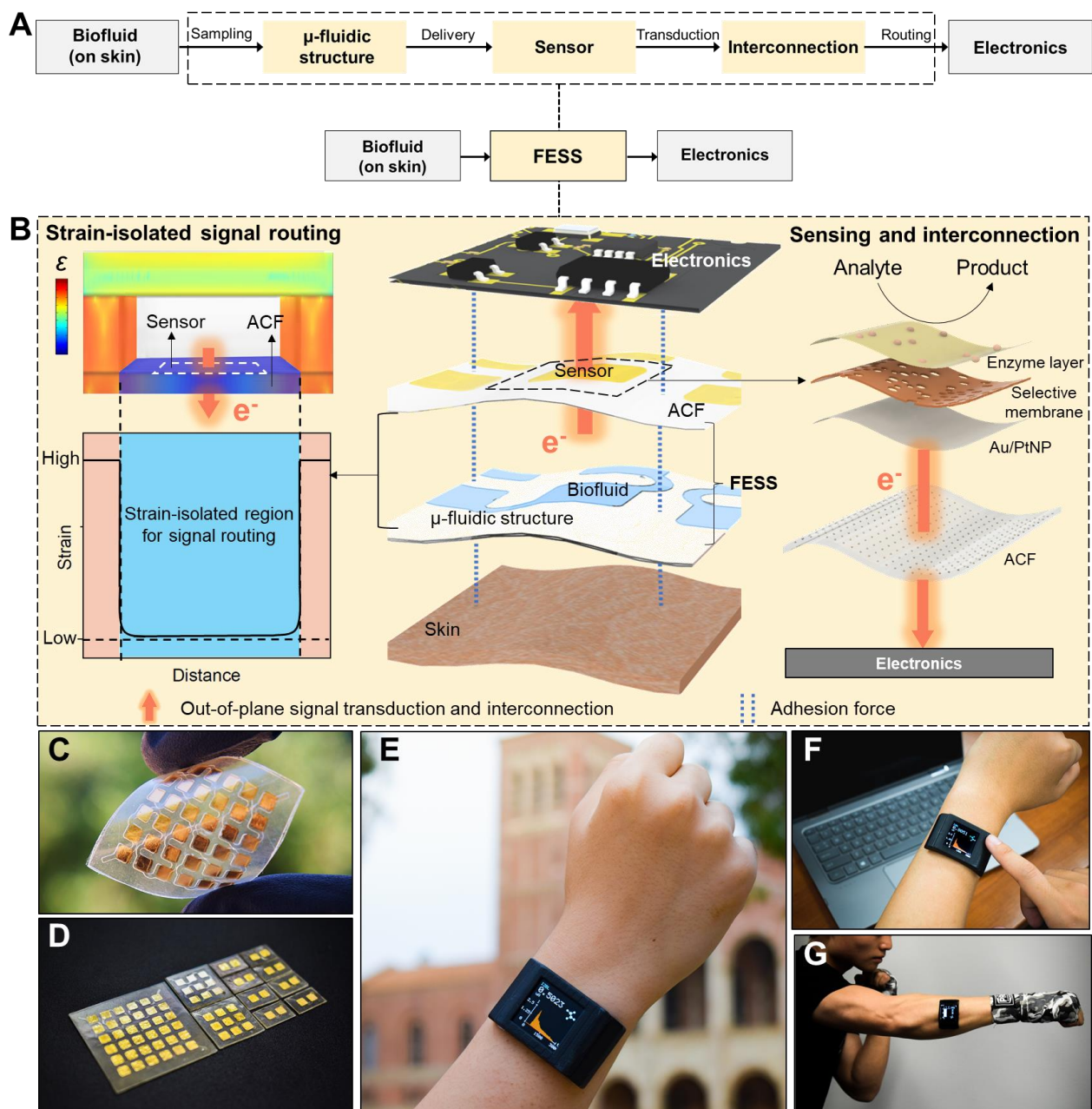
Figure 3.1. Freestanding electrochemical sensing system (FESS) design rationale, implementation, and application. (a) Schematic of the biomarker information delivery pathway enabled by the FESS, illustrating sampling, sensing, and routing of epidermally-retrieved biomarker information to readout electronics through a single entity. (b) Design rationale of the FESS. (c) A representative implementation of the FESS, demonstrating flexibility and no in-plane interconnection. (d) A representative family of FESS devices, containing 1×2, 3×3 and 6×6 electrode arrays. (e) Custom-developed and FESS-enabled smartwatch for biomarker monitoring. (f, g) Deployment of the FESS-enabled smartwatch in stationary (f) and high intensity exercise (g) settings. Photo credit: Peterson Nguyen, Kaili Chiu, Yichao Zhao, University of California, Los Angeles.
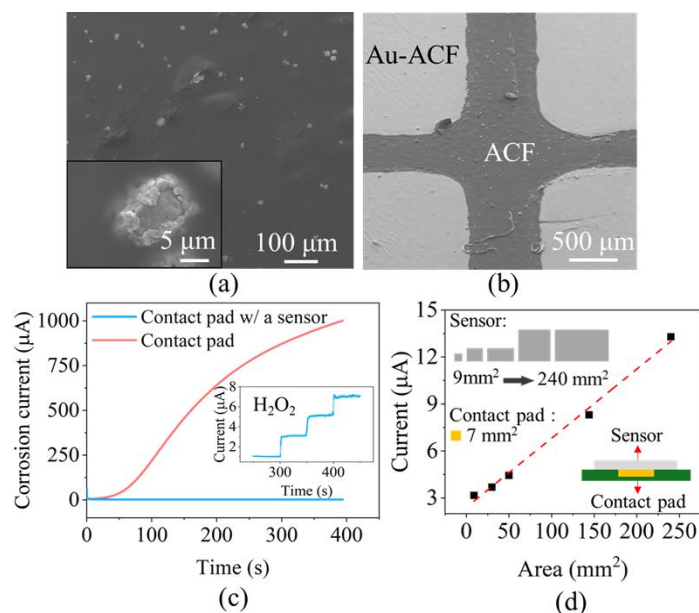
Figure 3.2. ACF-based electrode characterization. (a) SEM image of the ACF. The inset shows a silver particle (conductive agent) embedded in the ACF matrix. (b) SEM image of the Au-patterned ACF. A liner-based shadow mask was used in conjunction with E-beam evaporation to form the desired pattern. (c) Amperometric characterization performed with PCB contact pads (immersion gold) with and without the ACF-based sensing unit in phosphate buffered saline (PBS, 0.5 V vs. Ag/AgCl). The inset shows the electrochemical response of the ACF-coupled PCB interface to sequential H_2O_2 additions (3 steps, 100 μM per step) PBS solution (Ag/AgCl as the reference electrode). (d) Current response of ACF-based sensing units with various surface areas, measured via the same PCB contact pad.
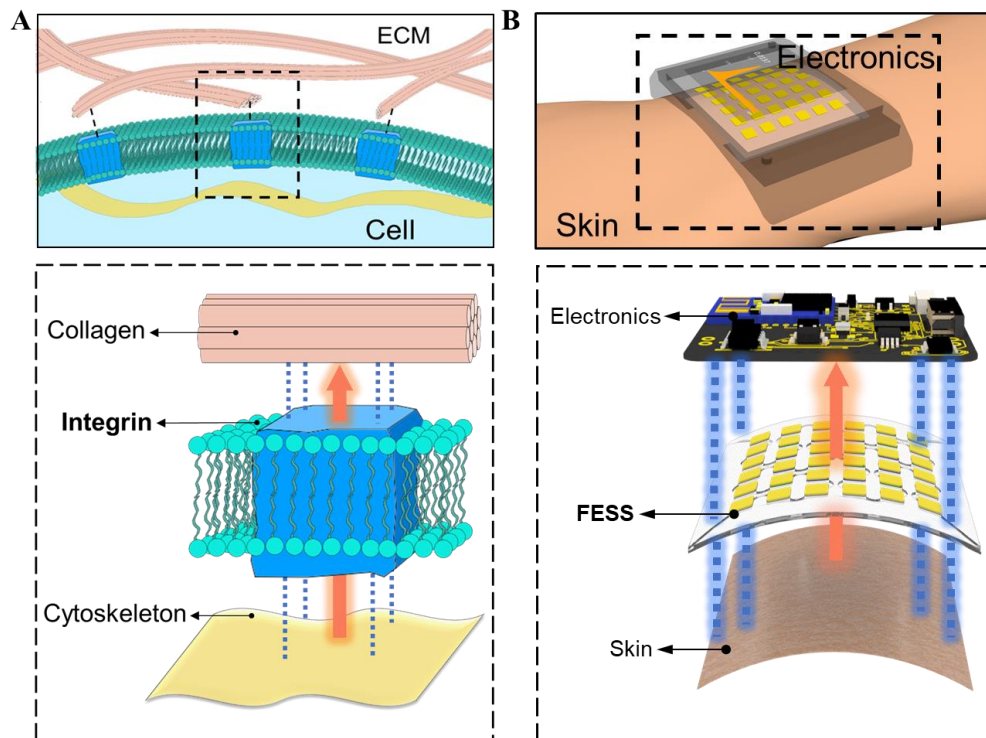
Figure 3.3. Bio-inspired in-situ sensing and signal interconnection. (a) Conceptual illustration of the physiological information exchange between intracellular/extracellular matrices facilitated by cell adhesive molecules (integrin) via sensing, out-of-plane signal interconnection, and double-sided adhesion. (b) *In-situ* sensing, out-of-plane signal interconnection, and double-sided adhesion enabled by FESS, as a single entity, placed between skin and electronics.
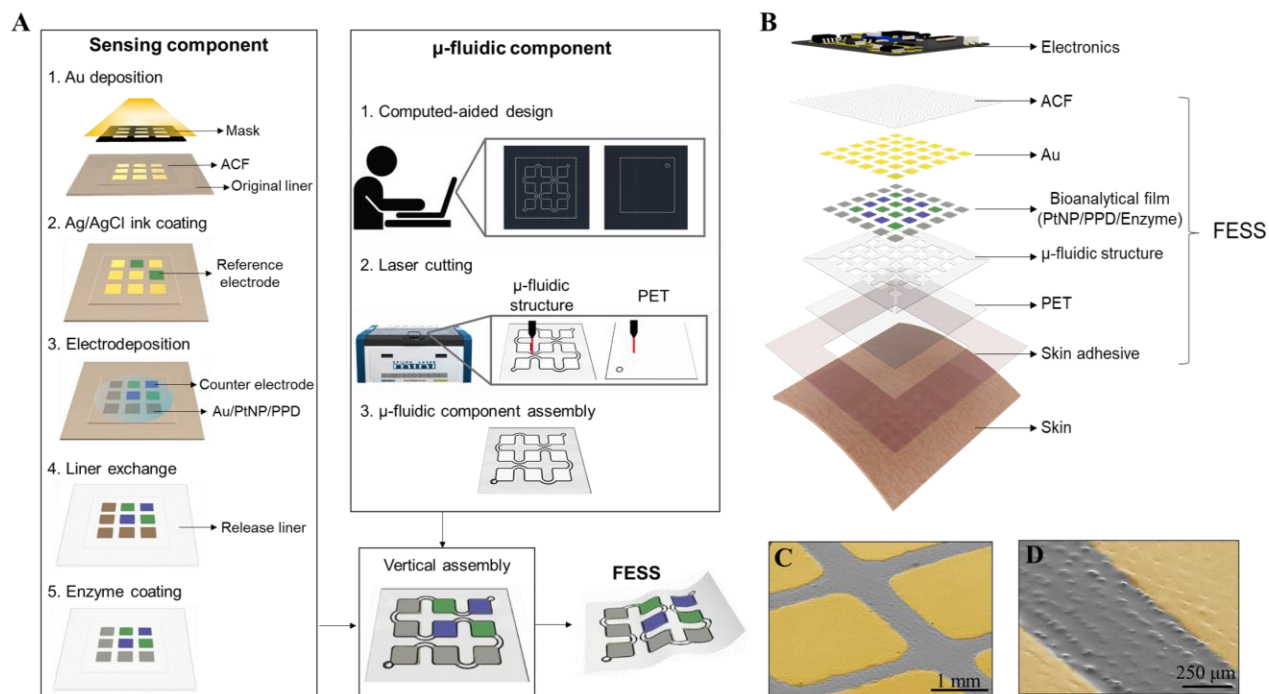
Figure 3.4. Design and fabrication of FESS components. (a) The design and fabrication processes of the sensing and microfluidic components of the FESS. The liner exchange step is visually detailed in Fig. S3. (b) Exploded view of the FESS. (c) SEM image of Au electrodes patterned on the ACF layer. (d) The zoom-in view of the electrode-patterned ACF layer.
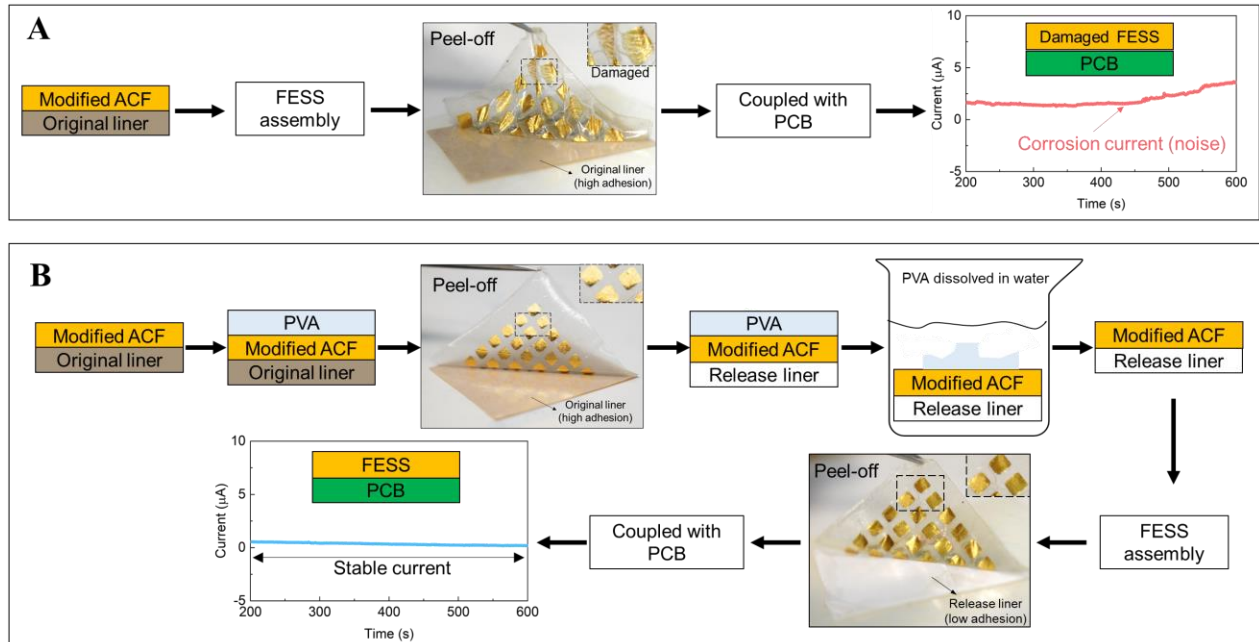
Figure 3.5. Liner exchange procedure for the FESS construction. (a) Demonstration of the device- and operational-level failure of the FESS (constructed without following the devised liner exchange procedure). The FESS is deformed during peeling from the original liner due to the high level of FESS-liner adhesion. The presence of the defects formed on the FESS electrodes subsequently leads to the corrosion of the underlying PCB contact pads, as evident from the unstable amperometric recording of the FESS-coupled PCB (performed in PBS, 0.5 V *vs.* Ag/AgCl). (b) Demonstration of the preserved device- and operational integrity of the FESS (constructed following the devised liner exchange procedure). Here, water soluble PVA layer is used as a backing to facilitate the liner exchange, replacing the original liner with a low adhesion release liner. The preserved operational integrity of the FESS is validated by performing amperometry and recording stable background current (performed in PBS, 0.5 V *vs.* Ag/AgCl). Photo credit: Peterson Nguyen, University of California, Los Angeles.
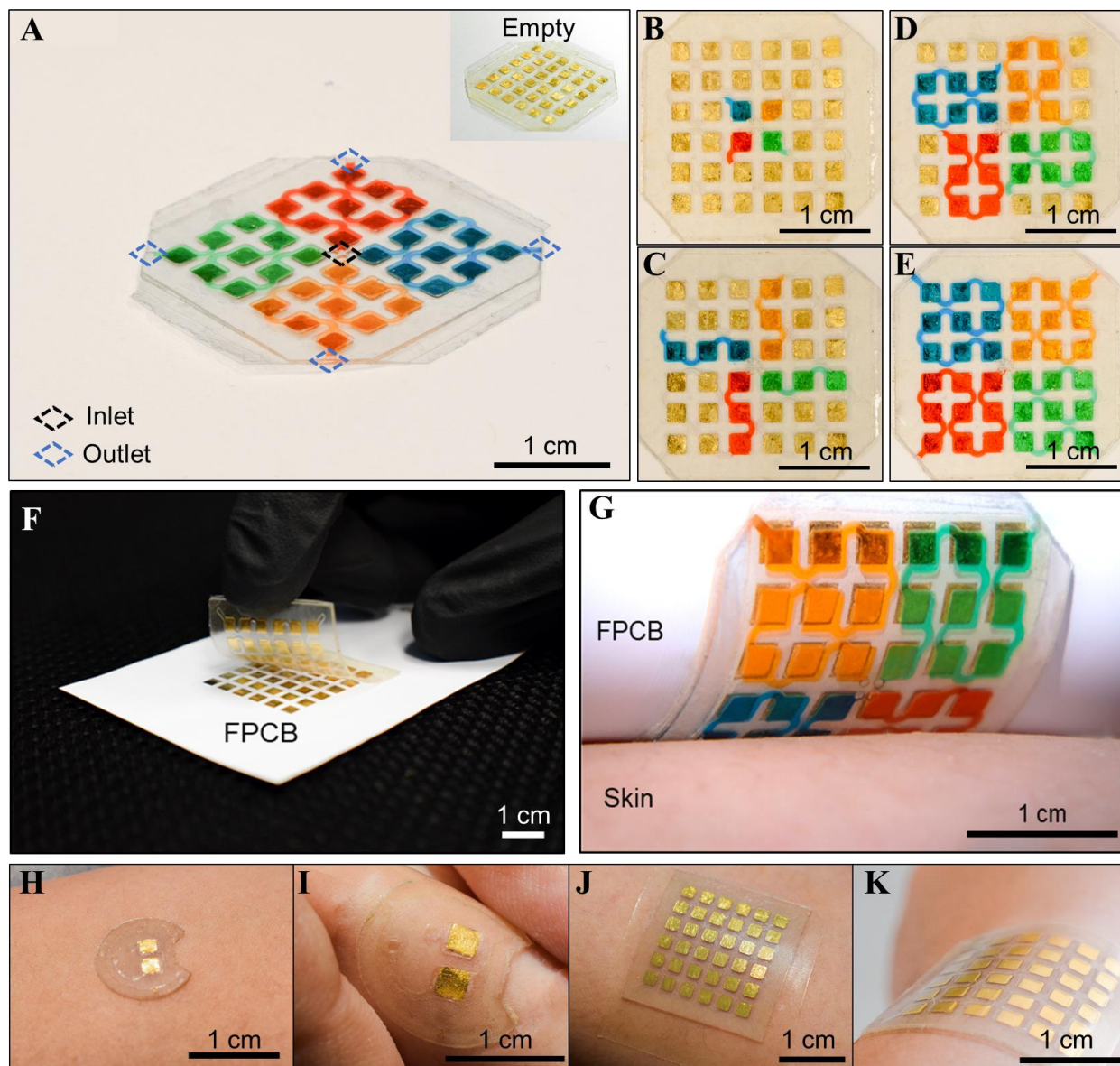
Figure 3.6. Visualization of the microfluidic module of the FESS and its integration with skin and electronics. (a) A representative 6×6-pixel FESS, filled with dye-colored solution to visualize its microfluidic network. Inset shows the corresponding unfilled FESS. (b)-(e) Optical images of the FESS as it is progressively filled. (f) Integration of a representative 6×6-pixel FESS with FPCB via adhesion force. (g) Adherence of the FESS-FPCB with skin via adhesion force. (h)-(k) A representative 1×2-pixel and 6×6-pixel FESS modules adhered to flat/curved skin. Photo credit: Peterson Nguyen, University of California, Los Angeles.
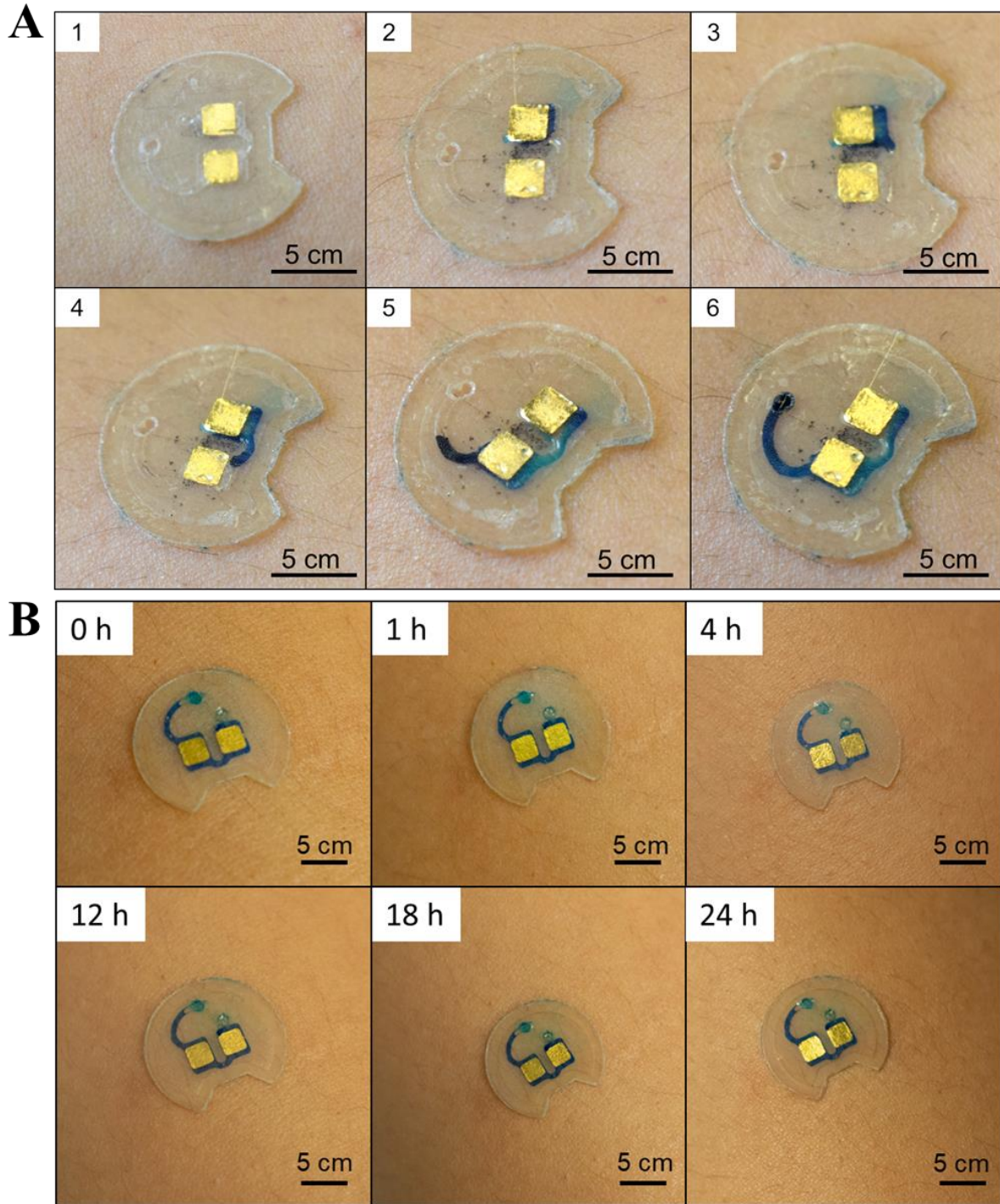
Figure 3.7. Visualization of the FESS-skin reliable adhesion. (a) Sequential optical images of a representative FESS (microfluidic channel volume: 4 μL), adhered to the forearm of a subject (engaged in physical exercise), indicating the leakage-free progression of secreting sweat in the FESS (imaged over a 10-min window). (b) Demonstration of FESS-skin long-term adhesion performed on the forearm of a subject (engaged in routine daily activities) over 24 hours. The FESS was filled with blue-dyed PBS and sealed with epoxy to visualize the microfluidic channel. Photo credit: Peterson Nguyen, University of California, Los Angeles.
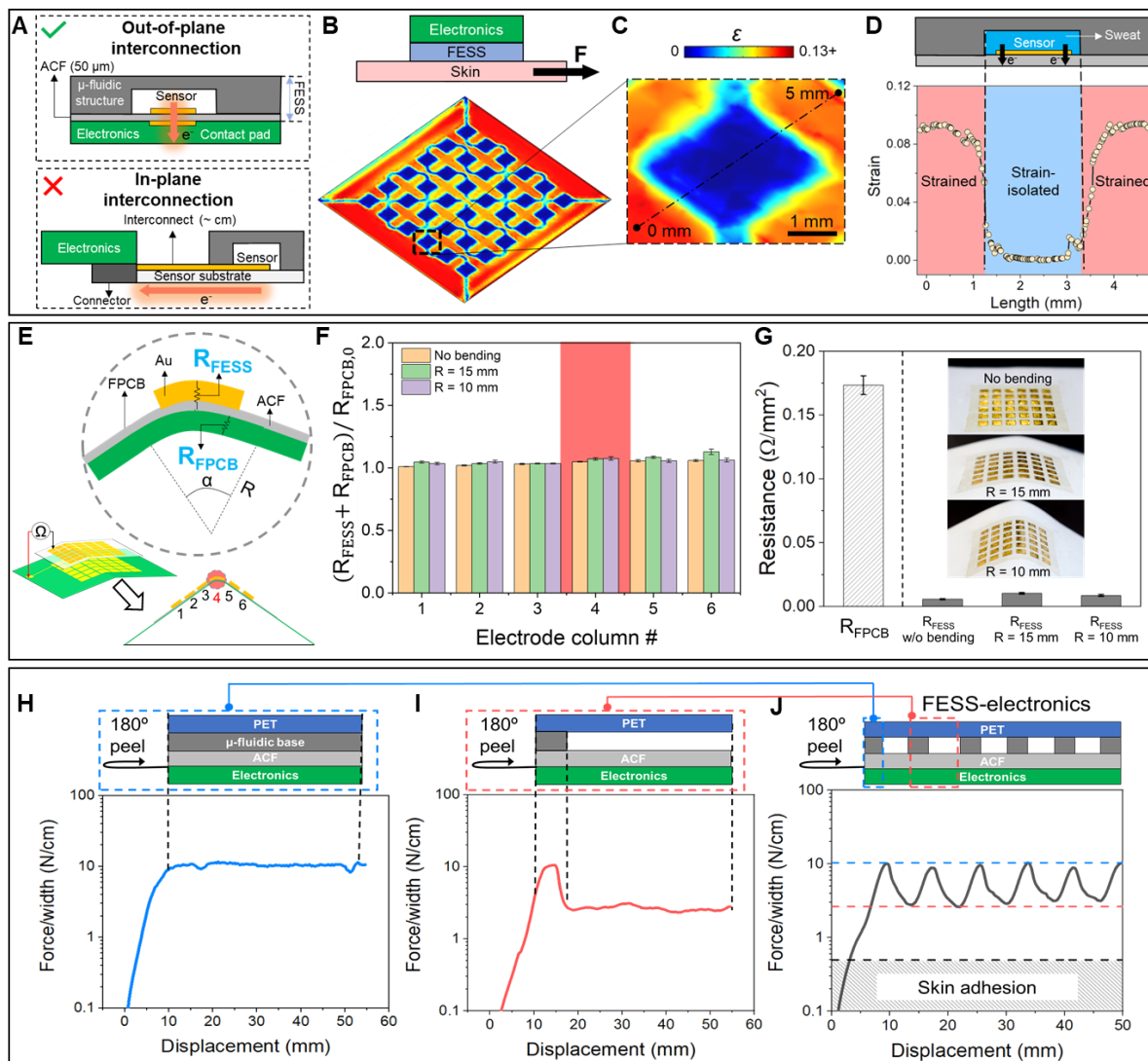
Figure 3.8. FESS strain simulation and characterization of strain-isolated signal interconnection. (a) Illustration of the FESS' out-of-plane signal interconnection *vs.* conventional in-plane signal interconnection. Conventional implementations are constrained to signal routing through highly strained regions, while the devised FESS allows for routing via near-zero strain regions. (b) COMSOL-simulated strain (ε) profile of a representative FESS in the presence of an externally applied shear force, illustrating near-zero strain at the bottom of the microchannel (*i.e.*, substrate-biofluid interface). (c) Corresponding zoomed-in view of the strain profile for one 'pixel'. (d) Strain distribution along the dashed line in Fig. 2c. (e) Out-of-plane interconnection electrical characterization of FESS, performed under different localized bending angles (for an array of 6×6 Au electrodes). (f) Interconnection resistances of the bent FESS-FPCB ($R_{FESS}+R_{FPCB}$), for different localized bending angles (normalized with respect to R_{FPCB} with no bending: $R_{FPCB,0}$). Error bars indicate standard error of measurements across the 6 electrodes within each column. (g) Resistance measurements of the FESS electrodes under different bending angles (n = 36), in relation to the FPCB contact pad resistance ($R_{FPCB,0}$). (h-j) 180º peeling tests characterizing the interconnection adhesion between the PCB and FESS with different backing structures: microfluidic base-ACF (h), microfluidic channel-ACF (i), and a representative microfluidic channel array-ACF (j). Photo credit: Peterson Nguyen, University of California, Los Angeles.
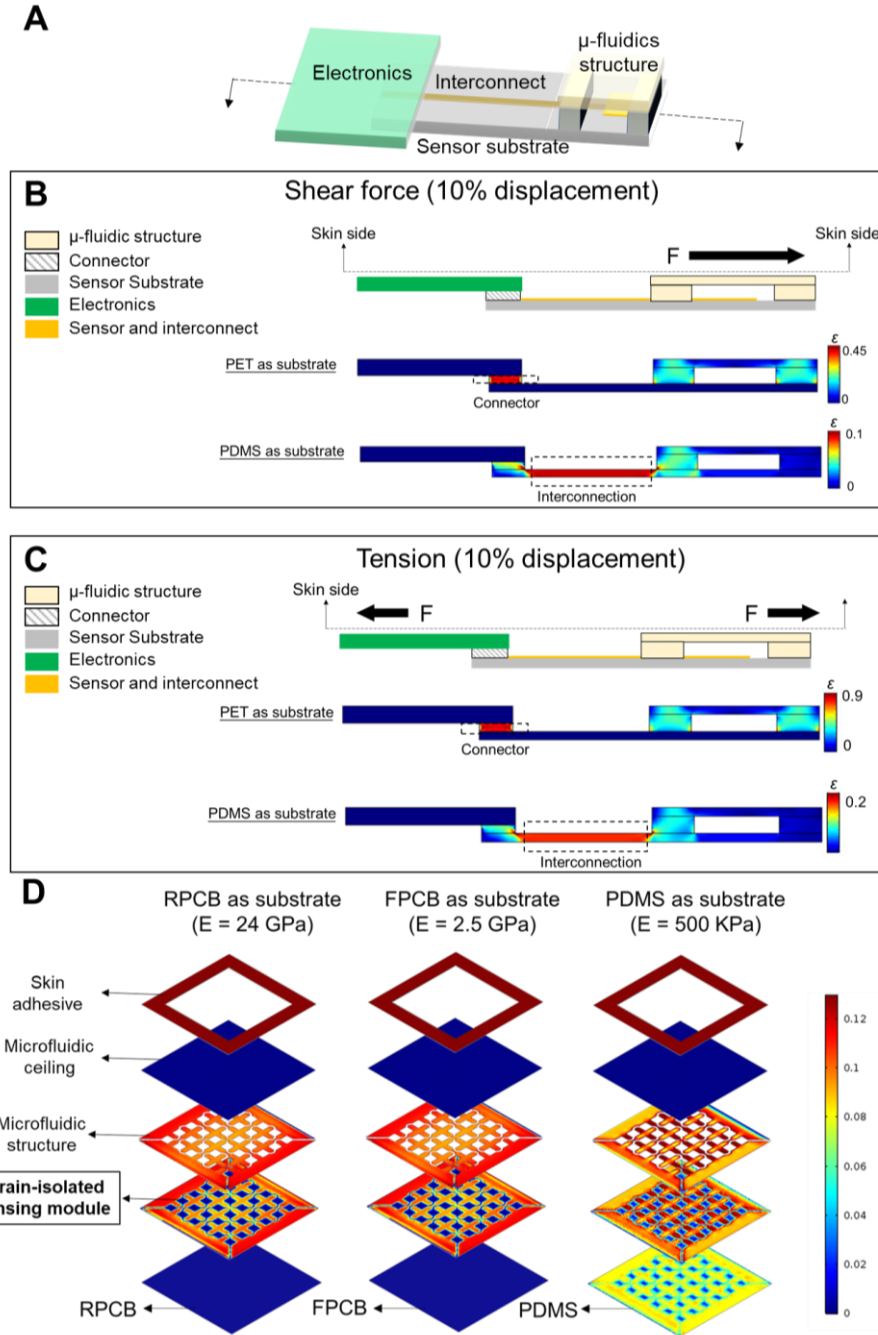
Figure 3.9. Mechanical strain simulation of different implementations. (a) Schematic of conventional in-plane interconnection between sensor and electronics. (b), (c) COMSOL-simulated strain profile of sensor-electronics systems implemented with in-plane interconnections and rigid connectors under shear (b) and tension (c). Both cases of flexible (PET) and stretchable (PDMS) substrates are considered for the sensor substrate. (d) COMSOL-simulated strain profiles experienced by different layers of a representative FESS and in the presence of a shear force. Three different electronics substrate materials are considered: PDMS, polyimide (PI), and Flame retardant 4 (FR4) with corresponding Young's modulus: 500 kPa, 2.5 GPa, and 24 GPa.
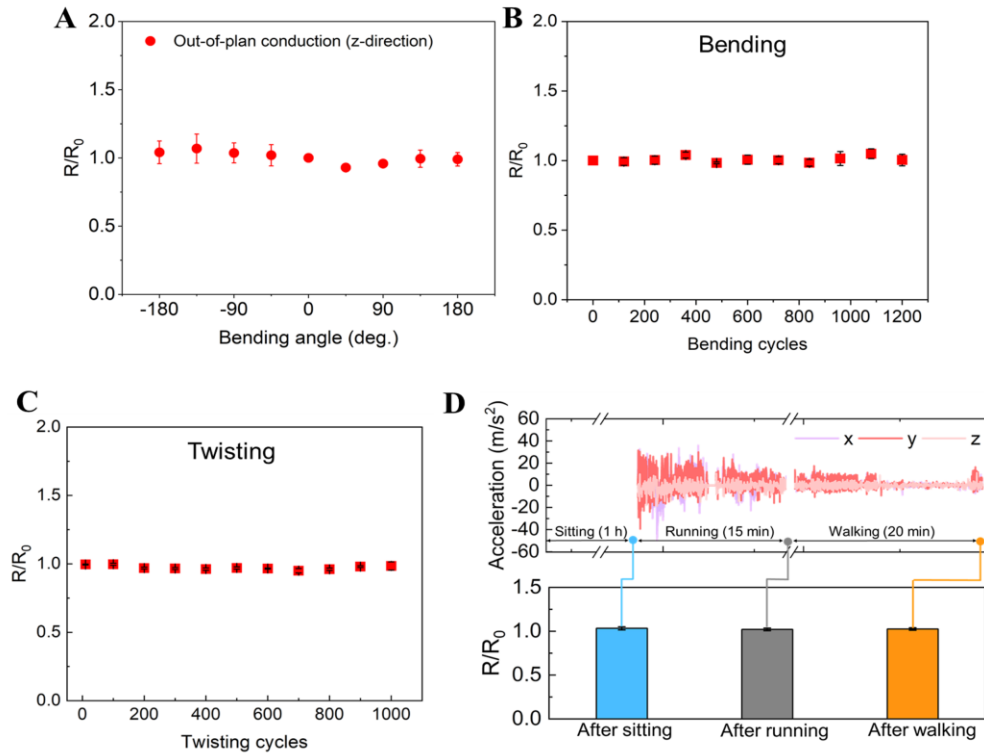
Figure 3.10. The effect of mechanical deformation on the FESS electrical interconnection (ACF) resistance. (a) Interconnection resistance measurements at different bending angles (SE, n = 3). (b) Cyclical interconnection resistance measurements involving repeated 0-to-180° bendings (where the interconnection resistance was probed after each bending under 0°, SE, n = 3). (c) Cyclical interconnection resistance measurements involving repeated twisting. (d) Interconnection resistance measurements before/after different daily activities (the recorded acceleration profile during the running and walking activities are presented atop). R represents the measured interconnection resistance and R_0 represents the measured interconnection resistance at the initial (undeformed) state.

103
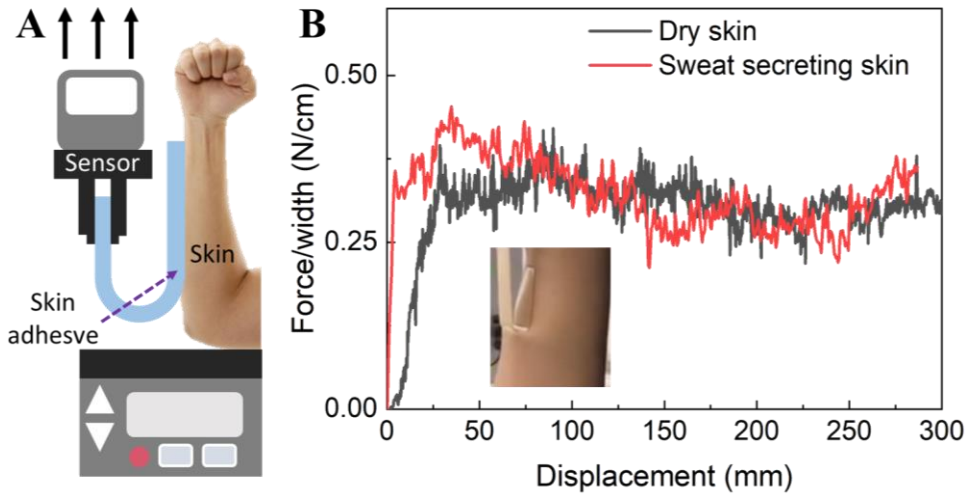
Figure 3.11. Skin adhesive peeling test. (a) 180° peeling adhesion force characterization setup using Instron 5943. (b) Adhesion force characterization for the skin adhesive-skin interface performed on dry and exercise-induced sweat secreting skin (where the skin adhesive was adhered to skin prior to physical exercise), indicating similar strength of adhesion between the skin and skin adhesive for both conditions.
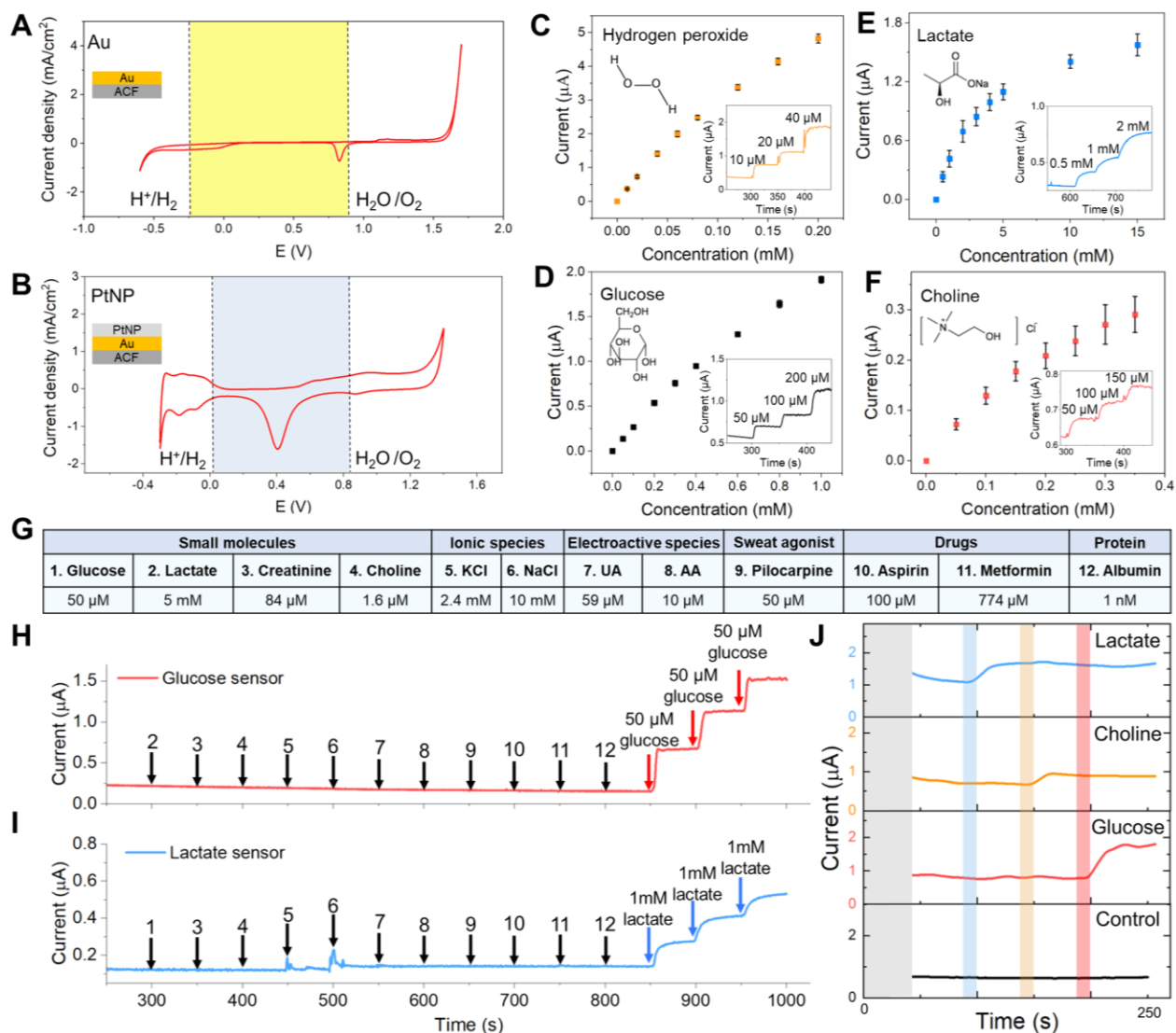
Figure 3.12. FESS signal transduction characterization. (a, b) Cyclic voltammetry characterization of Au (a) and Au/PtNP (b) electrode surfaces of the FESS, performed in 0.1 M H_2SO_4. Stable operational potential window (*29*) is highlighted with the shaded background. (c-f) FESS-based hydrogen peroxide (c), glucose (d), lactate (e), and choline (f) sensor responses to the target analytes (error bars indicate standard error (SE), n = 3). Inset figures show representative amperometric responses. (g) Table of common interferents in biofluids (*e.g.*, sweat). (h, i) Comprehensive selectivity studies for glucose (h) and lactate sensors (i) by monitoring the corresponding sensor responses to the sequential introduction of the listed interferents and target analytes (the introduction timepoints and the interferents/target analytes are indicated by arrows). (j) Characterization of a representative sensor array response built on the FESS platform for multiplex sensing.
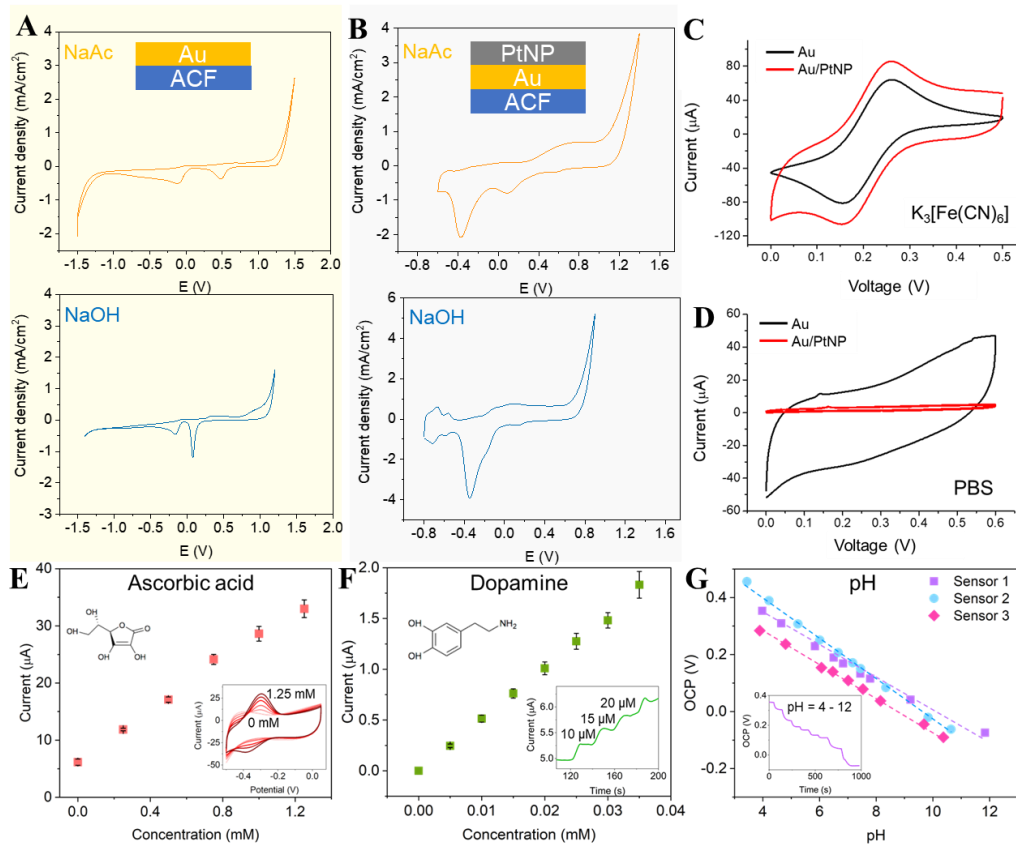
Figure 3.13. Electrochemical properties of Au and Au/PtNP electrode surface of the FESS. Cyclic voltammetry characterization of Au (a) and Au/PtNP (b) electrode surfaces of the FESS in 0.1 M NaAc (pH ~7.5), and 0.1 M NaOH (pH ~13) solutions. Cyclic voltammetry characterization of Au and Au/PtNP electrode surfaces of the FESS in 5 mM $K_3[Fe(CN)_6]$ + 0.1 M KCl (c) and 0.1 M PBS (d) solutions. FESS-based Au/PtNP electrode responses (SE, n = 3) toward dopamine (e) and ascorbic acid (f). (g) FESS-based pH sensors' calibration curves (SE, n = 3).
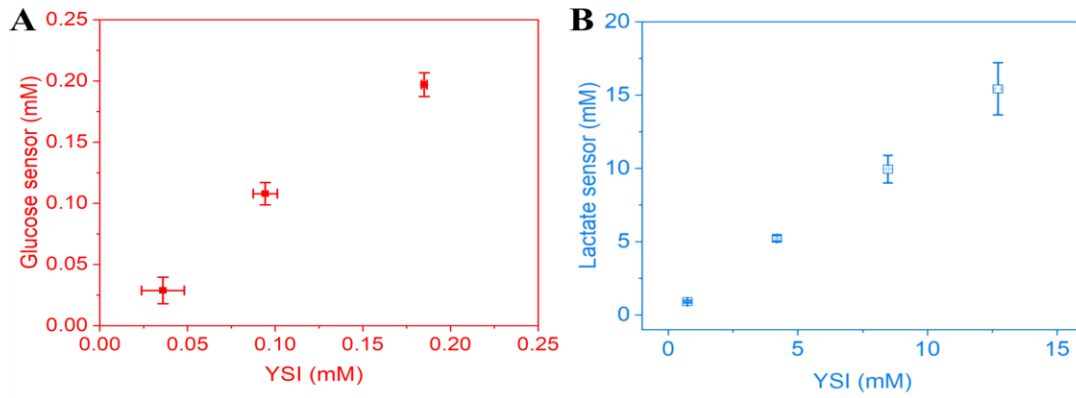
Figure 3.14. FESS-based electrochemical sensor accuracy validation. Glucose (a) and lactate (b) concentration measurements in a random sequence by FESS-based glucose (SE, n = 3) and lactate sensors *vs.* a gold-standard benchtop biochemistry analyzer (YSI 2900D, SE, n = 3).
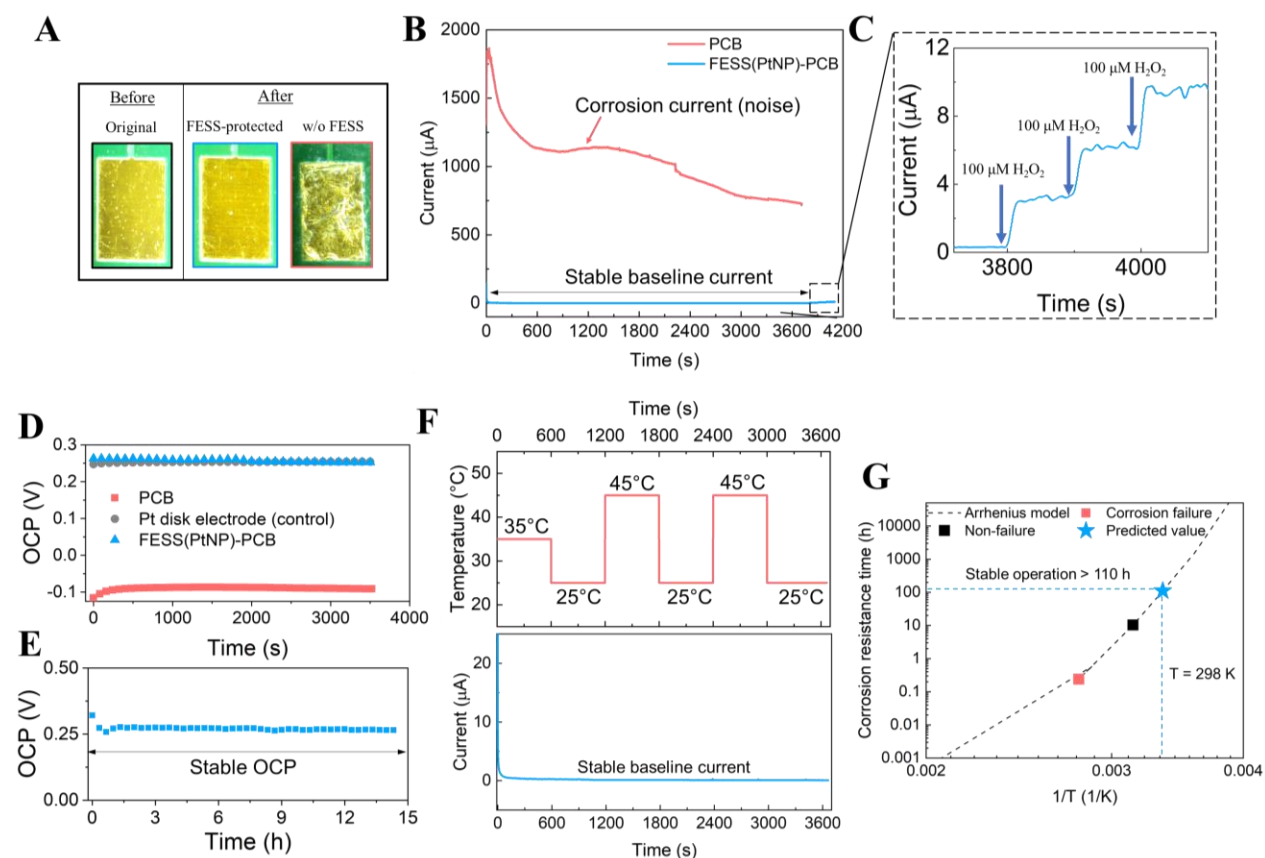
Figure 3.15. Anti-corrosion property of the FESS in aqueous environment. (a) Optical images of the two cases of FESS (PtNP)-coupled (image taken post-peeling) and bare PCB contact pads upon performing amperometric measurements (with contact pads immersed into PBS, 0.5 V *vs.* Ag/AgCl for 1 hour). The original optical image of the bare PCB contact pad is included for comparison. (b) Amperometric recordings performed with FESS(PtNP)-coupled and bare PCB contact pads (in PBS, 0.5 V *vs.* Ag/AgCl). The measured significantly large current density of the bare contact pad case indicates the onset of the electrochemical corrosion. (c) The follow up measured FESS (PtNP)-coupled electrode's linear responses to oxidant (H_2O_2) indicate the preserved catalytic capabilities of the electrodes (performed after the corrosion characterization experiment, shown in b). (d) Open circuit potential (OCP) measurement of bare and FESS (PtNP)-coupled PCB contact pads as well as standard Pt disk electrode for 1 hour in PBS against a standard Ag/AgCl reference electrode. The comparable performance of the FESS (PtNP)-coupled and Pt disk electrode cases indicate the transformation of the PCB contact pads to Pt-based electrodes upon coupling of the FESS (PtNP) with PCB contact pads. (e) OCP measurement of the FESS (PtNP)-coupled PCB contact pads over 14 hours, indicating the high stability of FESS (PtNP)-coupled interface for long-term operation in aqueous solution. (f) Amperometric recording of FESS (PtNP)-coupled PCB electrode in PBS (0.5 V *vs.* Ag/AgCl), during thermal cycling. (g) Accelerated life testing (PBS, 0.5 V *vs.* Ag/AgCl, heated with hot plate) to predict the minimum corrosion resistance lifetime of FESS (PtNP)-coupled PCB contact pads at room temperature (298.15 K) using Arrhenius model. The fitting is based on two reference measurements, performed at: 1) 358.15 K (leading to corrosion) and 2) 318.15 K, which did not lead to corrosion during the recorded time window (where stable recorded amperometric current was measured), and thus, used to set the lower-bound on the estimated lifetime for stable operation at room temperature.
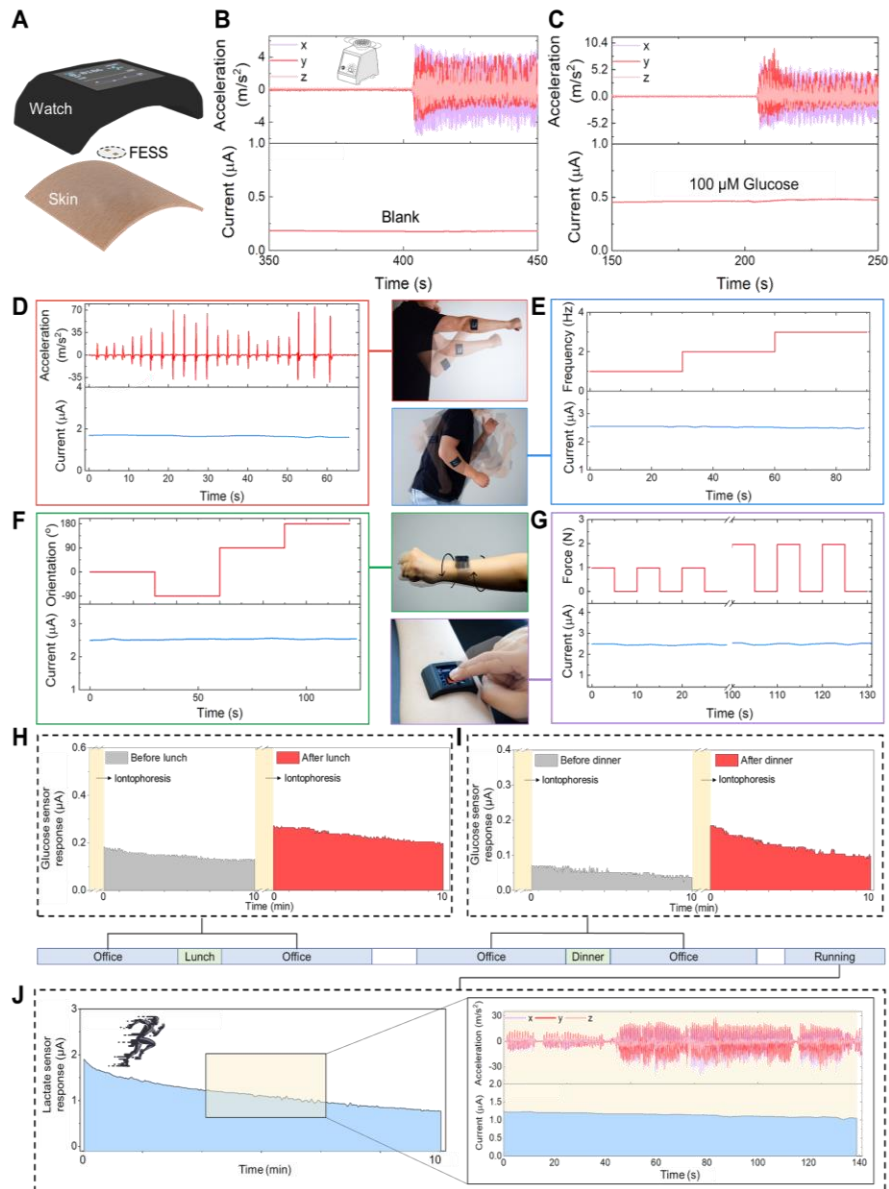
108

Figure 3.16. Custom-developed FESS-integrated smartwatch for on-body application. (a) Illustration of the FESS-enabled smartwatch (containing FESS, LCD screen, PCB, and battery units housed within a 3D-printed case). (b, c) *Ex-situ* characterization of the FESS-PCB glucose sensing system response upon vortical vibration (FESS electrode: 6 mm^2, microfluidic channel height: 170 μm and volume: 4 μL). The vibrational acceleration profiles are presented in the top- half, and the sensor responses are captured in the bottom-half when tested in PBS (b) and 100 μM glucose in PBS (c). (d-g) On-body signal fidelity characterization of a FESS-PCB lactate sensing system with a subject performing shadow boxing (d), arm swinging (e), wrist twisting (f), and device-pressing (g). The acceleration, frequency, orientation, and force profiles are presented in the top-half and sensor responses are captured in the bottom-half. (h-j) Monitoring the subjects' metabolite profiles through various daily events and in different settings. Iontophoretically-induced sweat glucose were measured before and after lunch (h) and dinner (i). (j) Sweat lactate measurements during exercise (a representative motion-induced acceleration profile is shown on the right). Photo credit: Peterson Nguyen, Kaili Chiu, Yichao Zhao, University of California, Los Angeles
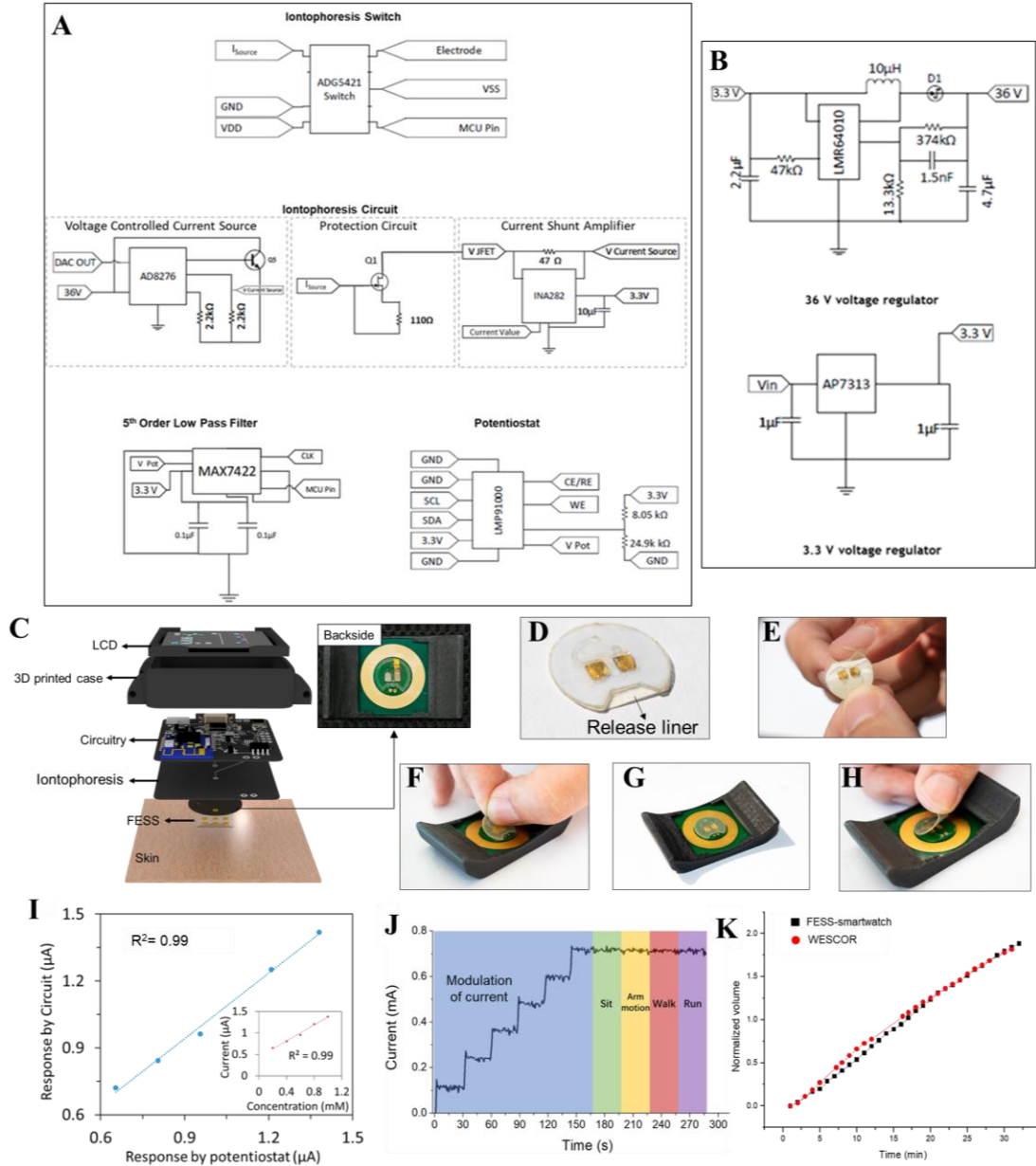
Figure 3.17. FESS-enabled smartwatch. (a) Schematic diagrams of the switch, programmable iontophoresis, and sensing circuitries. (b) Schematic diagrams of the implemented power-regulating circuitries. (c) Exploded view of the custom-developed wearable smartwatch with a ring-shaped iontophoresis module. The backside of the smartwatch is shown on the right, illustrating the interface of the smartwatch readout contact pads with the FESS (at the center). (d)-(h) Picking, placing, and detaching a representative FESS (1×2-pixel, 6 mm^2 electrode) on the back of the custom-developed smartwatch. (i) The measured amperometric glucose sensor response by PCB *vs.* potentiostat (inset shows the corresponding calibration curve obtained by the potentiostat). (j) Mobile application-based controlled delivery of different iontophoresis current levels. (k) Comparison of the secreted sweat volume (normalized with respect to the stimulated area) induced by the FESS-smartwatch iontophoresis module *vs.* a commercial iontophoresis instrument (WESCOR). Photo credit: Peterson Nguyen, University of California, Los Angeles.
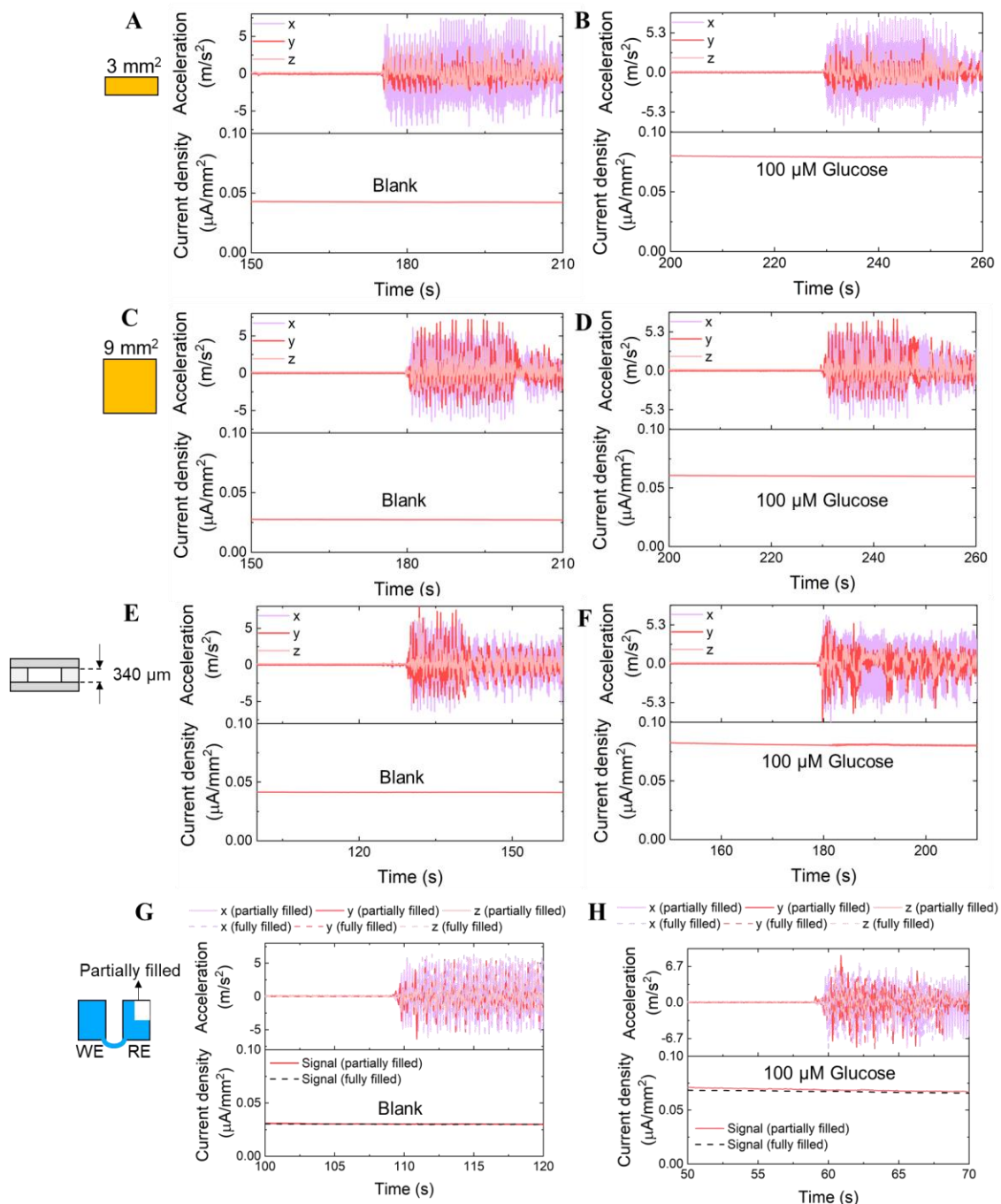
Figure 3.18. Ex-situ characterization of the signal stability of FESS-PCB glucose sensing system in presence of vortical vibration. The measured amperometric responses of FESS to blank solution and 100 μM glucose solution with 3 mm^2 (a, b) and 9 mm^2 FESS-electrodes (c, d) (both with channel height: 170 μm), as well as with FESS channel height of 340 μm (e, f) (6 mm^2 electrode). Amperometric response of FESS to blank solution (g) and 100 μM glucose solution (h), where the FESS microfluidic channel (height: 170 μm) was partially filled (~ 90%) with the solution (while ensuring that the 6 mm^2 working electrode, WE, was fully covered with the solution and fluidically connected to the 6 mm^2 reference electrode, RE). The corresponding vibrational acceleration profiles is shown atop each amperometry recording.
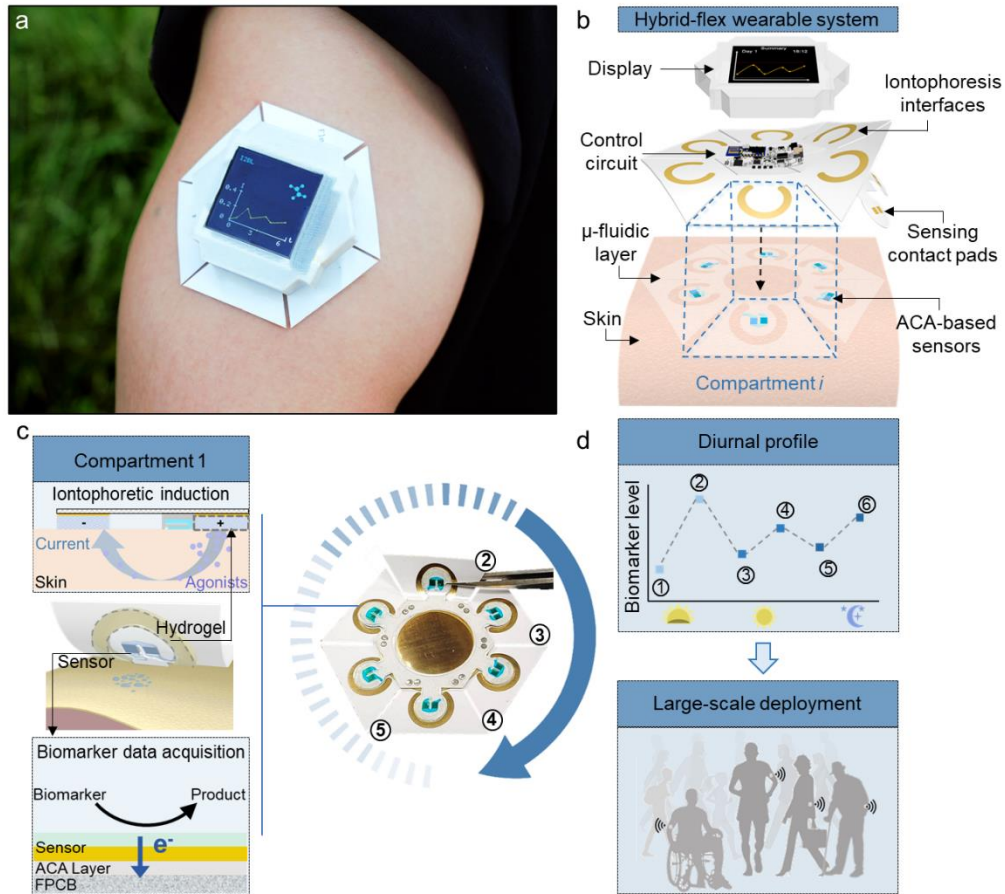
Figure 4.1. Design and operational principle of the hybrid-flex wearable system. (a) Image of the developed hybrid-flex wearable system adhered on a subject's arm; (b) Exploded schematic of the multi-compartment system, demonstrating vertical integration of an FPCB with iontophoresis electrode arrays (radially fabricated on the backside of the FPCB) and a microfluidic-sensing module; (c) Schematic representation of bioanalytical operations (left: iontophoresis, sensing) delivered by each of the compartments (right: bottom view photograph of the developed hybrid-flex wearable system) that can be programmatically activated at intermittent time points to obtain biomarker data; (d) Conceptual illustration of positioning the autonomous system to track the diurnal biomarker profiles for population-level health monitoring.
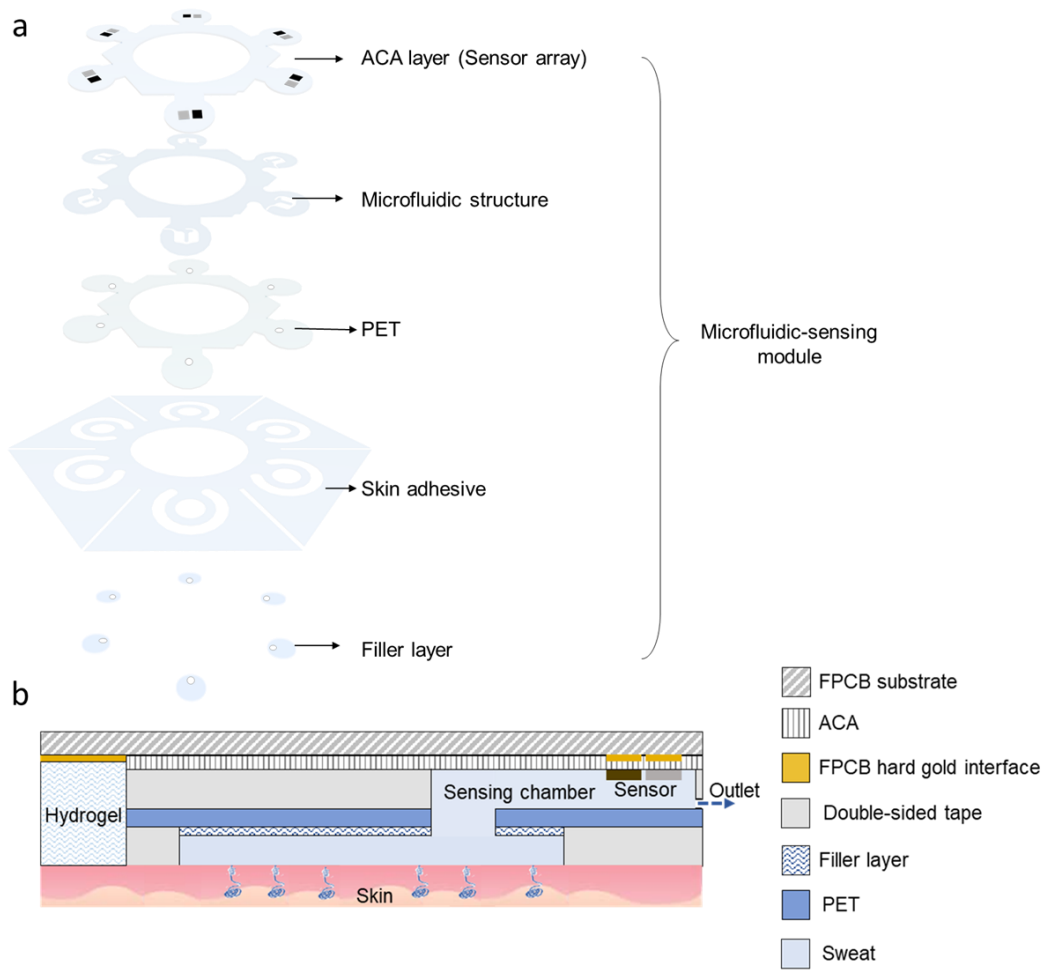
Figure 4.2. Microfluidic-sensing module design. (a) Exploded view of the microfluidic-sensing module; (b) Cross-section view of the microfluidic-sensing module-skin interface.
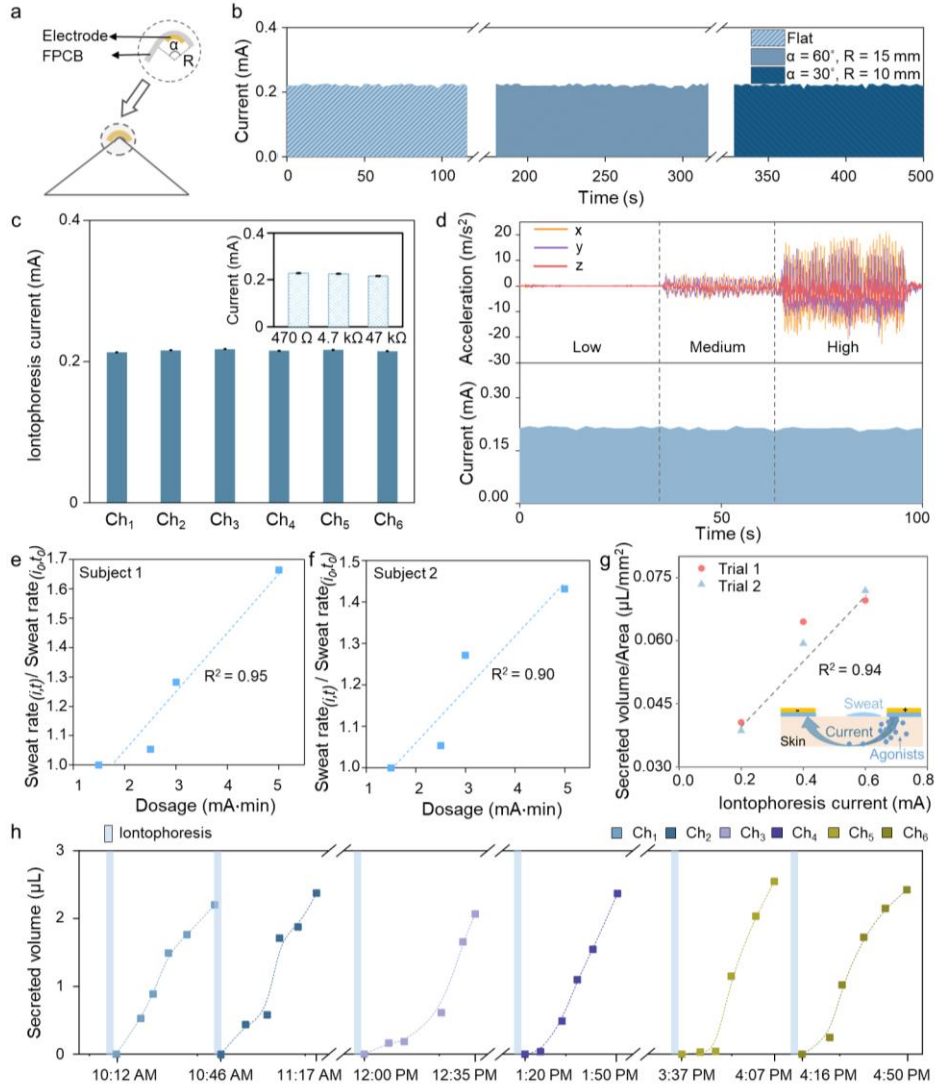
Figure 4.3. Characterization of the miniaturized and programmable iontophoresis. (a) Illustration of the setup for iontophoresis current characterization, performed under three bending conditions (1. no bending, 2. $\alpha = 60°$, $R = 15$ mm, and 3. $\alpha = 30°$, $R = 10$ mm); (b) Real-time iontophoresis current recordings under corresponding bending conditions (programmed current: 0.2 mA, CV for all cases < 1.5%); (c) Demonstration of consistent iontophoresis current delivery across all compartments (load: 47 kΩ, programmed current: 0.2 mA, $\Delta = 0.9\%$). Inset shows load-independent iontophoresis current delivery capability of the system. Error bars indicate standard error ($n = 6$ compartments). Δ is calculated as percent variation of the maximum measured current level from the baseline average value; (d) *In-situ* characterization of iontophoresis current stability on body under different exercise intensities (programmed current: 0.2 mA); (e, f) Sweat secretion rate *vs.* iontophoretic dosage for subject 1 (e) and 2 (f). The normalized sweat rate is obtained by dividing the measured sweat rate with the iontophoretic dosage ($I_n \times t_n$) by the sweat rate with the dosage ($I_0 \times t_0$) = (0.5 mA × 3 min); (g) Tunable sweat secretion rate achieved by programming the iontophoresis current (rendered by our wearable platform, area of stimulation: 0.6 cm^2). Inset shows the iontophoretic sweat agonist delivery process; (h) Intermittent sweat induction throughout a day using six sequentially activated compartments ($I = 0.6$ mA, $t = 5$ min).
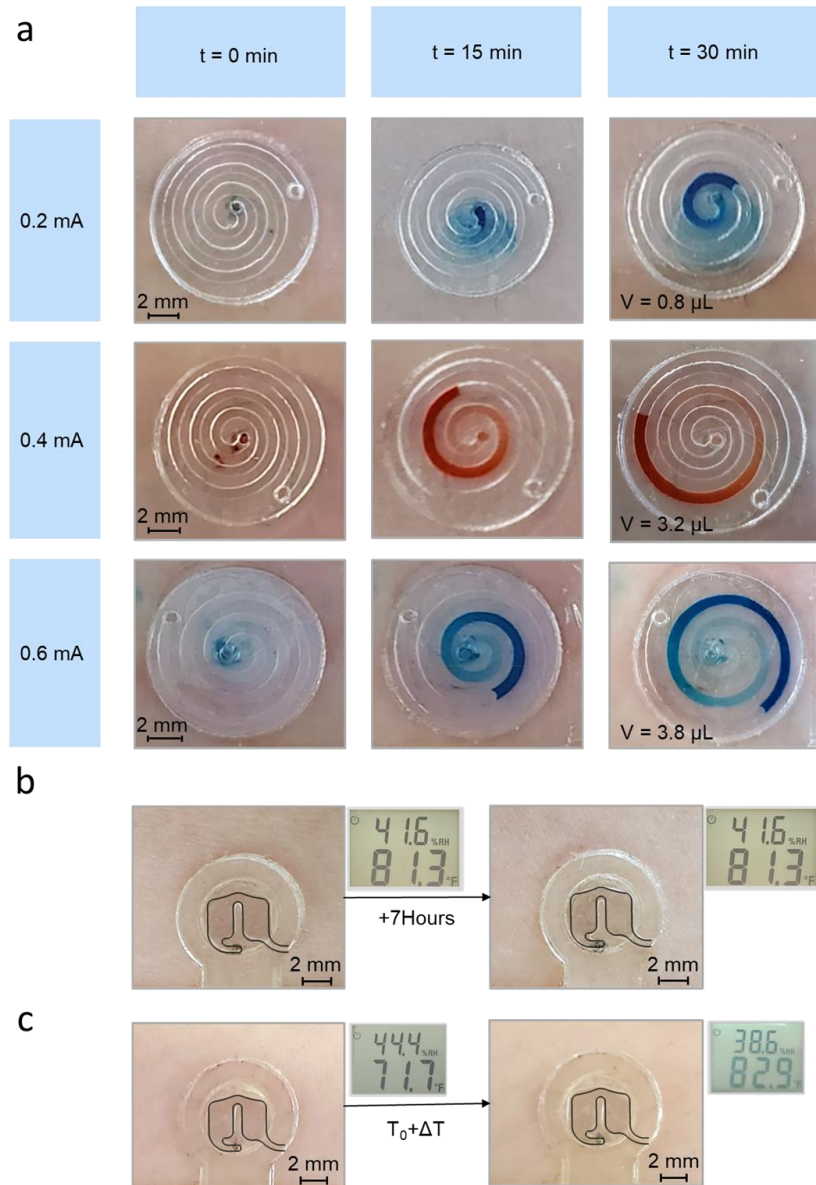
114

Figure 4.4. Sweat rate measurement by optical images of microfluidic modules. (a) Optical sweat secretion characterization (with the aid of color dyes embedded in the channel), following three different iontophoresis current levels; (b) Optical image of a compartment illustrating negligible accumulation of sweat sample due to natural perspiration after 7 hours of non-labor daily activities; (c) Optical image of a compartment illustrating negligible accumulation of sweat sample (over 2 hours) upon a moderate increase in the ambient temperature from ~ 22 °C to ~ 28 °C (equivalently, ~ 72 °F to ~ 83 °F, as measured and shown by a lab digital thermometer).
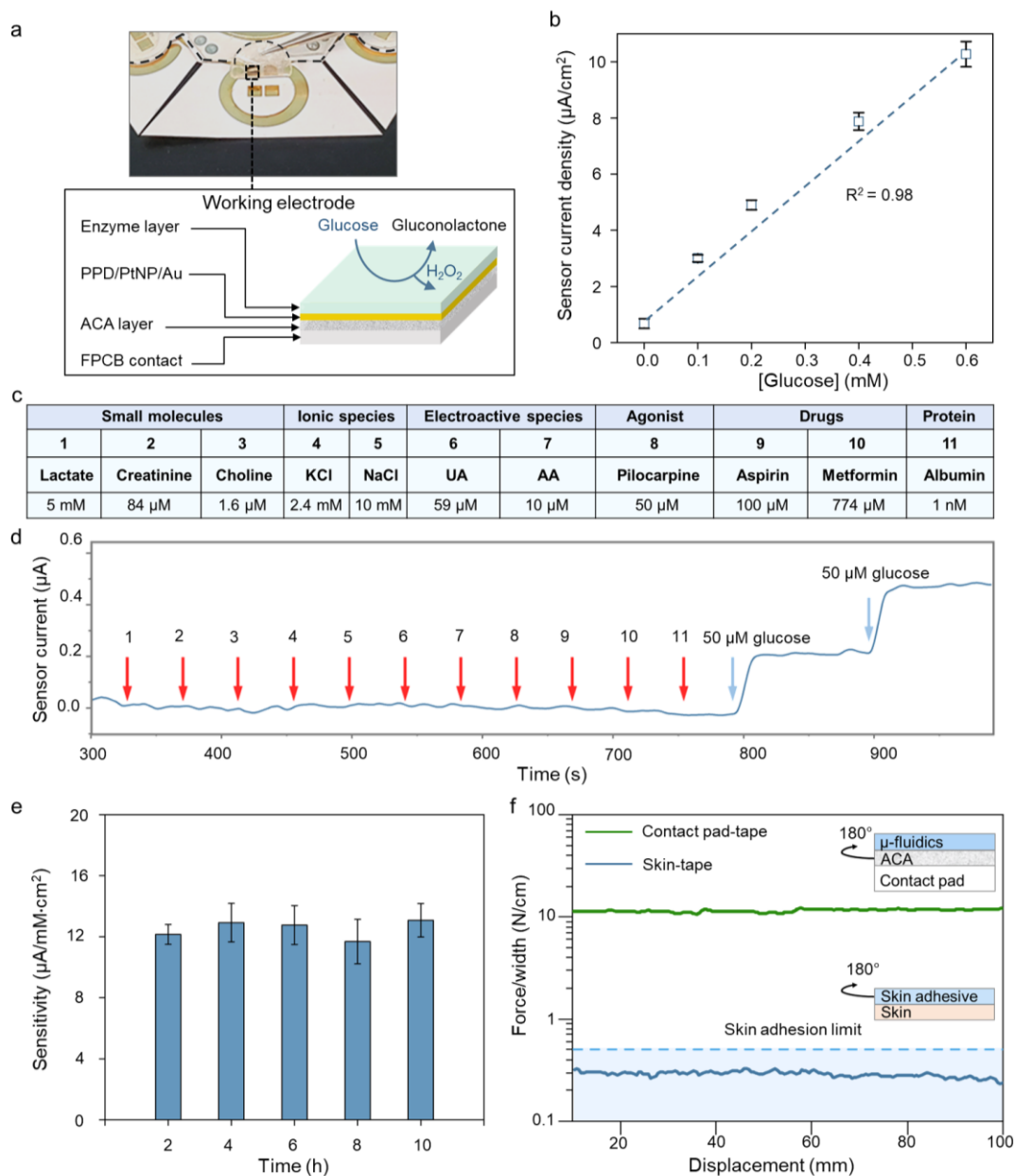
Figure 4.5. Characterization of the electrochemical sensing interface. (a) Integration of the disposable microfluidic-sensing module onto the corresponding FPCB contact pad and illustration of the sensing layers/mechanism for the developed glucose sensor; (b) The amperometric response of developed glucose sensors ($n = 3$ different sensors). Error bars indicate standard error (SE); (c) Table of common interfering molecules in sweat used for the selectivity study; (d) Selectivity study for the glucose sensor by monitoring its response to the sequentially-introduced interferents and glucose. The arrows indicate the introduction time points for the corresponding interferents/glucose; (e) The enzymatic sensors' preserved sensitivities over an 8-hour long storage at room temperature (SE, $n = 3$ different sensors); (f) 180° peeling tests characterizing the adhesion force between the skin and tape, as well as PCB and tape. The inset demonstrates the setup of the 180° peeling test.

116
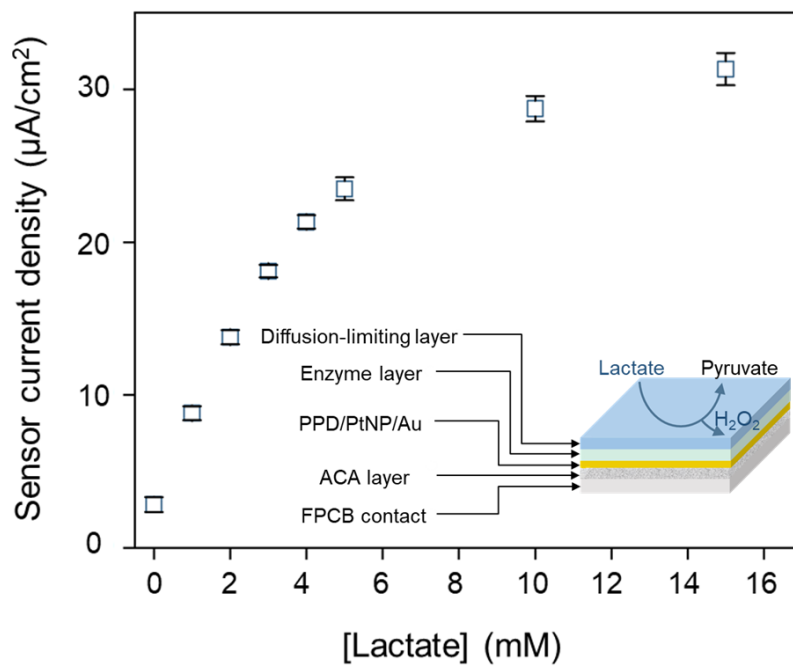
Figure 4.6. The developed lactate sensor's responses to different lactate solutions (SE, *n* = 3). Inset illustrates the underlying layers of the constructed lactate sensing interface.
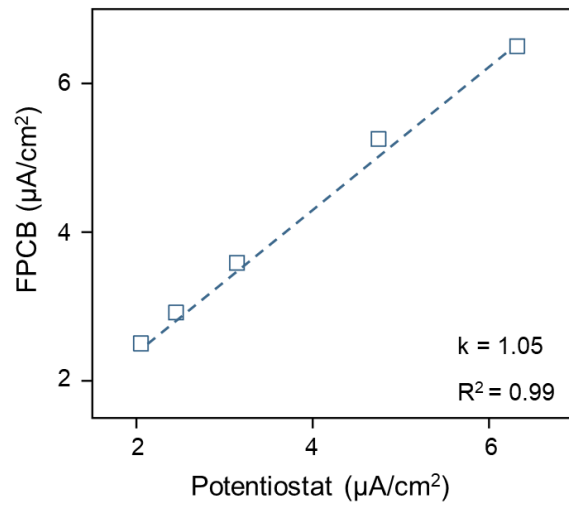
Figure 4.7. Comparison of glucose sensor readouts (current density) captured by the FPCB *vs*. potentiostat.
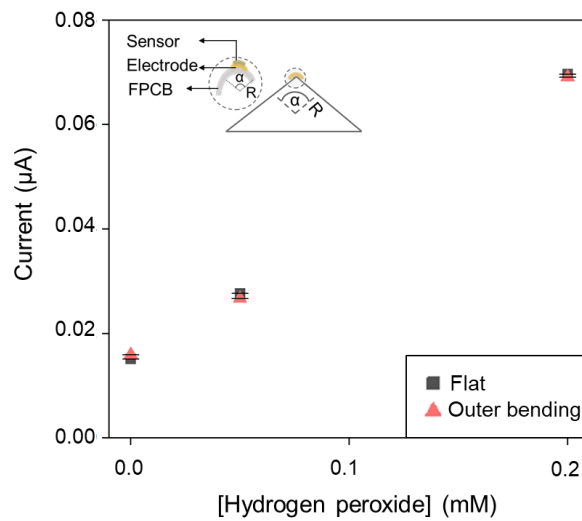

Figure 4.8. Evaluation of the PtNP/Au electrode (sensor substrate) response to hydrogen peroxide under different bending conditions (1. no bending, and 2. $\alpha = 60°$, $R = 15$ mm).
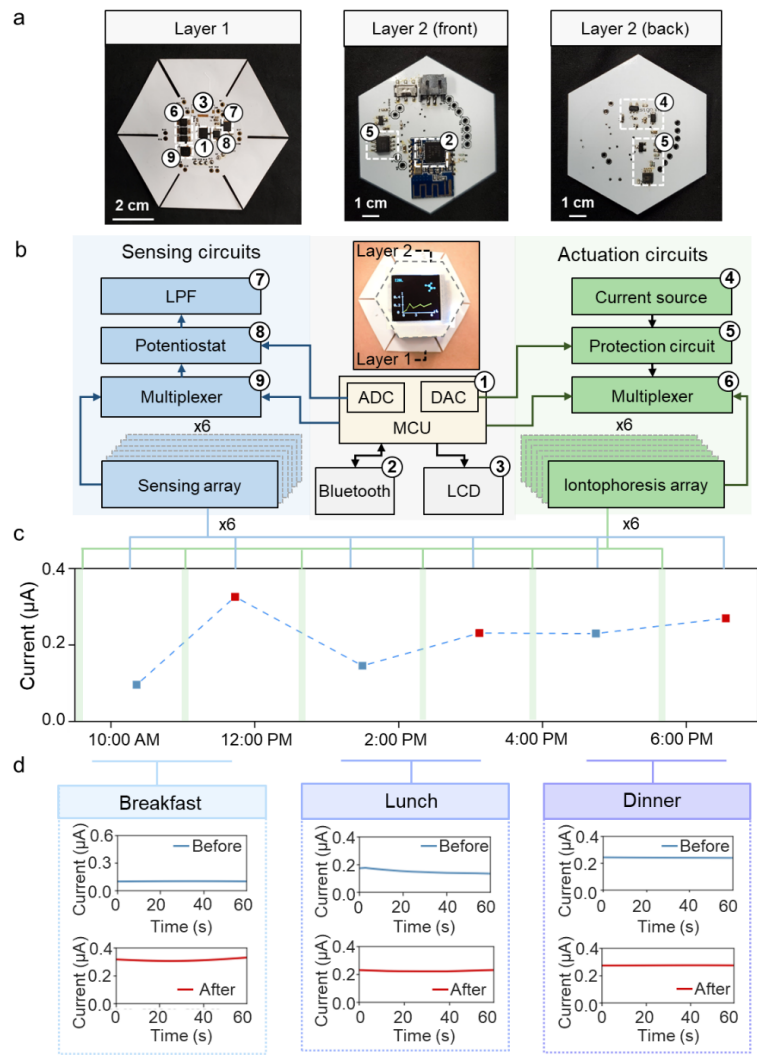
Figure 4.9. Integrated system for diurnal data acquisition. (a) Optical images of the two-layered FPCB module. Layer 1 features the sensing circuitry (at the center) and iontophoretic electrode array (mechanically flexible flaps). Layer 2 features the iontophoretic circuitry and the data transmission/display interfaces; (b) The system-level block diagram of the circuit operations; (c) Diurnal sweat glucose profile (specifically, before and after main meal intakes), captured *via* on-body autonomous sweat sampling and analysis (by our system); (d) Representative real-time amperometric recording of glucose sensors corresponding to the diurnal sweat glucose profile shown in Fig. 4.9c.
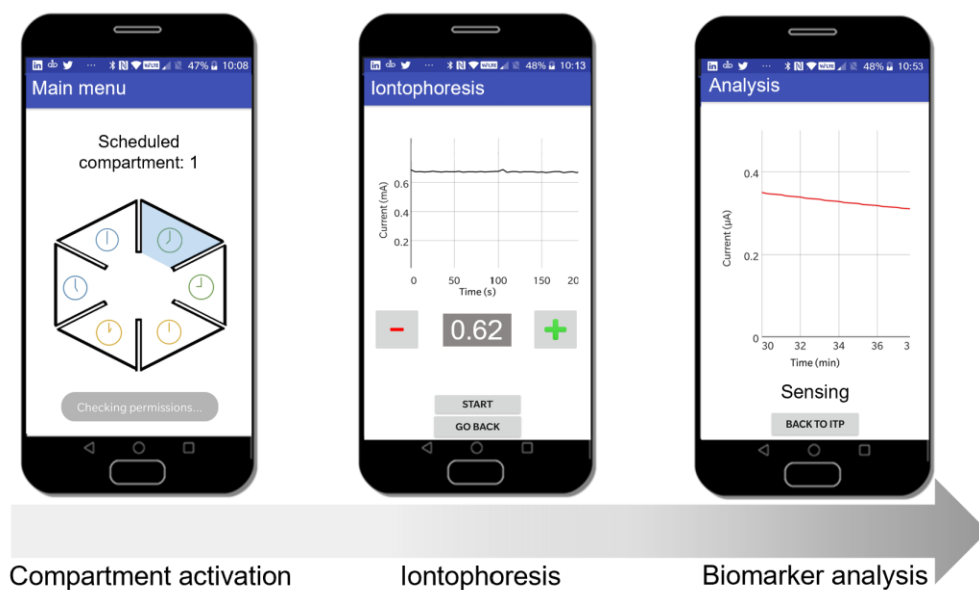
Figure 4.10. The custom-developed mobile application to control compartmentalized operations (programmable iontophoresis and sensing) and data display/storage.
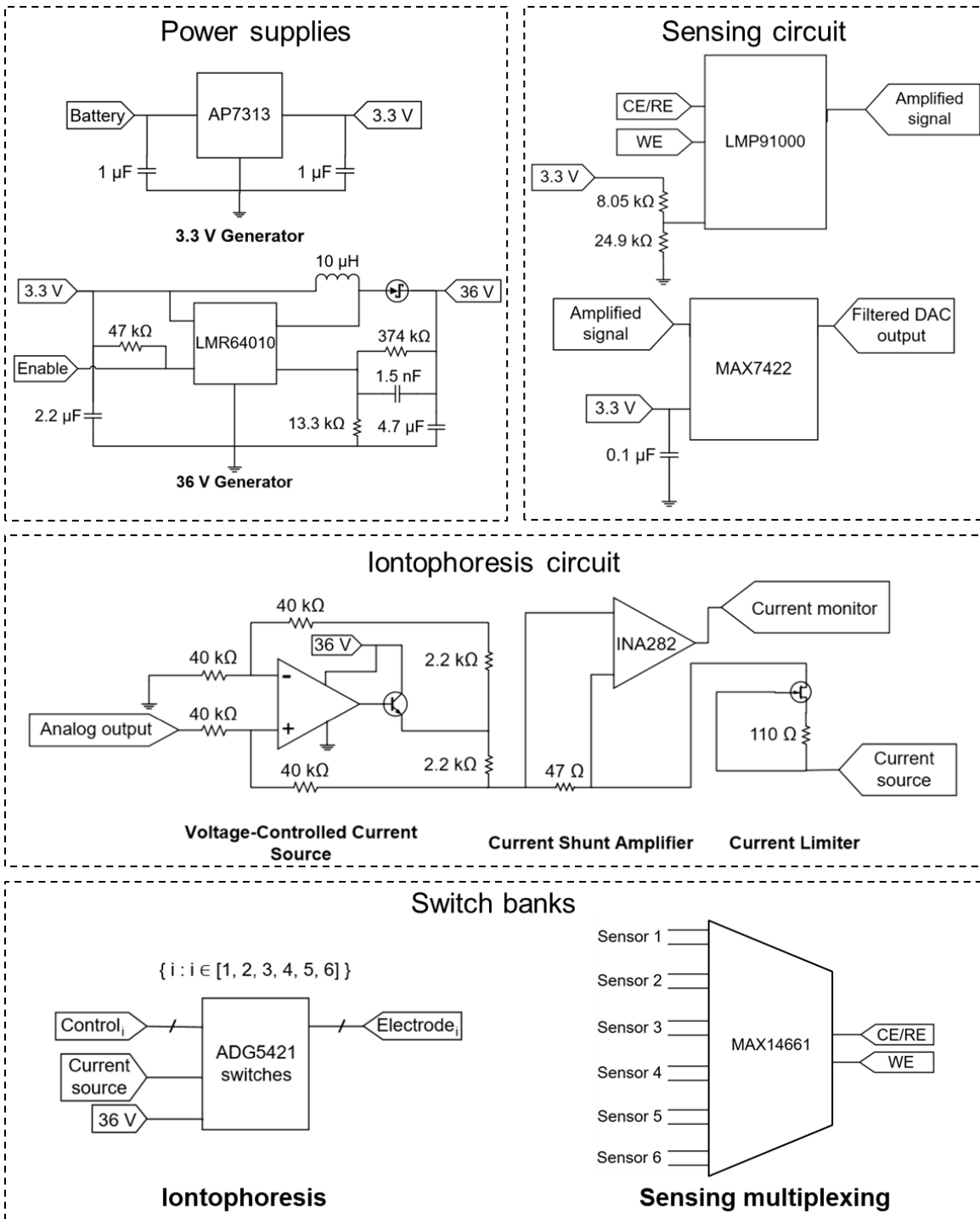
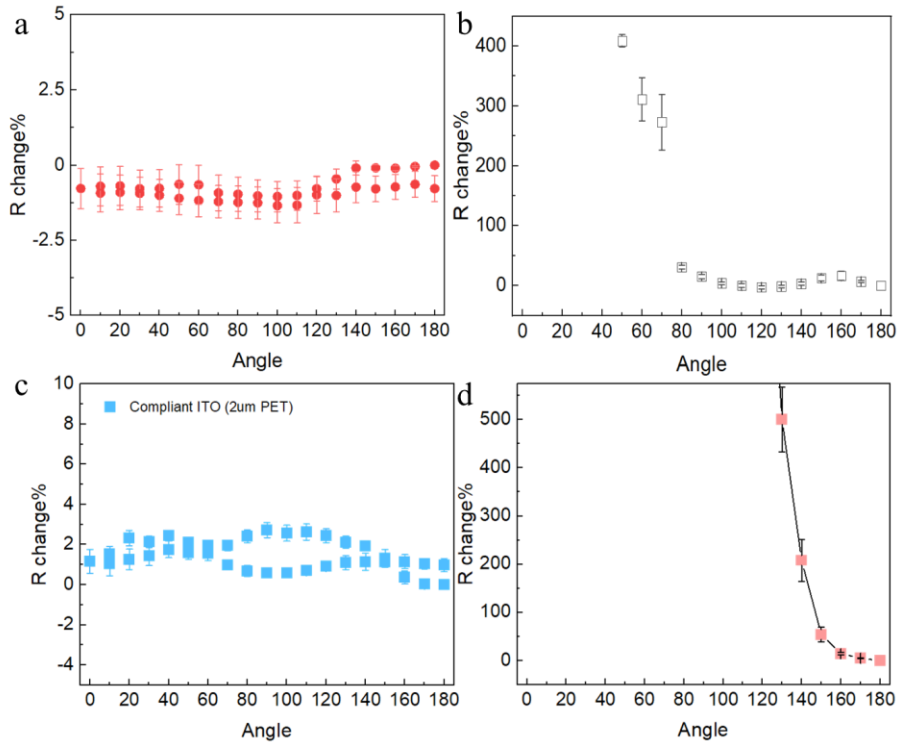**Figure 4.11. Schematic diagram of the wireless FPCB's circuitries.**

121

Figure 5.1. Resistance changes of (a) compliant Au, (b) single layer Au, (c) compliant ITO and (d) single layer ITO during folding and unfolding.
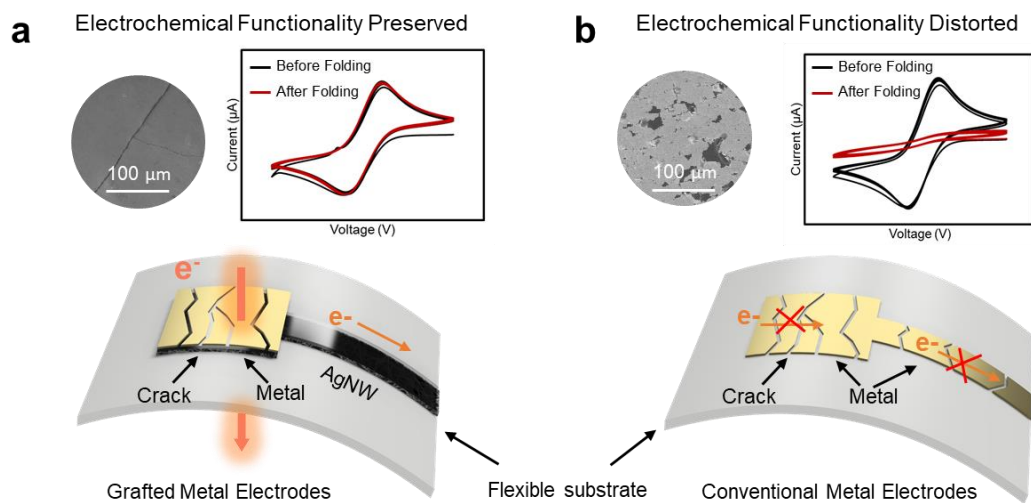
Figure 5.2. Schematics to illustrate electrochemical signal transduction and transmission under strain for (a) ACF-based Au grafted AgNW electrode and (b) conventional Au electrode.
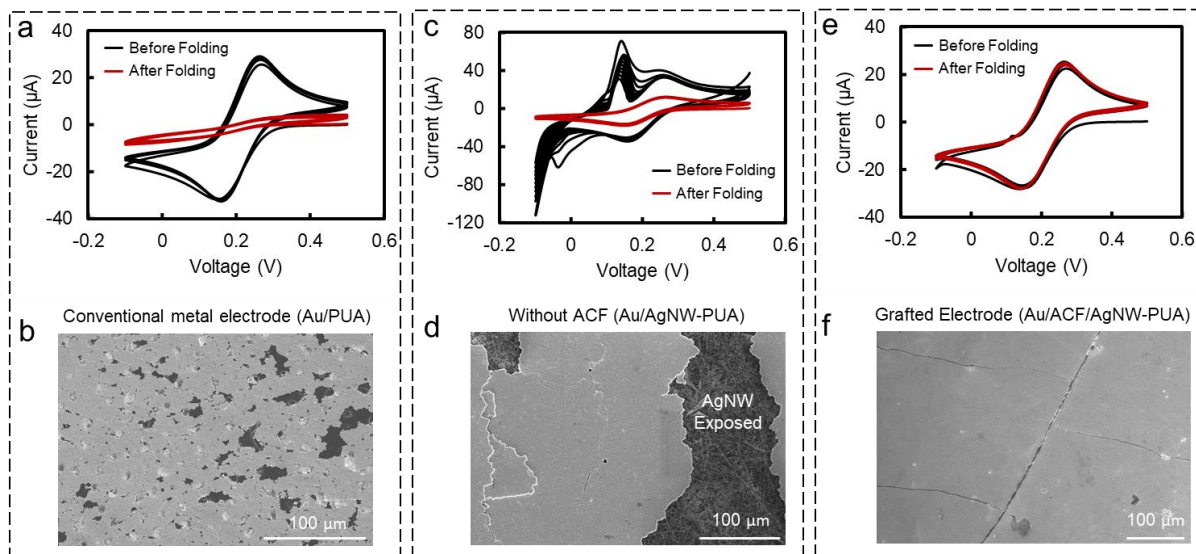
Figure 5.3. Cyclic voltammetry characterization and SEM visualization of electrodes. (a) CV before and after Au/AgNW/PUA electrode folding. (b) SEM image Au/PUA electrode after folding. (c) CV before and after Au/PUA electrode folding. (d) SEM image Au/AgNW/PUA electrode after folding. (e) CV before and after Au/ACF/AgNW/PUA electrode folding. (f) SEM image Au/ACF/AgNW/PUA electrode after folding.